INFORMATION TO USERS

This manuscript has been reproduced from the microfilm master. UMI films the text directly from the original or copy submitted. Thus, some thesis and dissertation copies are in typewriter face, while others may be from any type of computer printer.

The quality of this reproduction is dependent upon the quality of the copy submitted. Broken or indistinct print, colored or poor quality illustrations and photographs, print bleedthrough, substandard margins, and improper alignment can adversely affect reproduction.

In the unlikely event that the author did not send UMI a complete manuscript and there are missing pages, these will be noted. Also, if unauthorized copyright material had to be removed, a note will indicate the deletion.

Oversize materials (e.g., maps, drawings, charts) are reproduced by sectioning the original, beginning at the upper left-hand corner and continuing from left to right in equal sections with small overlaps.

Photographs included in the original manuscript have been reproduced xerographically in this copy. Higher quality 6" x 9" black and white photographic prints are available for any photographs or illustrations appearing in this copy for an additional charge. Contact UMI directly to order.

ProQuest Information and Learning
300 North Zeeb Road, Ann Arbor, MI 48106-1346 USA
800-521-0600

SURF BEAT FORCING AND DISSIPATION

By

Stephen M. Henderson

SUBMITTED IN PARTIAL FULFILLMENT OF THE
REQUIREMENTS FOR THE DEGREE OF
DOCTOR OF PHILOSOPHY
AT
DALHOUSIE UNIVERSITY
HALIFAX, NOVA SCOTIA
APRIL 2002

DALHOUSIE UNIVERSITY

FACULTY OF GRADUATE STUDIES

The undersigned hereby certify that they have read and recommend to the Faculty of Graduate Studies for acceptance a thesis entitled "Surf Beat Forcing and Dissipation" by Stephen M. Henderson, in partial fulfillment of the requirements for the degree of Doctor of Philosophy.

Dated: April 1, 2002

External Examiner:

Research Supervisor:

Research Supervisor

Examining Committee

DALHOUSIE UNIVERSITY

Date: **April 2002**

Author: **Stephen M. Henderson**

Title: **Surf beat forcing and dissipation**

Department: **Oceanography**

Degree: **Ph.D.** Convocation: **May** Year: **2002**

Permission is herewith granted to Dalhousie University to circulate and to have copied for non-commercial purposes, at its discretion, the above title upon the request of individuals or institutions.

Signature of Author

Contents

Abstract

Estimates of the cross-shore surf beat energy flux were substituted into an energy equation to determine the rate of net surf beat forcing (or dissipation) on a beach near Duck, North Carolina. Inside the surf zone, surf beat dissipation exceeded forcing. Outside the surf zone, surf beat forcing exceeded dissipation. During storms, the net shoreward surf beat energy flux in the outer surf zone was about half the energy flux that could be carried if all surf beat propagated directly shorewards. The associated dissipation of surf beat in the surf zone was very strong (the total surf beat energy dissipated in the surf zone in a single beat period sometimes exceeded the total surf beat energy stored there). At relatively low beat frequencies (0.005–0.025 Hz), the dominant Empirical Orthogonal Functions (EOF's) of measured pressure and velocity in 1–5 m depth had the nodal structure expected of cross-shore standing waves. At higher beat frequencies (0.03–0.05 Hz), dominant EOF's had some nodal structure, but their phase increased steadily with distance from the shore, indicating net shoreward propagation.

Forced, dissipative, shore-oblique shallow water waves were modeled. Forcing applied shoreward of the edge wave turning point generates edge waves, whereas forcing applied sufficiently far seaward of the turning point generates evanescent waves. Weakly-dissipative edge waves are nearly cross-shore standing, whereas strongly-dissipative edge waves progress obliquely across-shore, carrying energy from regions of forcing to regions of dissipation. Evanescent waves decay almost exponentially with distance from regions of forcing. Bound evanescent waves propagate shorewards and depress the sea level under groups of large incident waves. However, unlike the bound waves described by previous researchers, evanescent bound waves are not released when short waves break, and do not radiate energy away from the breakpoint.

List of symbols

$\langle X \rangle_\omega$ = complex amplitude of time series X at frequency ω,

$\langle X \rangle'_\omega$ = complex amplitude of windowed time series X at frequency ω,

$\hat{X}$ = complex amplitude of X at frequency $-\omega$ and longshore wavenumber k,

$\overline{X}$ = sample mean of X,

a_n = amplitude of mode n edge wave (m),

c_f = bottom drag coefficient,

Cg = group velocity (ms^{-1}),

$\mathcal{D}(\omega)$ = depth-integrated dissipation of frequency ω motion ($\mathrm{m}^3\mathrm{s}^{-3}$),

$E[X]$ = expected value of X,

$\mathcal{E}(\omega) = \int_{z=-h}^{0} |\langle \boldsymbol{u}(z) \rangle_\omega|^2 \, dz + g|\langle \eta \rangle_\omega|^2$ = depth-integrated linear energy density of frequency ω wave ($\mathrm{m}^3\mathrm{s}^{-2}$),

$\mathcal{E}_{nl}(\omega) = h|\langle \tilde{\boldsymbol{u}} \rangle_\omega|^2 + g|\langle \eta \rangle_\omega|^2$, ($\mathrm{m}^3\mathrm{s}^{-2}$),

$\mathcal{E}_{sb} = \int_{\omega_c=0.005\ \mathrm{Hz}}^{0.05\ \mathrm{Hz}} \mathcal{E}(\omega_c)$ = depth-integrated linear energy density of surf beat ($\mathrm{m}^3\mathrm{s}^{-2}$),

f_e = wave dissipation factor,

f_n = projection of forcing onto n'th edge wave mode,

F = nonlinear forcing in shallow water mass conservation equation,

F_x = nonlinear forcing in shallow water cross-shore momentum equation (ms^{-2}),

F_y = nonlinear forcing in shallow water longshore momentum equation (ms^{-2}),

${}_1F_1(a,b,c)$ = Kummer's function (Laguerre polynomial if $b = 1$ and $a \in \mathbb{Z}^-$),

$\mathcal{F}(\omega)$ = depth-integrated momentum flux working on frequency ω motion (m^3s^{-3}),

$g = 9.81\ ms^{-2}$ = gravitational acceleration,

$G(x, x_f)$ = Green's function representing sea level response at x to forcing at x_f,

h = still water depth (m),

h_{bar} = water depth at crest of sandbar (m),

h_{trough} = maximum water depth shoreward of sandbar (m),

h_T = edge wave turning depth (m),

$Hs = 4\overline{\eta_w^2}^{1/2}$ = significant wave height (m),

$\mathrm{i} = (-1)^{1/2}$,

k = longshore wavenumber (m^{-1}),

$k_c = k/(2\pi)$ = cyclic longshore wavenumber (m^{-1}),

$\boldsymbol{k}$ = wavenumber vector (m^{-1}),

K = inverse of evanescent wave cross-shore e-folding scale (m^{-1}),

$\mathcal{L} = \dfrac{\partial}{\partial x}\left(x\dfrac{\partial}{\partial x}\right) - k^2 x$, ($m^{-1}$),

$\boldsymbol{M}$ $=(M_1, M_2) =$ mass flux between sea level and still water level,
approximately the Stokes Drift (m^2s^{-1}),

$n = \frac{1}{2}\left(\frac{\omega^2}{kg\beta} - 1\right) =$ edge wave mode number,

$n' = \frac{1}{2}\left[\frac{\omega^2(1 + i\lambda/\omega)}{kg\beta} - 1\right]$,

$\mathcal{N}(\omega) =$ depth-integrated nonlinear energy transfer to frequency ω motion (m^3s^{-3}),

$p =$ water pressure ($kg\ m^{-1}s^{-2}$),

$q_{sb} =$ estimate of $\int_{\omega_c=0.005\ \mathrm{Hz}}^{0.05\ \mathrm{Hz}} q_x(\omega_c) =$ depth-integrated
shoreward linear energy flux due to surf beat (m^4s^{-3}),

$q_x(\omega) = 2h\Re[g\langle\eta\rangle_\omega \langle u\rangle_{-\omega}] =$ depth-integrated shoreward linear
energy flux due to waves of frequency ω (m^4s^{-3}),

$q_y(\omega) = 2h\Re[g\langle\eta\rangle_\omega \langle v\rangle_{-\omega}] =$ depth-integrated longshore linear
energy flux due to waves of frequency ω (m^4s^{-3}),

$Q = 2\pi \dfrac{\text{Total energy of mode}}{\text{Energy of mode dissipated in a single wave period}}$,

$\Re =$ real part,

$S =$ radiation stress ($kg\ s^{-2}$),

$t =$ time (s),

$T =$ depth-integrated momentum flux, approximately the radiation stress (m^3s^{-2}),

$\boldsymbol{u} = (u_1, u_2) =$ horizontal velocity (ms^{-1}),

$\tilde{\boldsymbol{u}} = (\tilde{u}_1, \tilde{u}_2) = \boldsymbol{u} + \boldsymbol{M}/h$, ($ms^{-1}$),

$\overline{|\boldsymbol{u}_{sb}|^2} =$ estimate of $2\int_{\omega_c=0.005\ \mathrm{Hz}}^{0.05\ \mathrm{Hz}} \Phi_{\omega_c}(|\boldsymbol{u}|, |\boldsymbol{u}|)\, d\omega_c =$ speed variance
due to surf beat (m^2s^{-2}),

$V = \frac{g}{2}\int_{x=0}^{\infty} |\hat{\eta}|^2\, dx =$ cross-shore integrated potential energy at frequency $-\omega$, wavenumber k ($m^4 s^{-2}$),

$\boldsymbol{w}$ = depth-integrated energy flux (includes nonlinear components) ($m^4 s^{-3}$),

$\boldsymbol{x} = (x_1, x_2) =$ horizontal position vector (m),

x = distance from shore (m),

$x_f = x$ location at which forcing is applied (m),

$x_T = x$ location of edge wave turning point (m),

y = longshore position (m),

z = elevation above sea level (m),

$\mathbb{Z}$ = the set of integers,

β = beach slope,

γ = value of Hs/h for a broken wave,

$\delta_{j,k} = \begin{cases} 1 & i = j \\ 0 & i \neq j \end{cases}$ = Kronecker delta,

$\delta(x)$ = Dirac Delta,

$\Delta\omega = 2\pi/\Delta t =$ frequency resolution for Fourier transform of time series of length Δt (s^{-1}),

$\tilde{\eta} = e^{kx}\hat{\eta}$, (m),

η = sea level above still water level (m),

$\overline{\eta_{sb}^2}$ = estimate of $2\int_{\omega_c=0.005\text{ Hz}}^{0.05\text{ Hz}} \Phi_{\omega_c}(\eta,\eta)\, d\omega_c =$ sea level variance due to surf beat (m^2),

$\overline{\eta_w^2}$ = estimate of $2\int_{\omega_c=0.05\text{ Hz}}^{0.3\text{ Hz}} \Phi_{\omega_c}(\eta,\eta)\, d\omega_c =$ sea level variance due to incident waves (m^2),

λ = Rayleigh bottom drag coefficient (s^{-1}),

$\Lambda = \dfrac{\omega^2(1 + i\lambda/\omega)}{g\beta}$, ($m^{-1}$),

$\Lambda_n = k(2n + 1) =$ eigenvalue of edge wave problem (m^{-1}),

$\rho = q/(\mathcal{E}Cg) =$ progressiveness parameter,

ϱ = water density (kg m^{-3}),

$\boldsymbol{\tau} = (\tau_x, \tau_y) =$ bed shear stress ($m^2 s^{-2}$),

$\Phi_\omega(X_1, X_2)$ = cross-spectral density between X_1 and X_2 at frequency ω,

$\Phi_\omega(\boldsymbol{X}_1, \boldsymbol{X}_2)$ = cross-spectral matrix between $\boldsymbol{X}_1$ and $\boldsymbol{X}_2$ at frequency ω,

$\Phi_{\omega_1,\omega_2}(X_1, X_2, X_3)$ = cross-bispectral density between X_1, X_2 and X_3 at frequencies ω_1 and ω_2,

$\Phi_{\omega_1,\omega_2,\omega_3}(X_1, X_2, X_3, X_4)$ = cross-trispectral density between X_1, X_2, X_3 and X_4 at frequencies ω_1, ω_2 and ω_3,

φ = normal mode (eigenvector) of edge wave problem,

$\chi = 2kx$,

ω = frequency (s^{-1}),

$\omega_c = \omega/(2\pi) =$ cyclic frequency (s^{-1}),

ω_n = resonant frequency of mode n edge wave (s^{-1}).

Acknowledgements

First, I'd like to thank my supervisor, Dr. Tony Bowen. Tony has been insightful, patient, generous, and a pleasure to work with — an excellent supervisor.

Bob Guza and Steve Elgar provided the data for Chapter 3 of this thesis, and have made many helpful suggestions. Steve Elgar helped me write the paper on which Chapter 3 is based.

Thanks to my committee (Keith Thompson, Barry Ruddick, Alex Hay, Bruce Smith, Paul Hill) for their helpful comments.

Many thanks to all those who helped collect the Sandyduck data on which Chapter 2 is based, and who've also helped me enjoy my time at Dalhousie: Alex Hay, Carolyn Smyth, Todd Mudge, Anna Crawford, Dave Hazen, Wes Paul, Phil MacAulay, Dianne Foster, Walter Judge, and Xingping Zou. Thanks also to the staff at the Field Research Facility at Duck, who helped collect data used in both Chapters 2 & 3.

My research was funded by the Izaak Walton Killam Foundation, the Andrew Mellon Foundation, and the Natural Sciences and Engineering Research Council of Canada.

Thanks to Christine Pequignet, Karin Bryan and Conrad Pilditch for making me so welcome when I arrived at Dalhousie. I've enjoyed chatting with my work-mates Armani Ngusaru and Keith Borg, and paddling with Mark Richard and Brian May. Finally, thanks to Mum, Dad, and Alison for their support.

Chapter 1

Introduction

1.1 What is surf beat?

Strong winds blowing over the deep ocean generate large waves with periods between about 5 and 15 seconds. When these waves approach a beach, they grow taller and eventually break. The energy of the incoming waves is then transfered to turbulence in spectacular fashion. Often the resulting loss of wave energy is almost total, and only a small remnant of each incident wave finally reaches the shore.

Hidden among the broken waves near the shore are lower frequency (0.005–0.05 Hz) waves called 'infragravity waves' or 'surf beat'. These waves are not eye-catching, because they have long periods and change the sea level only slowly. However, unlike breaking incident waves, surf beat actually gets bigger as the shore is approached. At the shore, surf beat often is bigger than breaking incident waves. Figure 1.1 shows a power spectrum of the sea level at the shore, measured on an Oregon beach by Holman and Bowen (1984). On this occasion surf beat accounted for 99.9% of sea level variance at the shore.

During storms, surf beat can change the sea level at the shore by more than a meter. Consequently, surf beat contributes to coastal flooding. Surf beat might also transport sand, and thereby erode or build a beach (Bowen and Inman, 1971; Guza and Inman, 1975; Short, 1975; Bowen, 1981; Holman and Bowen, 1982; Bauer and Greenwood, 1990; Howd *et al.*, 1992; O'Hare and Huntley, 1994; Bryan and Bowen, 1996; Vittori *et al.*, 1999).

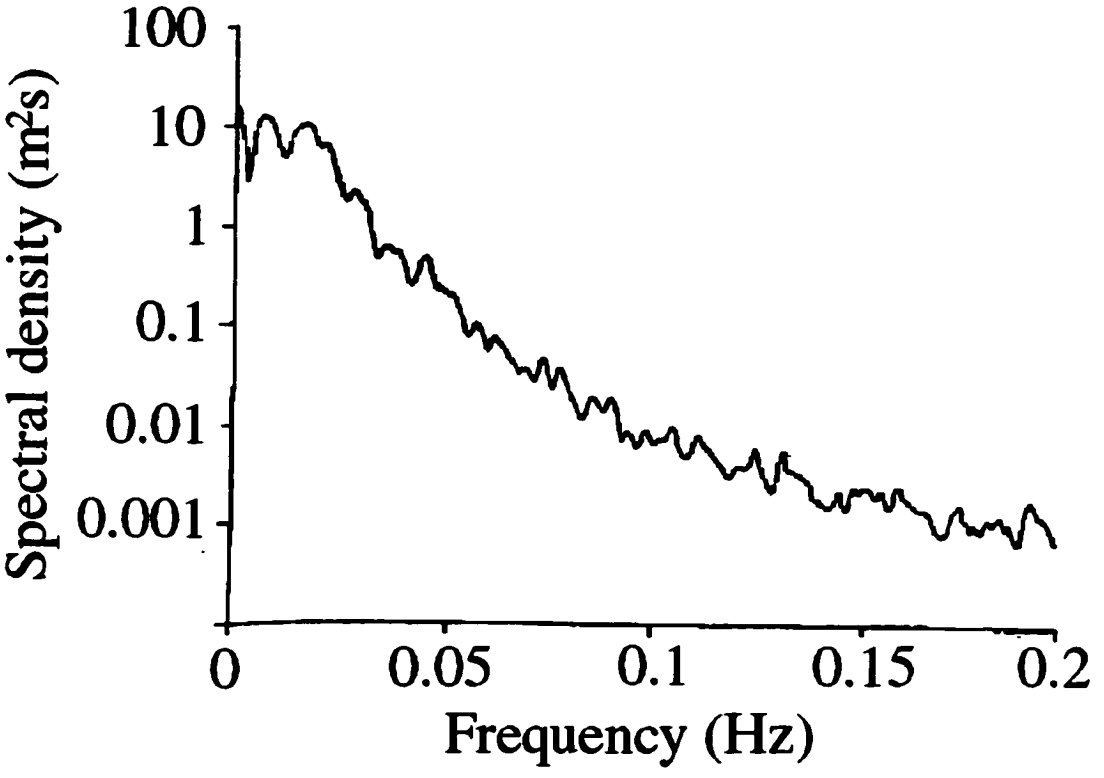

Figure 1.1: Power spectrum of sea level at the shore, measured on an Oregon beach by Holman and Bowen (1984) (their fig.4).

Furthermore, surf beat might control the location of the dangerous, seaward flowing 'rip currents' that are common near the shore (Bowen, 1969a, 1969b; Holman and Bowen, 1984; Symonds and Rangasinghe, 2001).

The dynamics of surf beat are not well understood. Published comparisons between surf beat models and field observations are rather qualitative, and sometimes reveal major discrepancies between predicted and observed behaviour (Ruessink, 1998b; Lippmann *et al.*, 1998, 2001). In this thesis, I present my Ph.D. research into surf beat dynamics. I will emphasise the surprisingly strong effects of dissipation on surf beat behaviour.

1.2 Edge waves, surf beat resonance, and dissipation

This section describes the two types of freely-propagating surf beat that exist on natural beaches. I also discuss surf beat resonance, and note the importance of damping in limiting the height of resonant waves.

Surface waves propagate more slowly in shallow water than in deep water. Consequently, shore-oblique waves refract towards the shore. Certain seaward-propagating waves, called edge waves, are turned back towards the shore by refraction. They then propagate shorewards until they reach the beach, reflect, and propagate back out to sea. Ideally, the cycle of refraction and reflection continues indefinitely, so that edge wave energy is forever trapped near the shore (Eckart, 1951; Ursell, 1952). The interference pattern produced by incoming and outgoing freely-propagating edge waves moves along the coast at a speed determined by the wave frequency[1].

Not all waves are trapped near the shore. Surface waves that can propagate freely to and from the deep ocean are called leaky waves. Near the beach, leaky waves propagate almost directly shorewards or seawards, with wave crests almost parallel to the shore. Consequently, leaky waves have very long longshore wavelengths. For example, all 40 s leaky waves have longshore wavelengths greater than about 2.5 km. Edge waves propagate at greater angles to the shore, and have shorter longshore wavelengths.

[1] In fact a finite set of longshore speeds is possible at each frequency, with each speed corresponding to a single edge wave mode (Appendix F).

Surf beat is generated by nonlinear interactions with higher frequency waves. Just as turbulent eddies exert a Reynolds stress, and particles of an ideal gas in random thermal motion exert a pressure, water waves exert a stress called the 'radiation stress'. Spatial gradients of the radiation stress force water from regions where waves are big to regions where waves are small (this is not the whole story — the radiation stress tensor is anisotropic, and dissipative waves can force non-divergent, rotational flows). On natural beaches the wave height changes slowly through time, and the resulting slow changes in the radiation stress force surf beat (the mass transported by the incident waves might also play a role — see Chapter 4). Nonlinear forcing is usually thought of as a source of surf beat energy, but nonlinear forcing could also oppose low frequency motions, and thereby damp surf beat (Schäffer, 1993; Van Dongeren *et al.*, 1996). However, surf beat energy must somehow be maintained in the presence of frictional dissipation, so the net, cross-shore integrated, effect of nonlinear interactions is probably to add energy to surf beat.

The longshore structure of surf beat forcing can be viewed as a random superposition of many Fourier components, each with its own frequency and longshore phase speed. Those components of the total forcing that have the frequency and longshore phase speed of a freely-propagating edge wave generate resonant edge waves. Since edge waves can not radiate energy to deep water, resonant edge waves on a longshore-uniform beach grow until some damping mechanism limits their amplitude. In contrast, when leaky waves are forced, they radiate their energy into the deep ocean, and do not resonate[2].

Surf beat damping is not understood. Several researchers have suggested mechanisms that could damp surf beat, including bottom friction (Guza and Davis, 1974; Lippmann *et al.*, 1997), wave breaking (Bowen, 1977; Schäffer, 1993; Van Dongeren *et al.*, 1996) and propagation of nonlinearly-forced higher frequency waves to deeper water (Guza and Bowen, 1976a; Mathew and Akylas, 1990). The energy of edge waves propagating over an irregular seabed might also be scattered to leaky waves, and then radiated to the deep ocean (Chen and Guza, 1999). These theories have not been tested against field observations

[2]At least, leaky waves do not resonate with quadratic nonlinear forcing, because they are orthogonal to such forcing in deep water. They do resonate with higher order nonlinear forcing, but this forcing seems to be too weak to generate the large beat-frequency waves observed inside the surf zone

and, because wave breaking is not fully understood, it is not known which of the possible dissipation mechanisms is most important.

If dissipation was very weak, then resonant edge waves would grow to be very large, and eventually dominate over non-resonant waves. However, if dissipation was strong then the effects of forcing could not accumulate over many wave periods, so resonance would be suppressed. The degree to which a resonant edge wave mode dominates over non-resonant modes is determined in part by the parameter

$$Q = 2\pi \frac{\text{Total energy of mode}}{\text{Energy of mode dissipated in a single wave period}}, \tag{1.1}$$

(Green, 1955). Note that Q is approximately the time scale for wave dissipation divided by the wave period, so a low Q indicates rapid dissipation, whereas a high Q indicates slow dissipation. Only if $Q \gg 1$ can the effects of forcing accumulate over many wave periods, generating a strong resonant response.

Field observations indicate that much surf beat energy is carried by waves which have the frequencies and longshore wavelengths of resonant edge waves (Munk *et al.*, 1964; Huntley *et al.*, 1981; Oltman-Shay and Guza, 1987). Similar evidence indicates that resonant edge waves can be trapped over offshore sand bars, at both infragravity and incident frequencies (Schönfeldt, 1995; Bryan and Bowen, 1996; Bryan *et al.*, 1998). These observations provide compelling evidence that edge waves do indeed resonate, and that the Q of infragravity edge waves is often greater than one. However, it is not clear just how large Q is. Indeed, several theories that neglect resonance entirely have successfully predicted aspects of surf beat behaviour that resonant edge wave theories do not predict.

Longuet-Higgins and Stewart (1962) and Hasselmann *et al.* (1963) showed that groups of waves propagating over a flat seabed nonlinearly force low frequency 'bound waves', which propagate with the wave groups. The models of Longuet-Higgins and Stewart (1962) and Hasselmann *et al.* (1963) assume a flat seabed, and therefore do not simulate refractive trapping and edge wave resonance (although they could be extended to do so (Herbers *et al.*, 1995a)). Nevertheless, the average phase between surf beat and short-wave energy departs only slightly from the 180 degrees predicted by these models. Furthermore, up to half of the surf beat variance observed near the shore is coherent with co-located nonlinear

forcing (Huntley and Kim, 1984; Guza *et al.*, 1984; Elgar and Guza, 1985a; Middleton *et al.*, 1987; Masselink, 1995; Ruessink, 1998a, 1998b). Strongly-resonant edge waves accumulate energy over many wave periods, so only a small proportion of their energy is forced locally. The strong coherence between surf beat and co-located nonlinear forcing lead Huntley and Kim (1984) and Middleton *et al.* (1987) to conclude that the surf beat energy they observed was distributed fairly evenly between locally-forced bound waves, and remotely-forced 'free' waves. Further offshore ($\geq$ 8 m water depth) only a small proportion of low frequency energy can be explained by local nonlinear forcing, although this proportion does increase during storms (Okihiro *et al.*, 1992; Elgar *et al.*, 1992; Herbers *et al.*, 1994, 1995b). Munk *et al.* (1964) found that strongly resonant (high Q) edge waves dominated the infragravity energy they observed in 7 m water depth on the Californian Continental Shelf.

1.3 Surf beat propagation and energy transport

Propagating surface gravity waves carry an energy flux. If the group velocity of the propagating waves is much greater than the mean water velocity, as is usually the case in the field, then this energy flux is carried in the direction of wave propagation. A steady surface wave field carries energy from regions of net forcing to regions of net dissipation, so wave propagation is linked closely with wave forcing and dissipation.

In the absence of forcing and dissipation, both edge and leaky waves are cross-shore standing, and carry no cross-shore energy flux. If Q is sufficiently high, edge waves are cross-shore standing (Chapter 4). Leaky waves can propagate across-shore, even when Q is very high (Schäffer, 1993; Van Dongeren *et al.*, 1996).

Sea and swell are mostly dissipated by breaking before they reach the shore. Consequently, sea and swell waves are reflected only very weakly from the shore, and propagate shorewards. In contrast, surf beat can be strongly reflected from the shore to form a cross-shore standing pattern. Holman (1981), Holland *et al.* (1995), and others presented field evidence for the existence of cross-shore standing waves at beat frequencies in water depths

less than 4 m. However, they did not show that these cross-shore standing waves dominated over progressive waves. Elgar *et al.* (1994) and Herbers *et al.* (1995a) presented field evidence of significant net cross-shore surf beat propagation in 13 m water depth.

1.4 Thesis outline

If dissipation is very weak, then cross-shore standing, resonant edge waves dominate surf beat. Edge wave resonance has been observed in the field, but the rate of surf beat dissipation, and the strength of edge wave resonance, are not known. Furthermore, observations of strong correlations between surf beat and local nonlinear forcing suggest that surf beat might not always be dominated by strongly-resonant edge waves.

This thesis aims to determine some of the major effects of dissipation on surf beat. Surf beat dissipation is linked closely with surf beat forcing, and some observations of surf beat forcing will also be presented. In Chapter 2, I use measurements of water pressure and velocity to estimate the rate of net surf beat dissipation (or forcing) on a natural beach. When incident waves were small, net dissipation was weak. When incident waves were large, net dissipation in the surf zone was very strong. Chapter 3 presents observations of the cross-shore structure of surf beat. Surf beat propagated shorewards into the surf zone when incident waves were large. The observed shoreward surf beat propagation constitutes a leading-order departure from the predictions of weakly-dissipative edge wave models. Chapter 4 presents a dissipative surf beat model which predicts shoreward propagation, in qualitative agreement with observations. Recently, model simulations lead to the recognition of a type of shoreward-propagating wave that I had previously neglected — the 'evanescent bound wave'. Evanescent waves are introduced in Chapter 4.2.3. I do not know yet whether evanescent waves play an important role in the field.

Chapter 2

The surf beat energy balance

2.1 Introduction

This chapter presents observations of the approximate strength of surf beat forcing and dissipation. Section 2.2 presents a simple energy balance equation for surf beat. This energy balance equation can be combined with measurements of water pressure, velocity, and depth to yield spatially-averaged rates of net surf beat forcing (or dissipation). This method provides estimates of the difference between surf beat forcing and dissipation, but does not allow us to evaluate forcing and dissipation separately. I will use the method developed in Section 2.2 to analyse data collected from a beach near Duck, North Carolina. Section 2.3 describes the field site and instrumentation. Results are presented in Section 2.4. Net surf beat forcing (or dissipation) was strong when incident waves were large and weak when incident waves were small. Forcing exceeded dissipation outside the surf zone and dissipation exceeded forcing inside the surf zone. During storms, a shoreward surf beat energy flux maintained surf beat energy inside the surf zone. I discuss the implications of these results and present conclusions in Section 2.5. Related results were presented by Henderson and Bowen (2002).

2.2 Energy equation

Schäffer (1993) derived an energy balance equation for surf beat by assuming that beat frequencies are much lower than incident-wave frequencies. Section 2.2.1 shows that a slightly modified form of Schäffer's energy equation applies even when beat frequencies are not much lower than incident wave frequencies. This result is useful because beat frequencies often are not much lower than incident-wave frequencies (surf beat frequencies are as high as 0.05 Hz and the peak frequency of incident waves is often only 0.1 Hz). Section 2.2.2 presents a simpler energy equation for a statistically steady wave field on a long, straight beach. The following definitions will be needed throughout this chapter:

$$t = \text{time}, \tag{2.1}$$

$$x_j = j\text{'th horizontal coordinate } (j = 1 \text{ or } 2), \tag{2.2}$$

$$\boldsymbol{u} = \text{horizontal water velocity}, \tag{2.3}$$

$$u_j = j\text{'th component of } \boldsymbol{u}, \tag{2.4}$$

$$h = \text{still water depth}, \tag{2.5}$$

$$\eta = \text{sea surface elevation (above still water level)}, \tag{2.6}$$

$$g = \text{gravitational acceleration}. \tag{2.7}$$

When analysing field data I will estimate h as the mean measured water depth, implicitly assuming that the mean depth approximately equals the still depth, which it does.

2.2.1 Energy balance in differential form

For any variable X, let $\langle X \rangle_\omega$ be the time-varying complex amplitude of a frequency ω Fourier component of X, so

$$X(t) = \sum_{j=-\infty}^{\infty} \mathrm{e}^{\mathrm{i}(j\,\Delta\omega)t} \langle X \rangle_{j\,\Delta\omega}, \tag{2.8}$$

where

$$\Delta\omega = 2\pi/\Delta t \tag{2.9}$$

is the frequency resolution, and

$$\langle X \rangle_\omega = \frac{1}{\Delta t} \int_{t'=t-\Delta t/2}^{t+\Delta t/2} \mathrm{e}^{-\mathrm{i}\omega t'} X(t')\, dt' \tag{2.10}$$

is the complex amplitude of a frequency ω sinusoid fitted to a length Δt segment of X centered on time t. Note that $\langle X \rangle_\omega$ is a function of time t. I consider only real-valued time series, so $\langle X \rangle_{-\omega}$ is the complex conjugate of $\langle X \rangle_\omega$.

An equation for the time-varying energy of frequency ω surf beat is

$$\frac{\partial \mathcal{E}_{nl}(\omega)}{\partial t} + \nabla \cdot \boldsymbol{w}(\omega) + \mathcal{F}(\omega) + \mathcal{D}(\omega) = 0, \tag{2.11}$$

where

$$\mathcal{E}_{nl}(\omega) = h |\langle \tilde{\boldsymbol{u}} \rangle_\omega|^2 + g |\langle \eta \rangle_\omega|^2, \tag{2.12}$$

$$\boldsymbol{w}(\omega) = 2\Re \left[hg \langle \eta \rangle_\omega \langle \tilde{\boldsymbol{u}} \rangle_{-\omega} \right], \tag{2.13}$$

$$\mathcal{F}(\omega) = 2\Re \left[\langle \tilde{u}_j \rangle_\omega \frac{\partial \langle T_{j,k} \rangle_{-\omega}}{\partial x_k} \right], \tag{2.14}$$

$$\mathcal{D}(\omega) = \text{depth-integrated rate of dissipation at frequency } \omega, \tag{2.15}$$

$$\Re = \text{real part},$$

and

$$\tilde{\boldsymbol{u}} = \boldsymbol{u} + \frac{\boldsymbol{M}}{h}, \tag{2.16}$$

$$T_{j,k} = \int_{-h}^{\eta} u_j u_k\, dz + \delta_{j,k} \int_0^{\eta} \frac{p}{\rho}\, dz, \tag{2.17}$$

$$\boldsymbol{M} = \int_0^{\eta} \boldsymbol{u}\, dz, \tag{2.18}$$

$$\delta_{j,k} = \begin{cases} 1 & j = k \\ 0 & j \neq k \end{cases}. \tag{2.19}$$

The summation convention has been used, so repeated indices are summed over all allowable values. Equation (2.11) is derived in Appendix A.

Equation (2.11) applies to both weakly- and strongly-nonlinear waves. However, in a strongly nonlinear wave field, some energy is shared between waves with different frequencies, and the wave energy at a single frequency is not well defined. Consequently, interpretation of eq. (2.11) is difficult unless nonlinear interactions are weak.

$\tilde{\boldsymbol{u}}$ is the depth-integrated mass transport divided by the still water depth. The momentum flux tensor T contains contributions from both the mean flow and the wave field. Variations in radiation stress (Longuet-Higgins and Stewart, 1964) are included in T. $\boldsymbol{M}$ is the transport between the still water level and the sea surface, and includes the Stokes drift.

$\mathcal{E}_{nl}(\omega)$ is, except for a small Stokes-drift contribution, the depth-integrated energy of a wave with frequency ω. $\boldsymbol{w}(\omega)$ is the the wave energy flux, and represents the depth-integrated rate of working by the water pressure on the water motion. $\mathcal{F}(\omega)$ is the depth-integrated rate of working by the momentum flux gradient on the water motion.

Nonlinear interactions between waves are associated with the momentum flux $\langle T_{j,k} \rangle_\omega$ and Stokes drift $\langle \boldsymbol{M} \rangle_\omega$ terms of eq. (2.11). I outline the statistical description of such interactions in Appendix B.

Equation (2.11) was derived by assuming that beat-frequency pressure fluctuations are hydrostatic (eq. (A.4)), and by neglecting the depth-dependence of beat-frequency fluctuations in horizontal velocity (eq. (A.5)). These assumptions are correct to leading order for Boussinesq surf beat and exact in the shallow water limit. Neglected effects include reductions in water pressure associated with the vertical flux of vertical momentum (which, as I show in the appendix, probably leads to errors of less than 5% in estimates of T), and non-potential flow in the bottom boundary layer (which is negligible if boundary layer thickness is small compared with the water depth). Equation (2.11) is very similar to the energy equation of Schäffer (1993), but does not rely on the assumption that the surf beat period is much longer than the incident wave period.

Let x and y be the cross-shore and longshore coordinates respectively (x positive onshore). Let u and v be the x and y components of the velocity $\boldsymbol{u}$. Applying the expectation operator $E[.]$ to eq. (2.11), assuming stationarity ($\partial E[.]/\partial t = 0$) and longshore homogeneity ($\partial E[.]/\partial y = 0$), and gathering nonlinear terms together into a single term $-\mathcal{N}(\omega)$ gives

$$\frac{\partial E[q_x(\omega)]}{\partial x} + E[\mathcal{D}(\omega)] - E[\mathcal{N}(\omega)] = 0, \tag{2.20}$$

where

$$q_x = 2h\Re\left[g\langle\eta\rangle_\omega\langle u\rangle_{-\omega}\right], \tag{2.21}$$

and

$$\mathcal{N}(\omega) = -2\Re\left[\frac{\partial g\langle\eta\rangle_\omega\langle M_x\rangle_{-\omega}}{\partial x} + \langle\tilde{u}_j\rangle_\omega\frac{\partial\langle T_{j,k}\rangle_\omega}{\partial x_k}\right]. \tag{2.22}$$

In a spatially homogeneous wave field, the first term on the right-hand side of eq. (2.22) vanishes, and the second term represents a nonlinear transfer of energy between waves of different frequencies. In this case, nonlinear energy transfers do not change the total energy at any single location. However, in an inhomogeneous wave field, both of the terms on the right hand side of eq. (2.22) can change the total energy at any single location (this is true regardless of the strength of nonlinearity). Near the surf zone, the water depth changes greatly in a single surf beat wave length, and the surf beat wave field is inhomogeneous. Consequently, the nonlinear term $\mathcal{N}$ probably represents more than just a localised transfer of energy between frequencies, and might change the total energy at any given location.

From eq. (2.21), for a sufficiently long time series, the mean energy flux per unit frequency is

$$q_x' \equiv E[q_x(\omega)]/(\Delta\omega) \approx 2gh\Re[\Phi_\omega(\eta,u)], \tag{2.23}$$

where

$$\Phi_\omega(\eta,u) = \lim_{\Delta\omega\to 0} E[\langle\eta\rangle_\omega\langle u\rangle_{-\omega}]/(\Delta\omega) \tag{2.24}$$

is the density of the cross-spectrum between u and η at frequency ω ($\Delta\omega$ is the frequency resolution defined by eq. (2.9)). Similarly, let

$$\mathcal{D}'(\omega) = \mathcal{D}(\omega)/(\Delta\omega), \tag{2.25}$$

and

$$\mathcal{N}'(\omega) = \mathcal{N}(\omega)/(\Delta\omega). \tag{2.26}$$

Eldeberky and Battjes (1996), Elgar *et al.* (1997), Chen and Guza (1997) and Herbers *et al.* (2000) applied eq. (2.20) to simulate breaking waves, but they assumed shoreward propagation (although Herbers *et al.* (2000) allowed for small departures from this assumption), so to leading order

$$q_x(\omega) = \mathcal{E}(\omega)\, Cg(\omega), \tag{2.27}$$

where

$$\mathcal{E}(\omega) = \int_{z=-h}^{0} |\langle u(z)\rangle_\omega|^2\, dz + g|\langle \eta\rangle_\omega|^2 \tag{2.28}$$

is the linear wave energy density, z = elevation above sea level, and $Cg(\omega)$ = group velocity. The assumption of shoreward propagation is probably a good approximation for the incident wave frequencies to which eq. (2.27) has primarily been applied, but its application to surf beat is not justified. Reflection of surf beat from the shore, broad directional spread, and refractive trapping of edge waves ensure that eq. (2.27) does not apply to surf beat. In contrast, eq. (2.21) allows for reflection and directional spread and is free from these problems.

Large arrays of instruments can be used to estimate directional spectra of infragravity waves. This approach allows for reflection, and therefore can be used to estimate net infragravity energy fluxes. Usually, a spatially-homogeneous wave field is assumed (Herbers *et al.*, 1994, 1995b, 1995a; Elgar *et al.*, 1994). This assumption is not valid very near the shore, where the depth varies rapidly, and the nodal structure of cross-shore standing waves is pronounced. Sheremet *et al.* (2001) showed that the assumption of homogeneity can be relaxed if the infragravity wave field is assumed to be composed of a limited set of uncorrelated modes with phase velocities near $(gh)^{1/2}$. A very large array is required to resolve the wave field (Sheremet *et al.* (2001) used an array of 35 instrumented frames), whereas application of eq. (2.23) requires measurements from only one location. Furthermore, eq. (2.23) has the advantage that no assumptions regarding the horizontal structure of the wave field are required. However, the method of Sheremet *et al.* (2001) has the advantage that the directional properties of the infragravity wave field are resolved. The

results obtained by Sheremet *et al.* (2001) are fascinating, and will be discussed further in Chapter 4.

2.2.2 Energy balance in integral form

Integrating eq. (2.20) from $x = a$ to $x = b$ and applying eq. (2.23) gives

$$q_x'(\omega)|_{x=b} - q_x'(\omega)|_{x=a} + \int_{x=a}^{b} \left(E[\mathcal{D}'(\omega)] - E[\mathcal{N}'(\omega)]\right) dx = 0. \qquad (2.29)$$

Equation (2.29) is an energy balance for statistically steady and longshore-homogeneous waves in the cross-shore region $a \leq x \leq b$ (we are free to chose a and b). The first two terms represent respectively the energy flux carried out of, and into, this region by propagating surf beat. The integral of $\mathcal{D}$ represents the total dissipation between a and b. The integral of $\mathcal{N}$ represents the nonlinear addition of energy to surf beat (it is through this term that groups of incident waves force surf beat). Therefore, eq. (2.29) shows that the net surf beat energy flux out of a cross-shore region equals the excess of forcing over dissipation within the region.

Given measurements of water pressure, water velocity, and mean water depth at two points $x = a$ and $x = b$ in the cross-shore, the net surf beat energy flux out of the region between a and b can be calculated using eq. (2.23). Equation (2.29) can then be solved for the excess of dissipation over forcing (negative if forcing exceeds dissipation) between a and b. Alternatively, we can choose b to be the shoreline, across which there is no flux of surf beat energy. Then the shoreward energy flux at $x = a$ equals the excess of dissipation over forcing onshore of a. Unfortunately, it is difficult to separate the forcing and dissipation terms of eq. (2.29), but the difference between forcing and dissipation still provides useful information.

Equation (2.29) applies at every surf beat frequency, but for simplicity I will integrate eq. (2.29) over all surf beat frequencies to obtain a total surf beat energy balance.

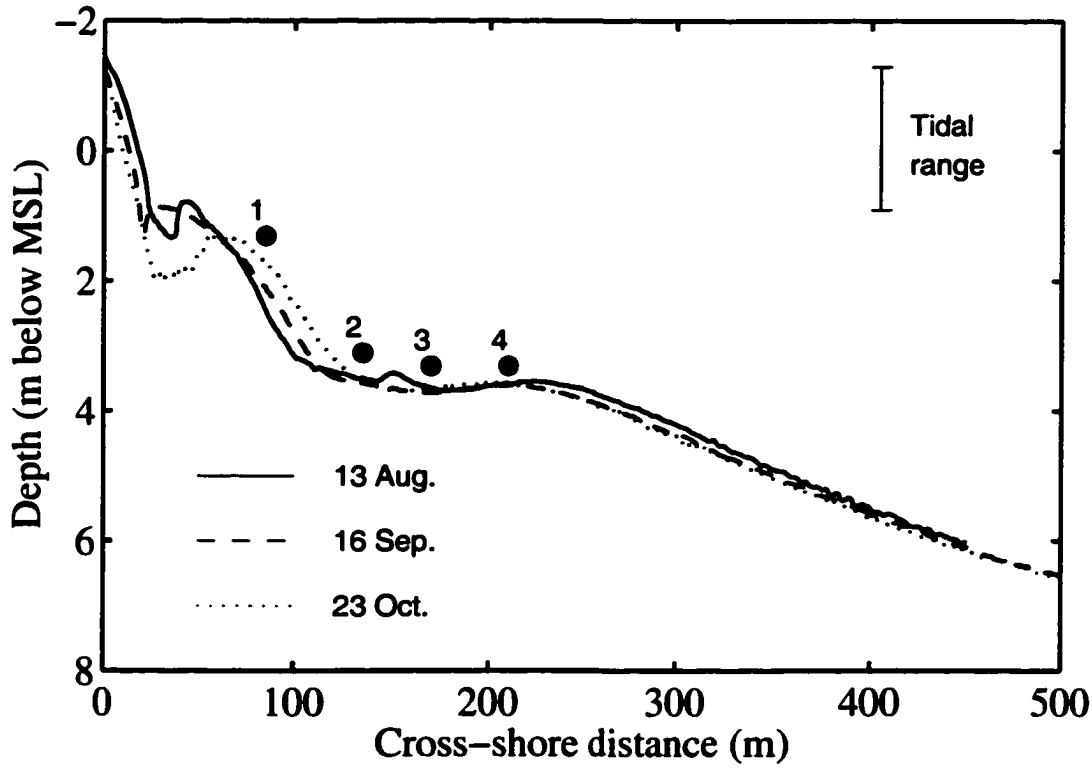

Figure 2.1: Measured beach profiles and location of instrumented frames 1–4.

2.3 Field site and instrumentation

This chapter presents analysis of data collected on an ocean beach near Duck, North Carolina by the Dalhousie nearshore research group during the Sandyduck beach experiment of 1997. Figure 2.1 shows the cross-shore array of four instrumented frames from which the data were collected, together with measured beach profiles. Water pressures and velocities were measured at 2 Hz at every frame. During the Sandyduck experiment, the U.S. Army Corps of Engineers regularly measured sea bed elevation profiles using the Coastal Research Amphibious Buggy (Lee and Birkemeier, 1993). Sea bed elevations beneath the instrumented frames were also measured continuously using sonar altimeters.

2.4 Results

Cross-periodograms between water pressure and velocity were calculated from quadratically-detrended half-hour time series. Spectra of the wave energy flux were estimated by averaging these cross-periodograms and applying eq.'s (2.23) & (A.4). Figure 2.2 shows a spectrum of the shoreward energy flux measured over two hours during a storm on day 293. The shaded region of fig. 2.2 is the surf beat band (0.005–0.05 Hz). For every half-hour of the experiment, I estimated the total surf beat energy flux q_{sb} by integrating raw cross-periodograms between pressure and velocity over the entire surf beat band and multiplying by the water depth h. Other statistics, such as significant wave height and the beat-frequency sea level variance, were also calculated every half hour. I estimated sea surface elevations from water pressure measurements using linear wave theory. The significant wave height was calculated as $4\,\overline{\eta_w^2}^{1/2}$, where the overbar denotes a sample mean, and $\overline{\eta_w^2}$ is the estimated sea level variance due to waves with frequencies greater than 0.05 Hz.

Equation (2.29) neglects the longshore gradient of the longshore energy flux. The ratio of the longshore flux gradient to the cross-shore flux gradient is

$$R = \left| \frac{\partial q_y / \partial y}{\partial q_x / \partial x} \right| \approx \left| \frac{q_y}{q_x} \right| \frac{L_x}{L_y}, \tag{2.30}$$

where

q_y = longshore component of surf beat energy flux,

L_x = cross-shore length scale over which q_x varies,

L_y = longshore length scale over which q_y varies.

Since the beach at Duck is long and straight, I assume $L_x/L_y < 1$. When incident waves were large, the observed longshore surf beat energy flux was usually an order of magnitude smaller than the cross-shore surf beat energy flux. When incident waves were small, the longshore and cross-shore energy fluxes were of the same magnitude. Therefore, when incident waves were large $R \ll 1$, so the longshore-uniform approximation made in the derivation of eq. (2.20) was reasonable. I can not be sure how accurate the longshore-uniform approximation was when incident waves were small.

Figure 2.3 shows the time series of significant wave height, surf beat sea level variance, and shoreward surf beat energy flux, measured at frame 4. Similar results were obtained from the other three frames. Surf beat energy increased with increasing significant wave height, consistent with the findings of Tucker (1950), Holman (1981), Guza and Thornton (1985), and others. The surf beat energy flux was directed onshore in 86% of cases, suggesting that the nearshore zone (<3.5 m depth) was usually a region of net surf beat dissipation during the Sandyduck experiment (eq. (2.29)). Shoreward energy fluxes were most pronounced when incident waves were large — when the significant wave height was greater than 1 m the surf beat energy flux was always directed onshore. The observed shoreward energy flux does not imply that surf beat forcing was weak near the shore, but it does imply that dissipation was usually stronger than forcing.

During the Sandyduck experiment, incident wave (0.05–0.33 Hz) energy fluxes ranged from 0.08 m^4s^{-3} to 12 m^4s^{-3}, and were always directed onshore.

Figure 2.4 shows the significant wave height Hs as a function of water depth at frames 1 and 4. Wave heights were limited by breaking, as described by the relation

$$Hs \leq \gamma h, \tag{2.31}$$

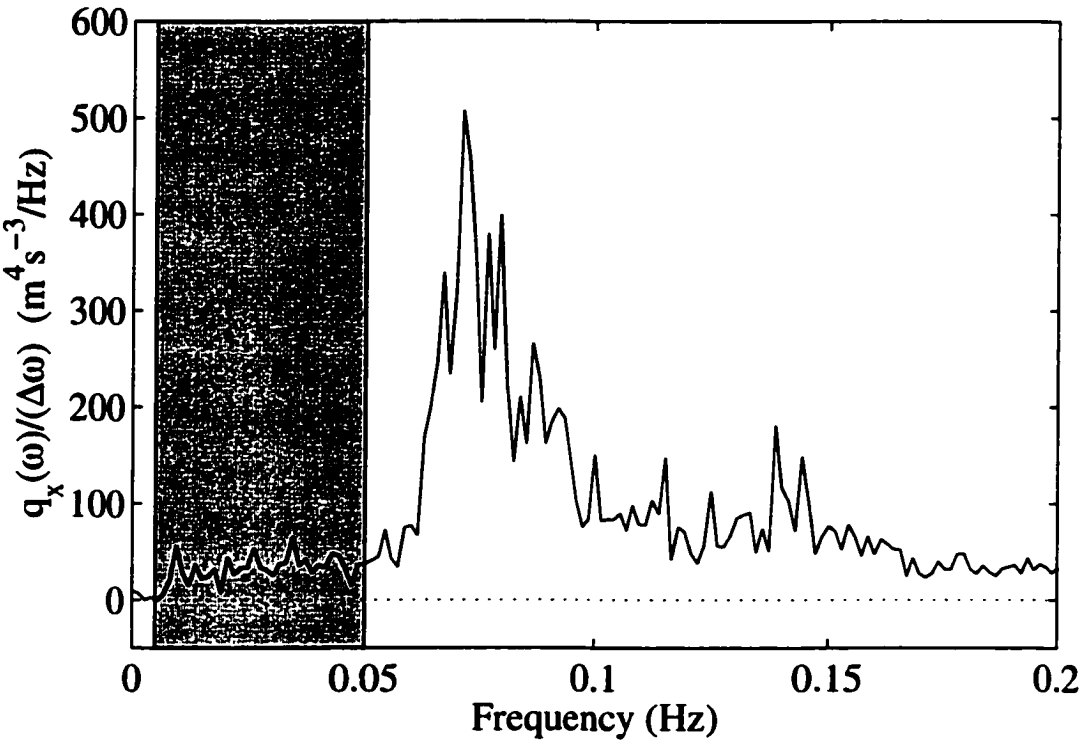

Figure 2.2: Spectrum of the energy flux density $q_x(\omega)/(\Delta\omega)$ at frame 1 for a two hour period following 10:30pm on day 293, estimated using eq. (2.23). The shaded region is the surf beat band. The co-spectral estimates have 10 dof.

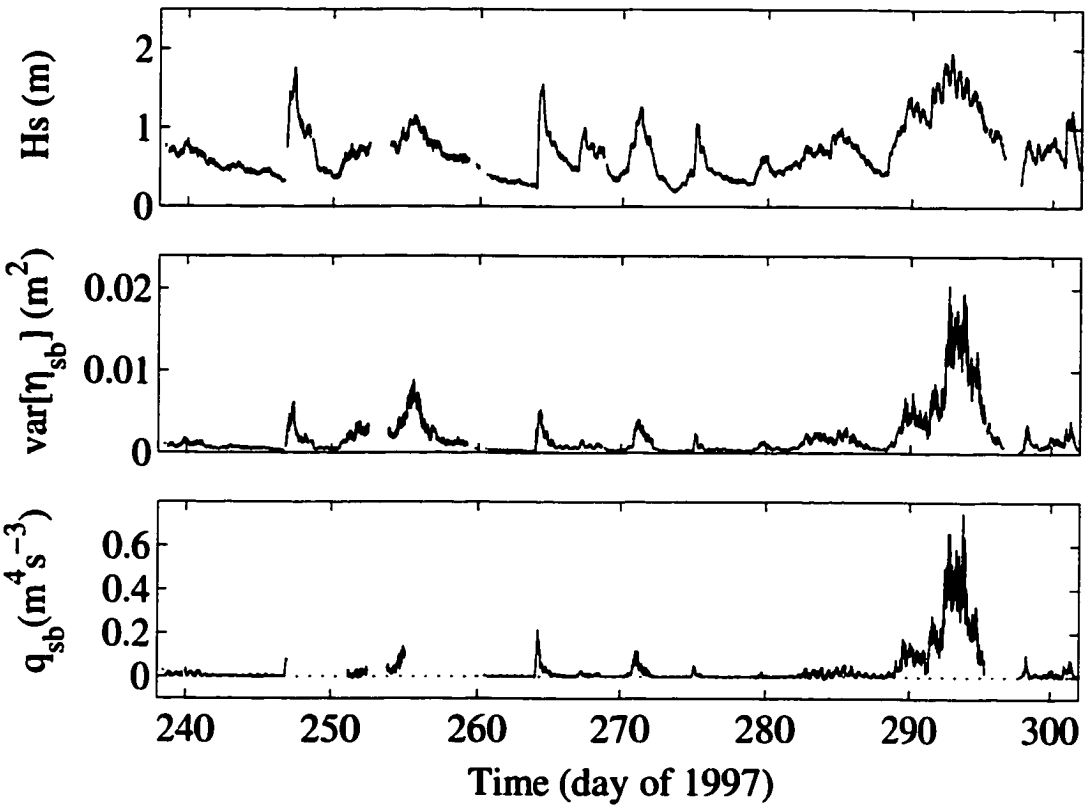

Figure 2.3: Time series of half-hourly significant wave height, Hs, surf beat sea level variance, $\overline{\eta_{sb}^2}$, and shoreward surf beat energy flux, q_{sb}, during Sandyduck at frame 4 ($\approx$ 3.5 m depth).

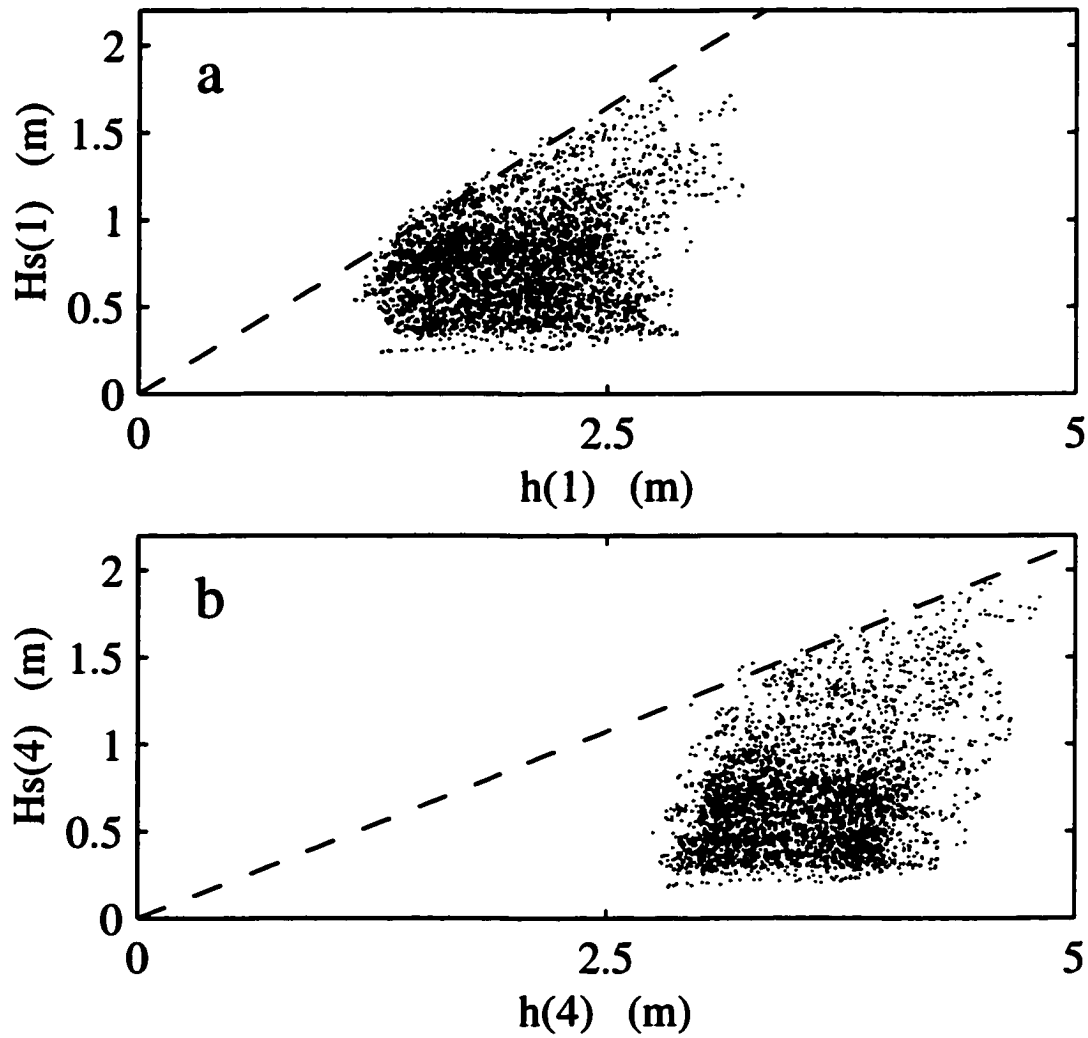

Figure 2.4: Significant wave height, *Hs*, *versus* water depth, h. a: frame 1. b: frame 4. Dashed line is $Hs = \gamma h$, where γ is 0.66 at frame 1 and 0.43 at frame 4. Each data point is estimated from a half-hour time series segment.

where the breaker-ratio γ (chosen to fit the data) equals 0.66 at frame 1 and 0.43 at frame 4. Sallenger and Holman (1985) and Raubenheimer *et al.* (1996) discuss the application of eq. (2.31) to the surf zone at Duck. In order to determine approximately whether frame 1 was inside or outside the saturated surf zone, I define the shoaled significant wave height

$$Hs' = [h(4)/h]^{1/4} Hs(4), \tag{2.32}$$

where $Hs(4)$ and $h(4)$ are the significant wave height and water depth at frame 4, and h is the local water depth. Hs' is the wave height that would be observed given linear, non-dissipative shoaling of shore-normal shallow water waves. Roughly, frame 1 is inside (outside) the saturated surf zone when Hs'/h is greater than (less than) γ at frame 1. At frame 4, $Hs' = Hs$.

The shoreward surf beat energy flux shown in fig. 2.3 implies some shoreward propagation of surf beat. Let

$$\rho = \frac{q_{sb}}{\mathcal{E}_{sb}(gh)^{1/2}}, \tag{2.33}$$

where $\mathcal{E}_{sb}$ is the total linear surf beat energy density. ρ is the ratio between the actual surf beat energy flux, calculated from eq. (2.23), and the surf beat energy flux expected for a purely shore-normal, shoreward-propagating wave, calculated from eq. (2.27). If all surf beat propagates directly shorewards $\rho = 1$, if all surf beat propagates directly seawards $\rho = -1$, and if all surf beat is standing in the cross-shore $\rho = 0$. Directional spreading of waves (away from shore-normal) reduces the magnitude of ρ. I estimated the total surf beat energy density as twice the potential energy density, or

$$\mathcal{E}_{sb} = g\,\overline{\eta_{sb}^2}, \tag{2.34}$$

where $\overline{\eta_{sb}^2}$ is the estimated sea surface elevation variance due to surf beat. The use of eq. (2.34) introduced errors into $\mathcal{E}_{sb}$ estimates, but allowed separation of surf beat (gravity wave) energy from the shear wave energy that often contributes a large proportion of the total low frequency kinetic energy (Lippmann *et al.*, 1999). Figure 2.5 shows the observed dependence of ρ on the non-dimensional shoaled wave height Hs'/h. When the

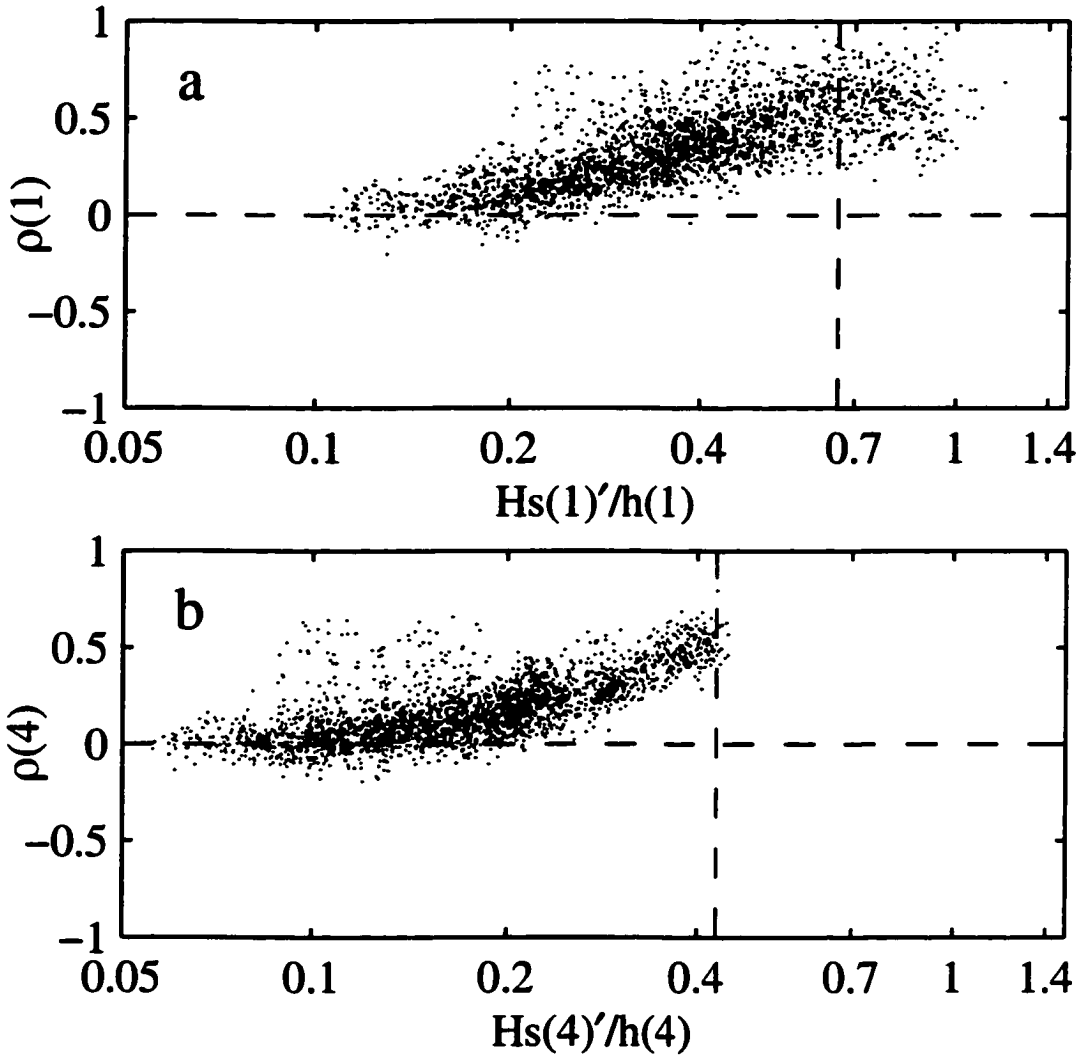

Figure 2.5: Onshore-progressiveness of surf beat, $\rho = q_{sb}/(\mathcal{E}_{sb}\, Cg)$, *versus* shoaled significant wave height (eq. (2.32)) divided by water depth, Hs'/h. a: frame 1. b: frame 4. The vertical dashed lines indicate $Hs'/h = \gamma$. Each data point is estimated from a half-hour time series segment.

non-dimensional wave height was small, $\rho \approx 0$ and surf beat was approximately standing in the cross-shore. When the non-dimensional wave height was large, $\rho > 0$ and there was a significant shoreward-propagating component of surf beat.

The observed net surf beat dissipation is consistent with a standard bottom stress parameterisation. The dissipation of the energy of a frequency ω wave by bottom friction is

$$\mathcal{D}(\omega) = f_e |\boldsymbol{u}| |\langle \boldsymbol{u} \rangle_\omega|^2, \tag{2.35}$$

where f_e is a dimensionless energy dissipation factor. Values of f_e observed in the field for incident-frequency waves are usually in the range 0.01–1 (Sleath, 1984).

Let $\boldsymbol{\tau} = (\tau_x, \tau_y)$ be the bed shear stress divided by the water density. Feddersen *et al.* (1998) showed that the drag force (divided by the water density) retarding the mean longshore current, $\overline{v}$, at Duck is

$$\overline{\tau}_y = c_f |\boldsymbol{u}| \overline{v},$$

where the bottom drag coefficient, c_f, is roughly 0.001 outside the surf zone and 0.003 inside the surf zone. Applying the same parameterisation to surf beat

$$\begin{aligned} \langle \boldsymbol{\tau} \rangle_\omega &= c_f |\boldsymbol{u}| \langle \boldsymbol{u} \rangle_\omega , \\ \Rightarrow \mathcal{D}(\omega) = \langle \boldsymbol{\tau} \rangle_\omega \cdot \langle \boldsymbol{u} \rangle_{-\omega} &= c_f |\boldsymbol{u}| |\langle \boldsymbol{u} \rangle_\omega|^2. \end{aligned} \tag{2.36}$$

Equation (2.36) differs from eq. (2.35) only in the magnitude of the non-dimensional coefficient — dissipation factors for waves are one or two orders of magnitude larger than drag coefficients for the mean current (Nielsen, 1992).

From eq.'s (2.35) & (2.36), the total dissipation of surf beat energy by bottom drag scales with

$$\overline{|\boldsymbol{u}|^2}^{1/2} \, \overline{|\boldsymbol{u}|^2}_{sb}, \tag{2.37}$$

where $\overline{|\boldsymbol{u}|^2}_{sb}$ is the contribution to velocity variance from surf beat frequencies. To separate gravity wave dissipation from shear wave dissipation, I re-write eq. (2.37) in terms of the

sea surface elevation variance. For gravity waves in shallow water (Lippmann *et al.*, 1999)

$$\overline{|\boldsymbol{u}|^2} \approx g\overline{\eta^2}/h,$$
$$\Rightarrow \overline{\mathcal{D}(\omega)} \approx f_e(g/h)^{3/2}\,\overline{\eta^2}^{1/2}\,\overline{\eta^2}_{sb}. \tag{2.38}$$

From eq.'s (2.29) and (2.38)

$$q_{sb}|_{x=a} \approx \int_{x=a}^{shore} \left(f_e(g/h)^{3/2}\,\overline{\eta^2}^{1/2}\,\overline{\eta^2}_{sb} - E[\mathcal{N}_{sb}]\right) dx. \tag{2.39}$$

Figure 2.6 shows that the shoreward surf beat energy flux at frame 1 scales with $\overline{\eta^2}^{1/2}\,\overline{\eta^2}_{sb}$ ($r^2 = 0.92$), as predicted by eq. (2.39) if the nonlinear energy exchange to the surf beat band, $\mathcal{N}_{sb}$, is neglected. An order of magnitude estimate for f_e is

$$f_e \approx \frac{\alpha}{(g/h)^{3/2} l}, \tag{2.40}$$

where l is the distance from frame 1 to the shore, α is the slope of the dashed line in fig. 2.6, and h is a typical water depth shoreward of frame 1 (taken to be half the depth at frame 1). Applying eq. (2.40) gives $f_e \approx 0.08$, which is a normal value for a wave dissipation factor and is 27–80 times larger than the drag coefficients Feddersen *et al.* (1998) found were appropriate for the mean longshore current.

About a year after finishing the above analysis, I discovered that the observed correlation between net damping and predicted frictional dissipation could be misleading This is because the magnitude of nonlinear working on surf beat is strongly correlated with the estimated frictional dissipation. From eq. (2.38), frictional dissipation scales with $\overline{\eta^2}^{1/2}\,\overline{\eta^2_{sb}}$. The nonlinear working on surf beat scales with $\overline{\eta^2}\,\overline{\eta^2_{sb}}^{1/2}$. Therefore, the ratio between nonlinear working and frictional dissipation scales with the ratio between the incident wave height and the surf beat height, i.e. $(\overline{\eta^2}/\overline{\eta^2_{sb}})^{1/2}$. But it is well known (Guza and Thornton, 1985, and others) that the height of surf beat is roughly proportional to the height of incident waves. Consequently, the magnitude of the nonlinear working on surf beat is roughly proportional to the predicted frictional dissipation. Therefore, the correlation presented in fig.2.6 might be due to nonlinear energy transfer from surf beat to higher frequency waves. I discovered this result by accident, when I found that the net energy *gained* by surf beat

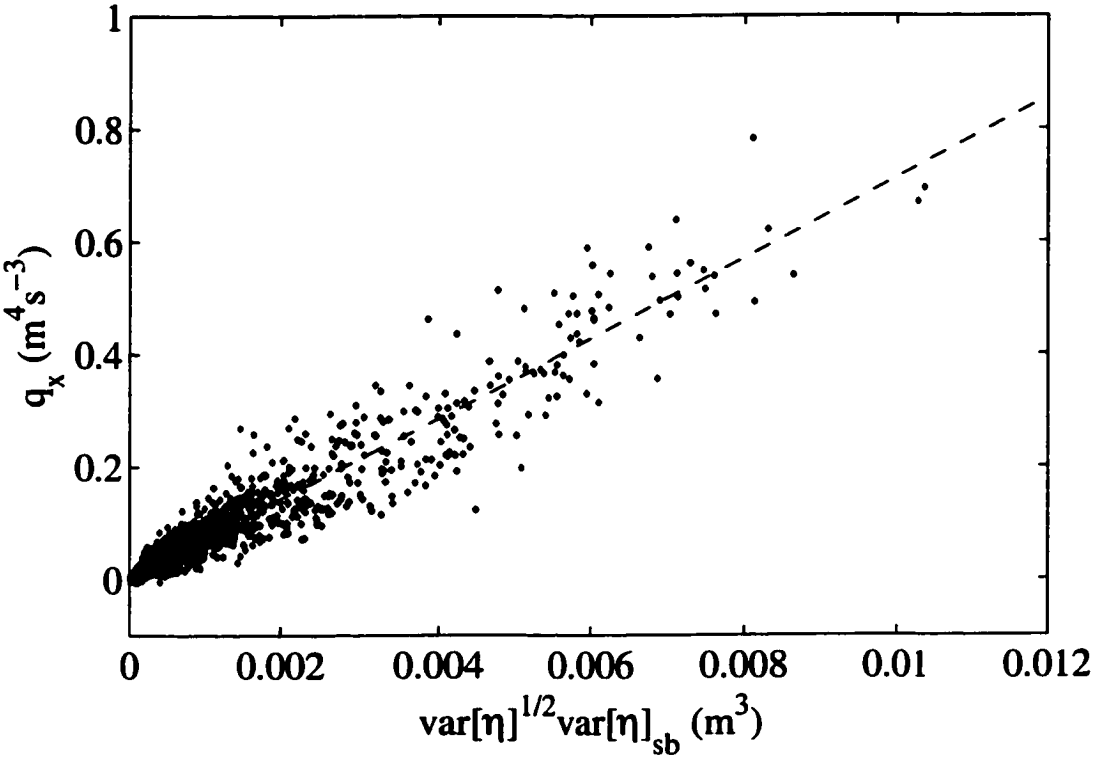

Figure 2.6: Onshore surf beat energy flux, q_{sb}, *versus* $\overline{\eta^2}^{1/2}\overline{\eta_{sb}^2}$ at frame 1. Dashed line is $q_{sb} = \alpha\,\overline{\eta^2}^{1/2}\overline{\eta_{sb}^2}$, with α chosen to give least-squares fit. Each data point is estimated from a half-hour time series segment.

outside the surf zone was strongly correlated with estimated frictional dissipation. Both bottom friction and nonlinear damping might account for the observed dissipation, but we can not determine which was most important from correlations of the sort shown in fig. 2.6.

Section 1.2 introduced Q as a measure of the strength of surf beat dissipation. Since I can measure only spatially-averaged net forcing or dissipation, I can not measure Q values for individual surf beat modes. Instead, I define the net forcing strength

$$\Omega = \frac{\text{Net surf beat energy generated in one beat period}}{\text{Total surf beat energy}}, \tag{2.41}$$

$$\Rightarrow \Omega = \frac{\int_{x=a}^{b} \left(E[\mathcal{N}_{sb}] - E[\mathcal{D}_{sb}]\right) dx}{\omega \int_{x=a}^{b} \mathcal{E}_{sb}\, dx}.$$

From eq. (2.29)

$$\Omega \approx \frac{q_{sb}|_{x=b} - q_{sb}|_{x=a}}{(0.025Hz) \int_{x=a}^{b} \mathcal{E}_{sb}\, dx}, \tag{2.42}$$

where $0.025Hz$ has been chosen as a typical surf beat frequency. Since this 'typical' beat frequency was chosen somewhat arbitrarily, only the sign and order of magnitude of Ω are significant. Where possible I estimated the integral in eq. (2.42) using the trapezoidal rule. To estimate the integral between frame 1 and the shore, I multiplied the energy density at frame 1 by the distance to the shore. The energy density $\mathcal{E}_{sb}$ was estimated using eq. (2.34).

Ω is positive (negative) if total forcing exceeds total dissipation (dissipation exceeds forcing) between $x = a$ and $x = b$. If $|\Omega|$ is order one, then the surf beat energy forced (or dissipated) between $x = a$ and $x = b$ in a single beat period is of the same order as the total amount of surf beat energy stored between $x = a$ and $x = b$. If $|\Omega| \ll 1$, then net forcing (or dissipation) is weak, but this does not imply that actual forcing and dissipation are weak. If strong forcing and strong dissipation happen to cancel, then $\Omega \ll 1$. Therefore, large $|\Omega|$ values indicate strong forcing or dissipation, whereas small $|\Omega|$ values are ambiguous.

Figure 2.7a shows the estimated strength of net surf beat forcing, Ω, for the region between frames 1 and 4. Figure 2.7b shows Ω for the region between frame 1 and the shore. The vertical dashed lines indicate the non-dimensional wave height at which frame 1 is approximately on the edge of the saturated surf zone. When incident waves were small,

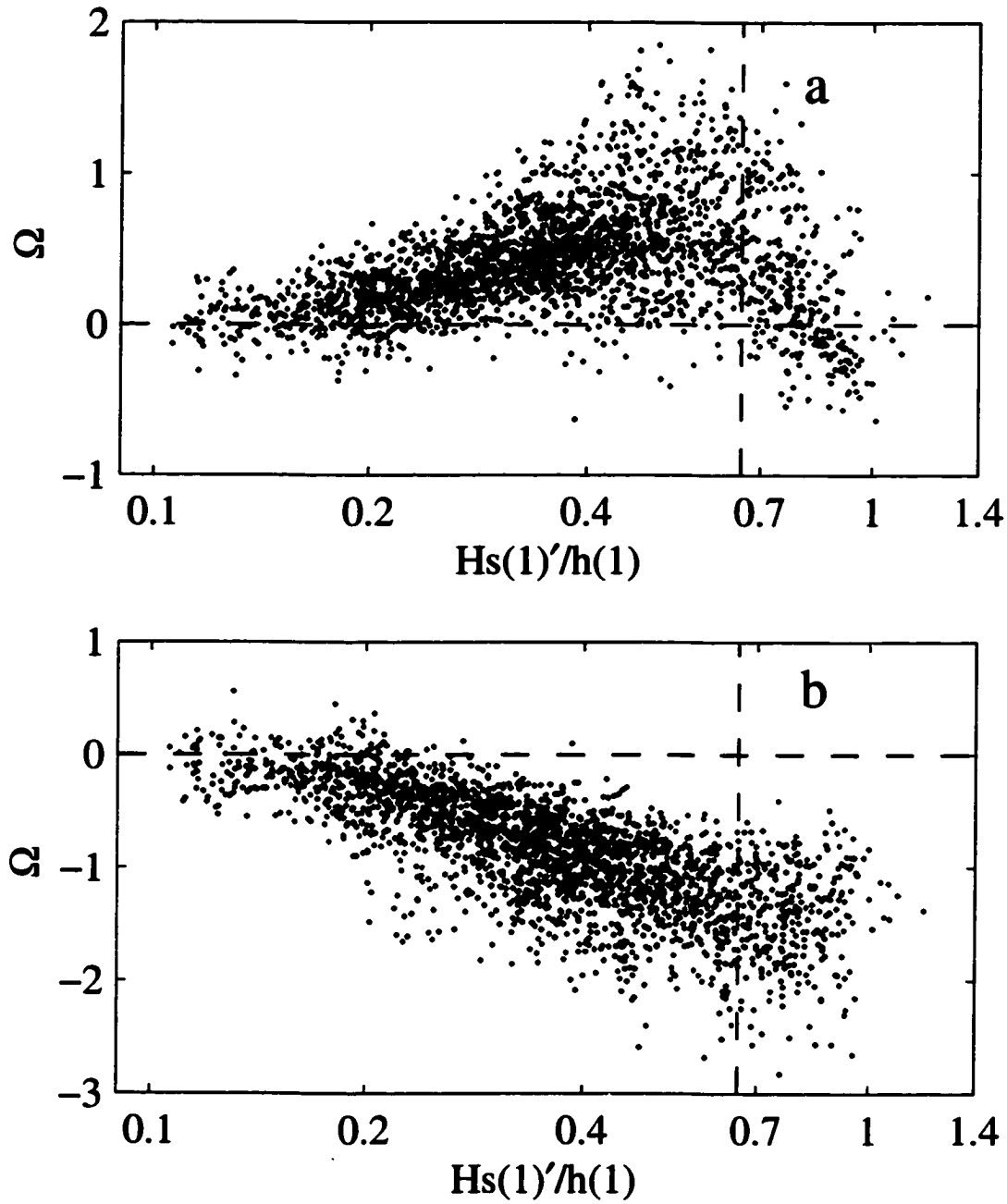

Figure 2.7: Estimated net forcing strength, Ω, defined by eq. (2.41) *versus* shoaled significant wave height (eq. (2.32)) divided by water depth, Hs'/h, at frame 1. a: Net forcing strength between frames 1 and 4. b: Net forcing strength onshore of frame 1. The vertical dashed lines indicate $Hs(1)'/h(1) = \gamma$. Each data point is estimated from a half-hour time series segment.

Ω values were scattered around zero. When incident waves were large, Ω was order-one, so forcing and dissipation were strong. Between frames 1 and 4 (between about 2 m and 3.5 m depth), net forcing increased with increasing wave height until it reached a maximum value when frame 1 was slightly outside the saturated surf zone. When frame 1 was inside the saturated surf zone, dissipation sometimes exceeded forcing between frames 1 and 4. Onshore of frame 1, dissipation usually exceeded forcing and net dissipation grew stronger as incident the wave height increased. I suggest that, when incident waves were large, dissipation was strong inside the surf zone and forcing was strong just outside the surf zone.

From equations (1.1) & (2.41) it is clear that $|\Omega|$ is related to $2\pi/Q$, but there are important differences between Ω and Q: Q measures the dissipation of a single wave (mode of motion), whereas Ω measures the net forcing or dissipation of all modes in some limited region. Consequently, the measured Ω values can not be used to estimate Q values for individual surf beat modes. Nevertheless, the negative, order-one Ω values observed during storms do indicate that the surf beat energy lost within the surf zone in a single beat period was of the same order as the total surf beat energy stored within the surf zone.

2.5 Discussion and conclusions

A simple energy balance equation relates the energy flux carried by progressive surf beat to net surf beat forcing or dissipation. I used water pressures, velocities, and depths measured on a beach near Duck, North Carolina, to estimate cross-shore surf beat energy fluxes, and applied the energy balance equation to estimate net surf beat forcing or dissipation. During the Sandyduck experiment, the nearshore zone (< 3.5 m depth) was usually a region of net surf beat dissipation. Surf beat carried energy into the nearshore zone to balance this net dissipation. The net shoreward surf beat energy flux was large during storms (about half as large as the energy flux that could be carried if all surf beat propagated directly onshore).

The strong shoreward energy fluxes reported here are consistent with the incomplete reflection of surf beat observed in the the surf zone by Nelson and Gonsalves (1992), Raubenheimer *et al.* (1995), Saulter *et al.* (1997), Henderson *et al.* (2001), and Sheremet *et al.* (2001).

Most existing surf beat models do not predict strong shoreward propagation because they do not simulate strong surf-zone dissipation. Unforced, undamped surf beat models (Eckart, 1951; Ursell, 1952; Kenyon, 1970; Holman and Bowen, 1979, 1982; Howd *et al.*, 1992; Bryan and Bowen, 1996) predict that surf beat is cross-shore standing. Non-dissipative and weakly-dissipative models that allow for the possibility of edge wave resonance (Gallagher, 1971; Bowen and Guza, 1978; Schäffer, 1994; Lippmann *et al.*, 1997) also predict that surf beat is cross-shore standing. The breakpoint-forcing model of Symonds *et al.* (1982) predicts cross-shore standing waves onshore of the breakpoint, and seaward propagating waves offshore of the breakpoint. The models of Schäffer (1993) and Van Dongeren *et al.* (1996) predict that nonlinear forcing due to intermittent wave breaking opposes incident bound-wave motions, leading to net nonlinear damping of surf beat at the breakpoint, and shoreward propagation just outside the breakpoint. However, these last three models exclude the possibility of edge wave resonance through the arbitrary assumption that forcing is entirely shore-normal.

During the Sandyduck experiment, dissipation was strongest well inside the saturated surf zone, exactly where incident waves were limited by breaking and surf beat made an important contribution to the total flow field. Models of surf beat dynamics should incorporate rapid surf-zone dissipation.

A standard bottom dissipation parameterisation predicted the observed net surf beat dissipation well. The wave dissipation factor for surf beat was $O(10^{-1})$, within the range of dissipation factors usually observed for higher frequency incident waves. However, the magnitude of nonlinear working on surf beat was correlated with the predicted frictional dissipation, so the correlation between net dissipation and predicted frictional damping might not indicate a causal relationship.

The region between 2 m and 3.5 m depth was a region of net surf beat forcing, except

when incident waves were very large and the saturated surf zone extended beyond 2 m depth. I suggest that surf beat forcing usually exceeded dissipation outside the surf zone, whereas dissipation exceeded forcing inside the surf zone. This is consistent with the cross-shore structure of surf beat forcing predicted by Longuet-Higgins and Stewart (1962) and Symonds *et al.* (1982), and with the suggestion of Guza and Bowen (1976b) and others that surf beat dissipation might be most rapid inside the surf zone.

Surf beat forcing and dissipation were very strong during storms. When incident waves were large, the surf beat energy dissipated within the surf zone during a single beat period was of the same order as the total surf beat energy stored within the surf zone. The surf beat energy forced in a single beat period near the edge of the surf zone was also of the same order as the total surf beat energy stored near the edge of the surf zone.

Chapter 3

The cross-shore structure of surf beat

3.1 Introduction

In Chapter 2, long time series of water pressure and velocity, measured at just four locations on a natural beach, were used to show that surf beat is dissipated rapidly in the surf zone. This chapter presents further observations from a different field experiment. Only a few short time series are analysed, but a very dense cross-shore array of 15 instrumented frames allows better resolution of the cross-shore structure of surf beat. The field site and instrumentation are described in Section 3.2. Section 3.3 shows that spatially-coherent surf beat was partly cross-shore standing, and partly cross-shore (usually shoreward) progressive. Section 3.4 presents estimates of the cross-shore energy flux carried by progressive surf beat. Results are summarised in Section 3.5. Related results were presented by Henderson *et al.* (2001).

3.2 Field site and instrumentation

Data were collected on an ocean beach near Duck, North Carolina, during the Duck94 experiment at the U.S. Army Field Research Facility (Gallagher *et al.*, 1998; Elgar *et al.*, 1997). Near-bottom water pressure and horizontal velocity were measured (at 2 Hz) at 16 locations along a cross-shore transect extending from the shore to about 8 m water depth

(fig.3.1). Seabed elevations were determined with surveys from an amphibious vehicle (Lee and Birkemeier, 1993) and sonar altimeters (Gallagher *et al.*, 1996) co-located with the pressure and current sensors.

3.3 Spatially-coherent surf beat

3.3.1 Methods

At each instrument location, 3-hr time series of bottom pressure were broken into ninety 50% overlapping segments, with

$$p_{j,k}(t) = j\text{'th time series of bottom pressure (in m water) at location } k.$$

Each time series segment was Hanning windowed and Fourier transformed. Let

$$\langle p_{j,k} \rangle'_\omega = \text{Fourier component of windowed } p_{j,k} \text{ at frequency } \omega,$$

$$\langle \boldsymbol{p}_j \rangle'_\omega = \begin{pmatrix} \langle p_{j,1} \rangle'_\omega \\ \langle p_{j,2} \rangle'_\omega \\ \vdots \\ \langle p_{j,14} \rangle'_\omega \end{pmatrix},$$

so that the vector $\langle \boldsymbol{p}_j \rangle'_\omega$ represents the cross-shore structure of pressure fluctuations at frequency ω. Pressure fluctuations measured at the most offshore location (7.5 m depth, fig.3.1) were not included in $\langle \boldsymbol{p}_j \rangle'_\omega$.

A cross-spectral matrix Φ was estimated at every frequency ω,

$$\Phi_\omega(\boldsymbol{p}, \boldsymbol{p}) = \overline{\langle \boldsymbol{p}_j \rangle'_\omega \, \langle \boldsymbol{p}_j^T \rangle'_{-\omega}},$$

where the overbar denotes an average over all realizations (i.e. all values of j), and T denotes a transpose. At each frequency, the eigenvectors of $\Phi_\omega(\boldsymbol{p}, \boldsymbol{p})$ are the frequency-domain Empirical Orthogonal Functions (EOF's), or principal components, of the pressure fluctuations. There are as many EOF's as there are elements of $\langle \boldsymbol{p}_j \rangle'_\omega$, but here only the

dominant EOF is considered (i.e. the eigenvector of $\Phi_\omega(\boldsymbol{p},\boldsymbol{p})$ associated with the largest eigenvalue). Johnson and Wichern (1982) show that the dominant EOF is the vector $\boldsymbol{\vartheta}(\omega)$ that minimises the mean square error $\overline{|\boldsymbol{\epsilon}_j(\omega)|^2}$ in

$$\langle \boldsymbol{p}_j \rangle'_\omega = a_j \boldsymbol{\vartheta}(\omega) + \boldsymbol{\epsilon}_j(\omega),$$

where the amplitudes a_j are chosen to obtain the best fit. In this sense, the dominant EOF is the single cross-shore structure that best fits the observed cross-shore structure of pressure fluctuations at frequency ω. In the cases presented the dominant EOF accounted for between 45% and 70% of the variance summed over all instruments.

If $\boldsymbol{\vartheta}(\omega)$ is a dominant EOF, then so is $\kappa\,\boldsymbol{\vartheta}(\omega)$ for any constant κ. The EOF's are normalised so that the component representing the pressure fluctuation closest to the shore equals 1 m.

The combined pressure *and* cross-shore velocity EOF's also were estimated as the dominant eigenvectors of the cross-spectral matrix

$$\Phi_\omega(\boldsymbol{\varsigma},\boldsymbol{\varsigma}) = \overline{\langle \boldsymbol{\varsigma}_j \rangle'_\omega \, \langle \boldsymbol{\varsigma}_j^T \rangle'_{-\omega'}},$$

where

$$\langle \boldsymbol{\varsigma}_j \rangle'_\omega = \begin{pmatrix} g^{1/2}\,\langle p_{j,1}\rangle'_\omega \\ g^{1/2}\,\langle p_{j,2}\rangle'_\omega \\ \vdots \\ g^{1/2}\,\langle p_{j,14}\rangle'_\omega \\ h^{1/2}\,\langle u_{j,1}\rangle'_\omega \\ h^{1/2}\,\langle u_{j,2}\rangle'_\omega \\ \vdots \\ h^{1/2}\,\langle u_{j,14}\rangle'_\omega \end{pmatrix},$$

$\langle u_{j,k} \rangle'_\omega$ =Fourier component of windowed $u_{j,k}$ at frequency ω,

$u_{j,k}(t)$ =j'th time series of shoreward water velocity at frame k,

g =gravitational acceleration,

h =water depth.

At every frequency a dominant EOF of was estimated from $\Phi_\omega(\varsigma,\varsigma)$. This single dominant EOF represented the cross-shore structure of both pressure and velocity.

Note the energy-based weighting of $\langle p\rangle'_\omega$ and $\langle u\rangle'_\omega$. For linear shallow water waves,

$$|g^{1/2}\ \langle p\rangle'_\omega\ |^2 = \text{potential energy density at frequency } \omega, \tag{3.1}$$

$$|h^{1/2}\ \langle u\rangle'_\omega\ |^2 = \text{kinetic energy density at frequency } \omega. \tag{3.2}$$

Finally, the pressure components of the dominant EOF of $\Phi_\omega(\varsigma,\varsigma)$ were divided by $g^{1/2}$ and the velocity components were divided by $h^{1/2}$ to convert back to units of pressure (m) and velocity (ms^{-1}).

3.3.2 Results and discussion

Figure 3.2a–c shows the dominant EOF's of low frequency (0.022 Hz) pressure fluctuations for two different 3 hr pressure time series. Both EOF's have clear amplitude maxima (at the shore and $x \approx 230$ m) and minima (at $x \approx 160$ and $x \approx 300$ m), with a phase jump of $\pm\pi$ at each minimum, consistent with the presence of a cross-shore standing wave. Here. unlike in Chapter 2, x is positive seawards. Monotonic changes of phase with distance from the shore, which would indicate the presence of a cross-shore progressive wave, were not observed.

The EOF's shown in fig.3.2a–c are typical of those observed at frequencies less than about 0.025 Hz. However at surf beat frequencies above about 0.03 Hz, the EOF's had a different cross-shore structure, as shown in fig. 3.2d–f ($\omega = 0.044$ Hz). Although the higher-frequency EOF had some nodal structure (fig.3.2e), the phase jumps obvious in the low frequency case have been replaced by a monotonic increase in phase with distance from the shore (fig.3.2f), indicating the presence of some shoreward-progressive surf beat. The sea level fluctuation associated with a given EOF $\boldsymbol{\theta}$ is proportional to $\Re[\boldsymbol{\theta}e^{i\omega t}]$. Figure 3.3 presents a sequence of 'snapshots' of $\Re[\boldsymbol{\theta}e^{i\omega t}]$ through the wave cycle for the 0.044 Hz EOF of September 22nd (fig. 3.2d–f).

Figure 3.4a–c shows a dominant EOF of combined pressure and velocity fluctuations

at $\omega = 0.022$ Hz. Note that in fig.3.4b,c a single 28-element EOF, with 14 pressure components and 14 velocity components, is plotted as two curves, with one curve representing the cross-shore structure of pressure EOF components and the other representing the cross-shore structure of velocity EOF components. Also note that, although the absolute magnitude of the EOF is arbitrary, the relative magnitudes of the pressure and velocity components are not arbitrary. For example, if the EOF plotted in fig.3.4a–c had generated a pressure fluctuation of 1 m at the most onshore instrument location, the associated co-located velocity fluctuation would have been about 2 ms^{-1} (fig.3.4b).

The pressure component of the dominant EOF of combined pressure and velocity fluctuations (circles, fig.3.4b,c) is similar to the EOF of pressure fluctuations alone (circles, fig.3.2b,c). Contributions to both pressure and velocity fluctuations show nodes, antinodes, and $\pm\pi$ phase jumps. Offshore of $x \approx 200$ m the nodes of pressure fluctuations coincided with the antinodes of velocity fluctuations, and *vice-versa*. Onshore of $x \approx 390$ m pressures were about $\pm\pi/2$ out of phase with co-located velocities. All of these features are predicted by cross-shore standing wave theories.

The dominant EOF of combined water pressure and velocity fluctuations at 0.044 Hz displays a mixture of progressive and standing wave behaviours (fig.3.4d–f). Some nodal structure is present, but there is a monotonic increase in phase with distance from the shore, indicating net shoreward propagation. With the exception of the most offshore location, the magnitude of the phase between pressure and velocity was between the $\pm\pi/2$ phase of standing waves and the zero phase of shoreward progressive waves.

Since the dominant EOF does not account for all of the observed variance, the results of the section are not conclusive. Nevertheless, it is encouraging that the cross-shore structure of surf beat revealed by EOF analysis is consistent with the observations of shoreward energy fluxes reported in Chapter 2, and in Section 3.4.

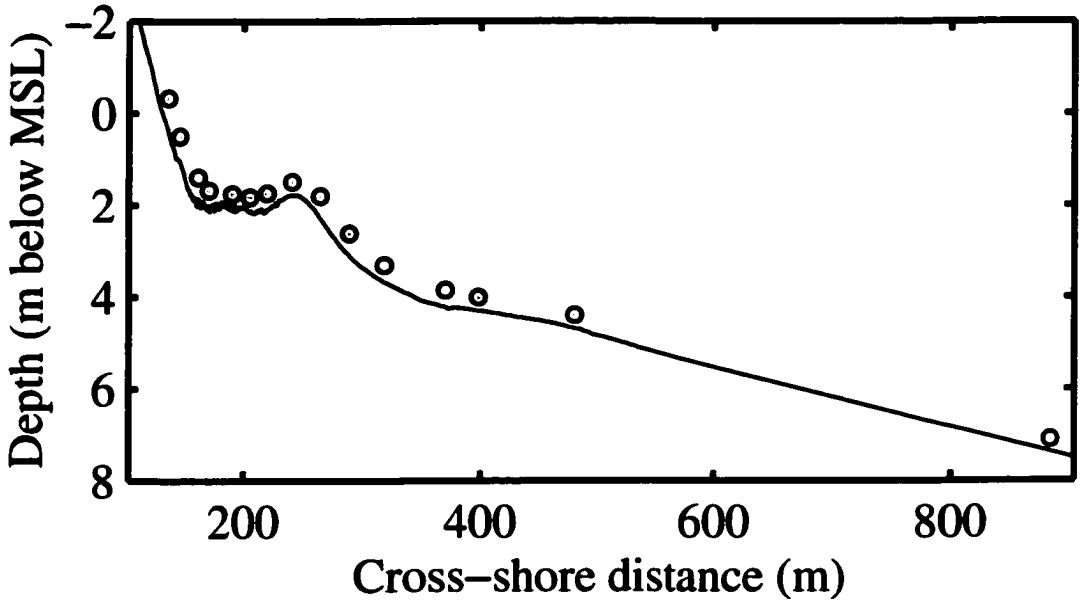

Figure 3.1: Beach profile measured on Sept. 20th (solid curve) and the location of co-located pressure gauges and current meters (circles). The zero of the x-axis is arbitrary.

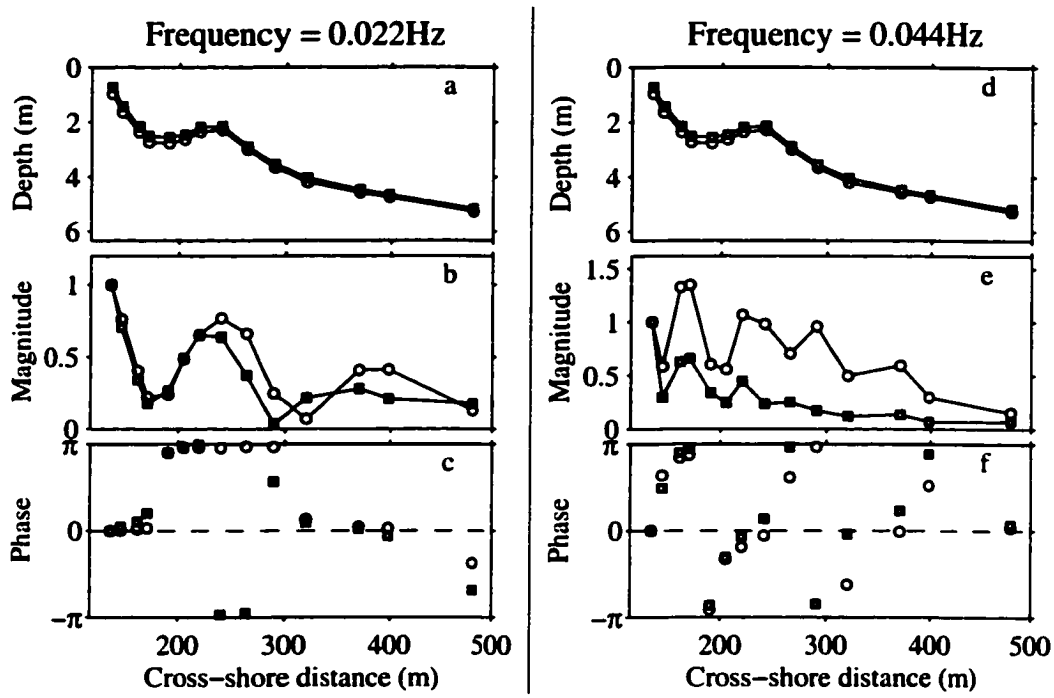

Figure 3.2: Water depth (a,d), and the amplitude in m (b,e) and phase (c,f) of dominant EOF's of pressure *versus* cross-shore distance (relative to same datum as fig.3.1). Left panels: frequency = 0.022 Hz. Right panels: frequency = 0.044 Hz. Squares: September 28th, significant wave height 0.4 m. Circles: September 22nd, significant wave height 2.7 m.

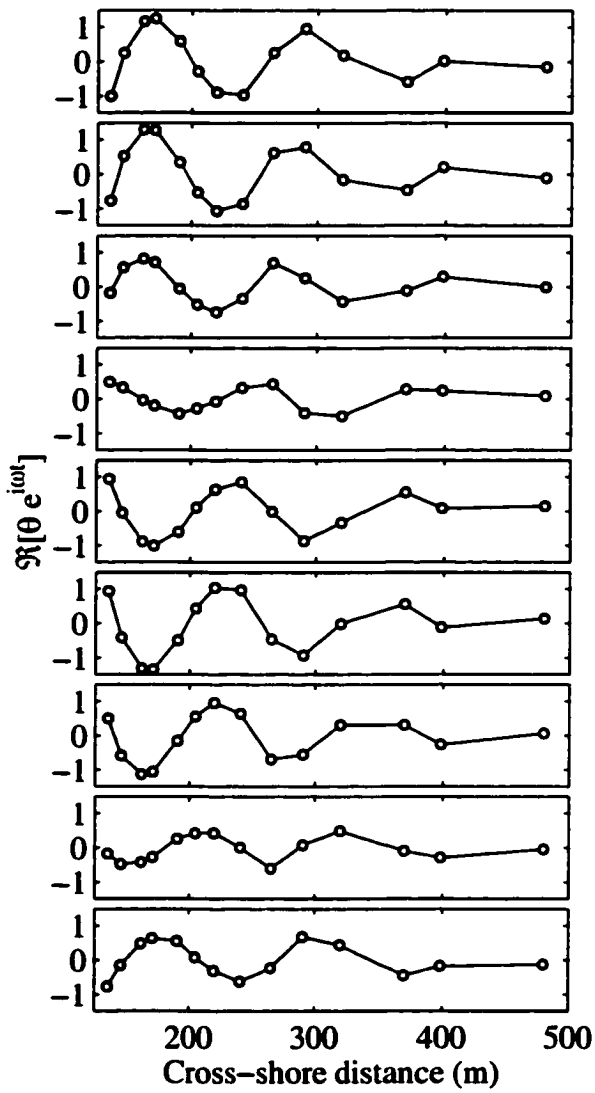

Figure 3.3: Sea level fluctuation due to 0.044 Hz EOF of September 22nd θ *versus* cross-shore distance. j'th panel from top represents the sea level j ninths of the way through a wave cycle, i.e. $\Re[\theta e^{i\omega t_j}]$, where $\omega = (2\pi)0.044$ Hz, and $t_j = (2\pi/\omega)(j/9)$.

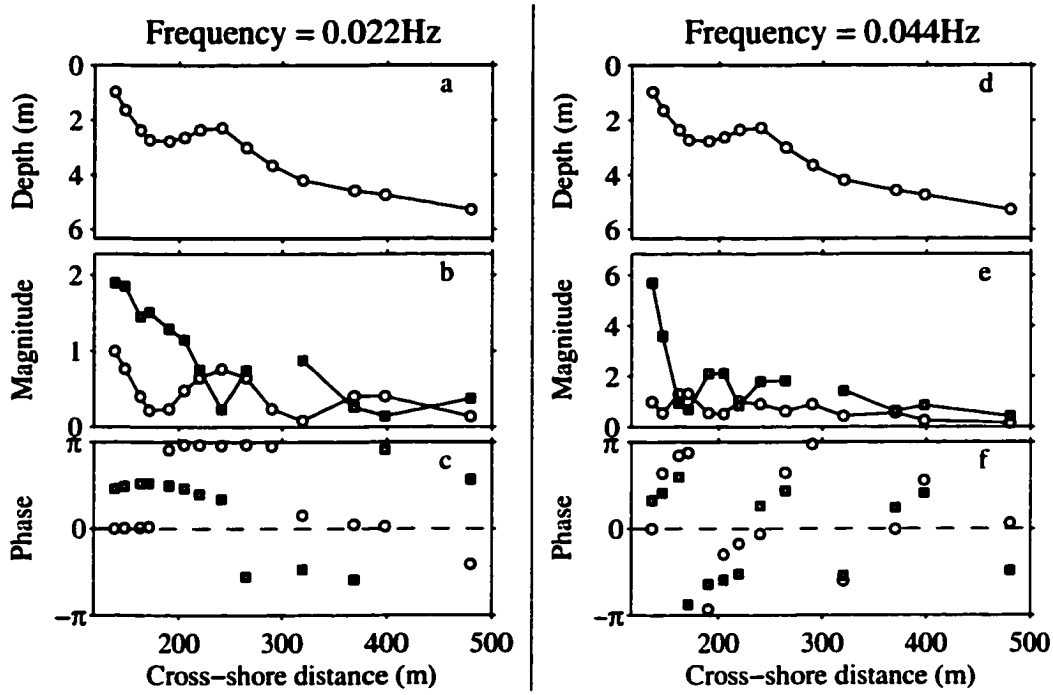

Figure 3.4: Water depth (a,d), and the amplitude (b,e) and phase (c,f) of the dominant EOF of combined water pressure and velocity on September 22nd *versus* cross-shore distance (relative to same datum as fig.3.1). Left panels: frequency = 0.022 Hz. Right panels: frequency = 0.044 Hz. Circles: pressure (m). Squares: cross-shore velocity (ms^{-1}).

3.4 Energy transport

This Section presents observations of wave energy density and energy flux. I consider three frequency bands: Low frequency surf beat (0.005–0.025 Hz), high frequency surf beat (0.025–0.05 Hz), and sea/ swell (0.05–0.3 Hz). Since sea and swell are not always in shallow water, it is necessary to allow for depth-dependence of the water pressure and velocity fields. I assumed that the depth-dependence of the pressure and velocity is given by linear theory (Mei, 1983). The energy flux was then estimated as the depth-integrated product of pressure and velocity (depth dependence was allowed for, but had very little effect, at infragravity frequencies). I neglected vertical variations in pressure and velocity associated with wave breaking. Consequently, the estimates of incident wave energy density and flux presented in this section might not be accurate inside the surf zone. In contrast, estimates of surf beat energy densities and fluxes are probably not affected greatly by vertical structure (Section 2.2.1 and Appendix A.1).

About 1000 three-hour time series were collected during the Duck94 experiment. Most were clearly non-stationary, and were excluded from the data set presented here. The remaining data set was reduced to just 13 three-hour time series by removing occasions when longshore currents were greater than 0.25 ms^{-1}, and occasions when the longshore surf beat energy flux was greater than half the cross-shore energy flux. The exclusion of cases where longshore currents were significant ensured that shear waves contributed little to the observed low frequency motions. Cases where the longshore surf beat energy flux was strong were removed to minimise the effects of longshore non-uniformity on the surf beat energy balance. This section presents results from three typical three-hour times series. Results from the remaining 10 time series are presented in Appendix C.

The estimated shoreward energy flux carried by small incident waves (Sept. 17th, $Hs =$ 0.4 m) was almost constant seaward of about $x = 250$ m, indicating that very little energy was dissipated as incident waves shoaled from about 8 m to 2.5 m depth (fig. 3.5d). The incident wave energy flux decreased on the shoreface ($x < 160$ m), indicating dissipation. For incident waves, the progressiveness parameter ρ was slightly less than one (fig. 3.5g), indicating that reflection of incident waves was weak, but measurable (consistent with Elgar

et al. (1997)).

Seaward of $x \approx 300$ m, the surf beat energy fluxes and ρ values were almost constant and near zero, indicating that surf beat was nearly cross-shore standing (fig. 3.5e,f,g). Between $x = 200$ m and $x = 300$ m, the estimated shoreward surf beat energy flux increased, indicating that surf beat energy was generated in this region. Shoreward of $x = 200$ m, the energy flux carried by high frequency surf beat increased slightly, whereas the energy flux carried by low frequency surf beat seemed to decrease just shoreward of $x = 200$ m, before again increasing shoreward of $x = 170$ m. Shoreward of about $x = 250$ m, ρ was slightly greater than zero, indicating that surf beat was nearly cross-shore standing, but there was some weak net shoreward propagation.

The estimated shoreward energy flux carried by moderately energetic incident waves (Sept. 26th, $Hs = 0.96$ m) decreased from about 3.8 m^4s^{-3} at $x \approx 350$ m to about 1.8 m^4s^{-3} at $x \approx 200$ m, presumably due to wave-breaking dissipation on the seaward face of the bar (fig. 3.6d). For incident waves, the progressiveness parameter ρ was about one seaward of the bar crest, but dropped slightly below one at about $x = 200$ m and $x = 150$ m (fig. 3.6g), perhaps due to weak reflection, or the increase in directional spread that accompanies breaking (Herbers *et al.*, 1999).

Seaward of $x \approx 500$ m, surf beat energy fluxes and ρ values were slightly less than zero, indicating that surf beat was nearly cross-shore standing, but there was some weak net seaward propagation (fig. 3.6e,f,g). Between $x = 250$ m and $x = 500$ m, the estimated shoreward surf beat energy flux increased, indicating net surf beat generation. Shoreward of $x = 250$ m, the energy flux carried by high frequency surf beat decreased slightly, whereas the energy flux carried by low frequency surf beat decreased greatly, indicating net surf beat dissipation. ρ values were greater than zero but less than 0.5 over the bar crest, indicating mixed standing and shoreward-propagating waves. Shoreward of about $x = 170$ m, ρ values for high frequency surf beat were near 0.5, indicating strong net shoreward propagation. In contrast, ρ values for low frequency surf beat were almost zero in this region, indicating that these waves were almost cross-shore standing.

The energy density and energy flux of energetic incident waves (Oct. 16th, $Hs =$

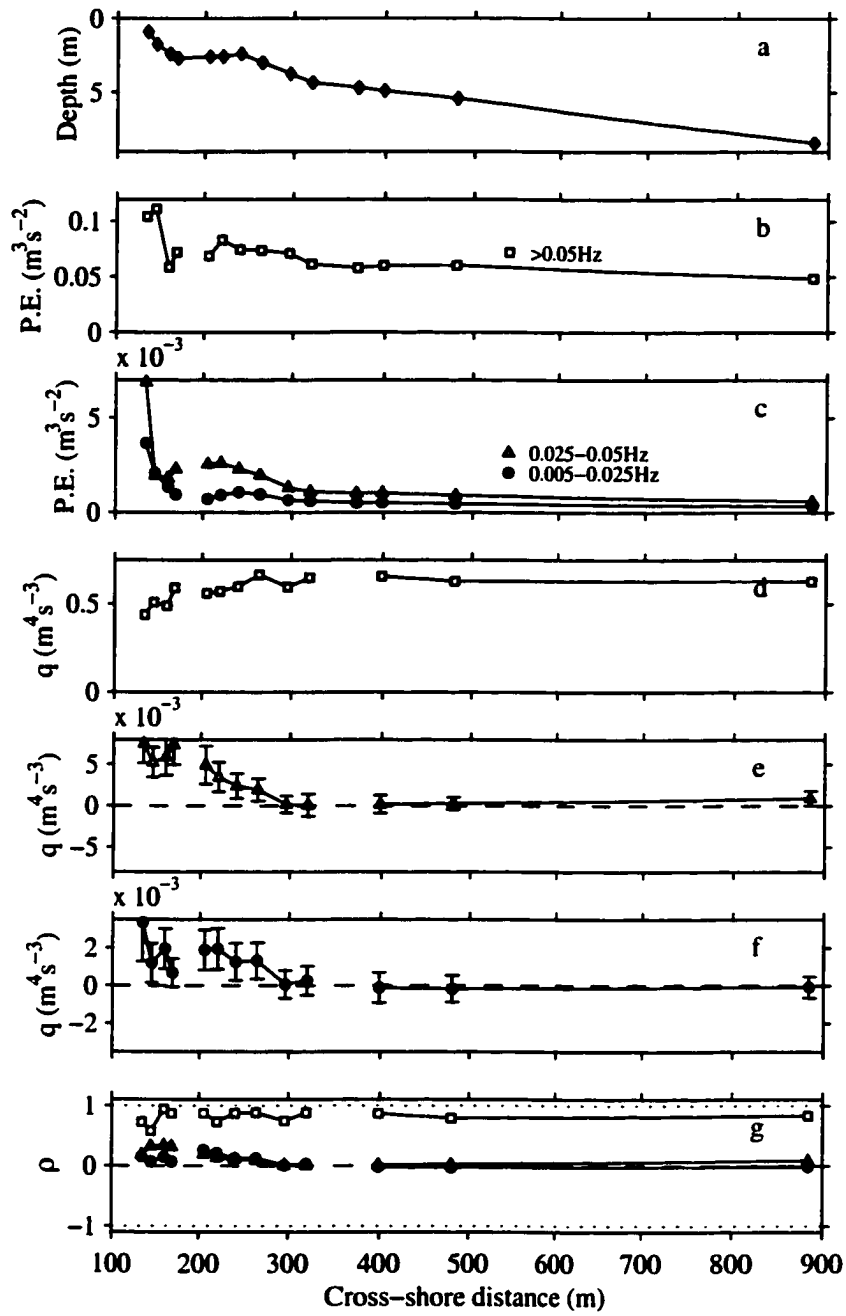

Figure 3.5: Water depth (a), potential energy density $P.E.$ (b: swell. c: surf beat), shoreward energy flux q (d: swell. e: high frequency surf beat. f: low frequency surf beat), and progressiveness parameter ρ (g) *versus* cross-shore distance. Values estimated from 3 hr time series on September 17th, $Hs = 0.4$ m. Squares: Swell (> 0.05 Hz). Triangles: High frequency surf beat (0.025–0.05 Hz). Circles: Low frequency surf beat (0.005–0.025 Hz).

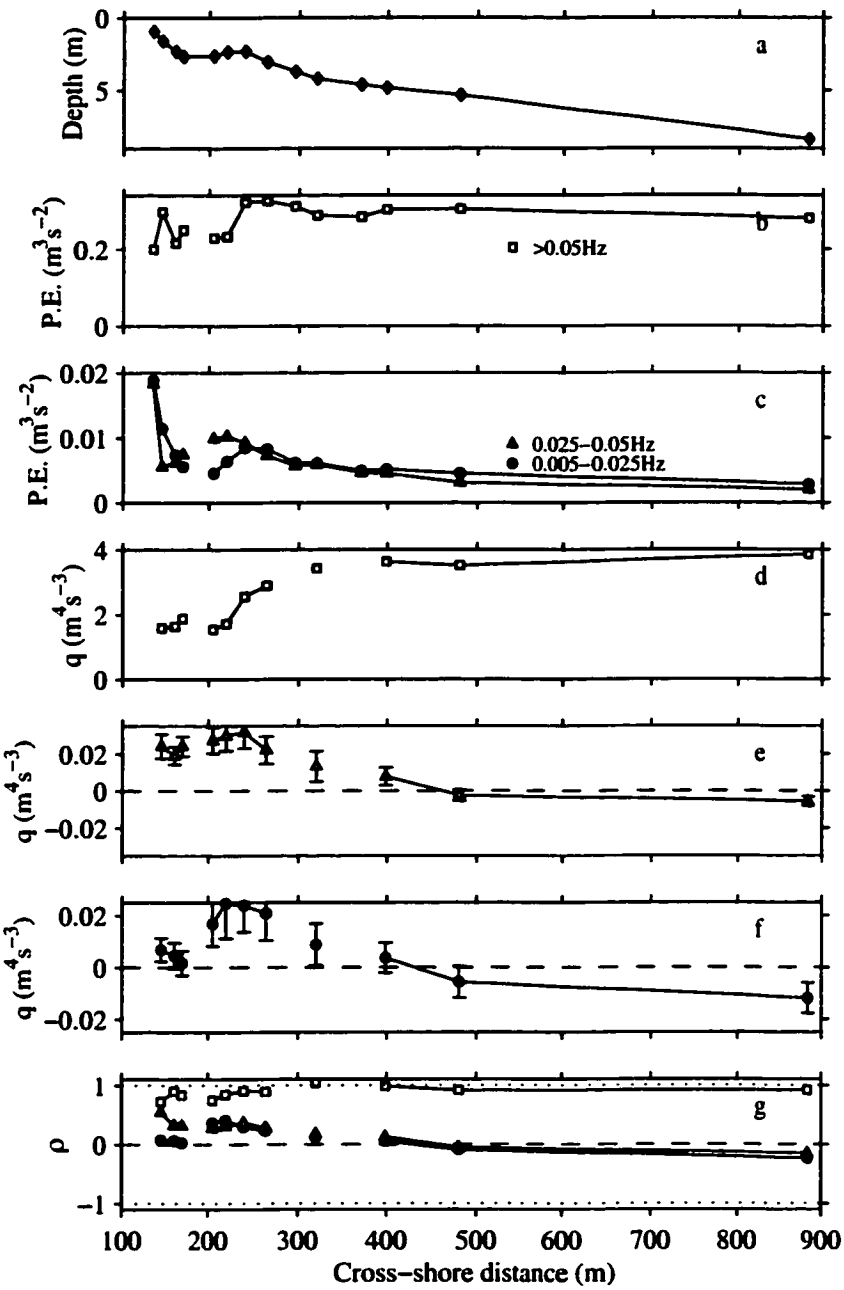

Figure 3.6: Water depth (a), potential energy density $P.E.$ (b: swell. c: surf beat), shoreward energy flux q (d: swell. e: high frequency surf beat. f: low frequency surf beat), and progressiveness parameter ρ (g) *versus* cross-shore distance. Values estimated from 3 hr time series on September 26th, $Hs = 0.96$ m. Squares: Swell (> 0.05 Hz). Triangles: High frequency surf beat (0.025–0.05 Hz). Circles: Low frequency surf beat (0.005–0.025 Hz).

2.3 m) decreased shoreward of about $x = 500$ m (fig. 3.7b,d), suggesting that the surf zone extended from the shore to at least 6 m water depth (the surf zone might have extended further seaward but we can not be sure, because the current meters in 8 m depth did not provide reliable data on this day). Seaward of the bar (about $x = 270$ m), estimated ρ values for incident waves were very close to 1 (fig. 3.7g). Over the bar, ρ values for incident waves dropped as low as 0.7, perhaps due to increased directional spread of incident waves over the bar crest (Herbers *et al.* (1999)). Interestingly, ρ values increase again, to about 1, shoreward of the bar.

The estimated surf beat energy flux was directed shorewards ($q > 0$, fig. 3.7e,f) across the entire array, indicating that the nearshore was a net sink of surf beat energy. The surf beat energy flux decreased on the offshore face of the bar (between $x = 270$ m and $x = 400$ m), suggesting that surf beat was dissipated there. Surf beat ρ values were greater than zero and sometimes exceeded 0.5 (fig. 3.7g), indicating net shoreward progressiveness. The ρ values of relatively high frequency surf beat were greater than ρ values of low frequency surf beat, indicating that high frequency surf beat was more shoreward-progressive than low frequency surf beat.

In the three cases discussed above, and in the remaining 10 cases presented in Appendix C, surf beat carried energy into the very shallow region onshore of the most shoreward instrument frame. The mechanism responsible for dissipating the surf beat energy brought into this region is not known. Bottom friction, wave breaking, and nonlinear wave interactions probably play a role, but the relative importance of these processes can not be determined from these measurements.

Observed marked decreases in the incident wave energy flux, which indicate intense wave breaking, were usually accompanied by marked decreases in the energy flux carried by low frequency surf beat. A simultaneous, but weaker, reduction in the energy flux carried by high frequency surf beat was also often observed. The mechanism responsible for the rapid loss of surf beat energy in the outer surf zone is not known. Bottom friction could play a role. Section 4.3.4 outlines another possible mechanism for destruction of shoreward-propagating infragravity waves in the outer surf zone.

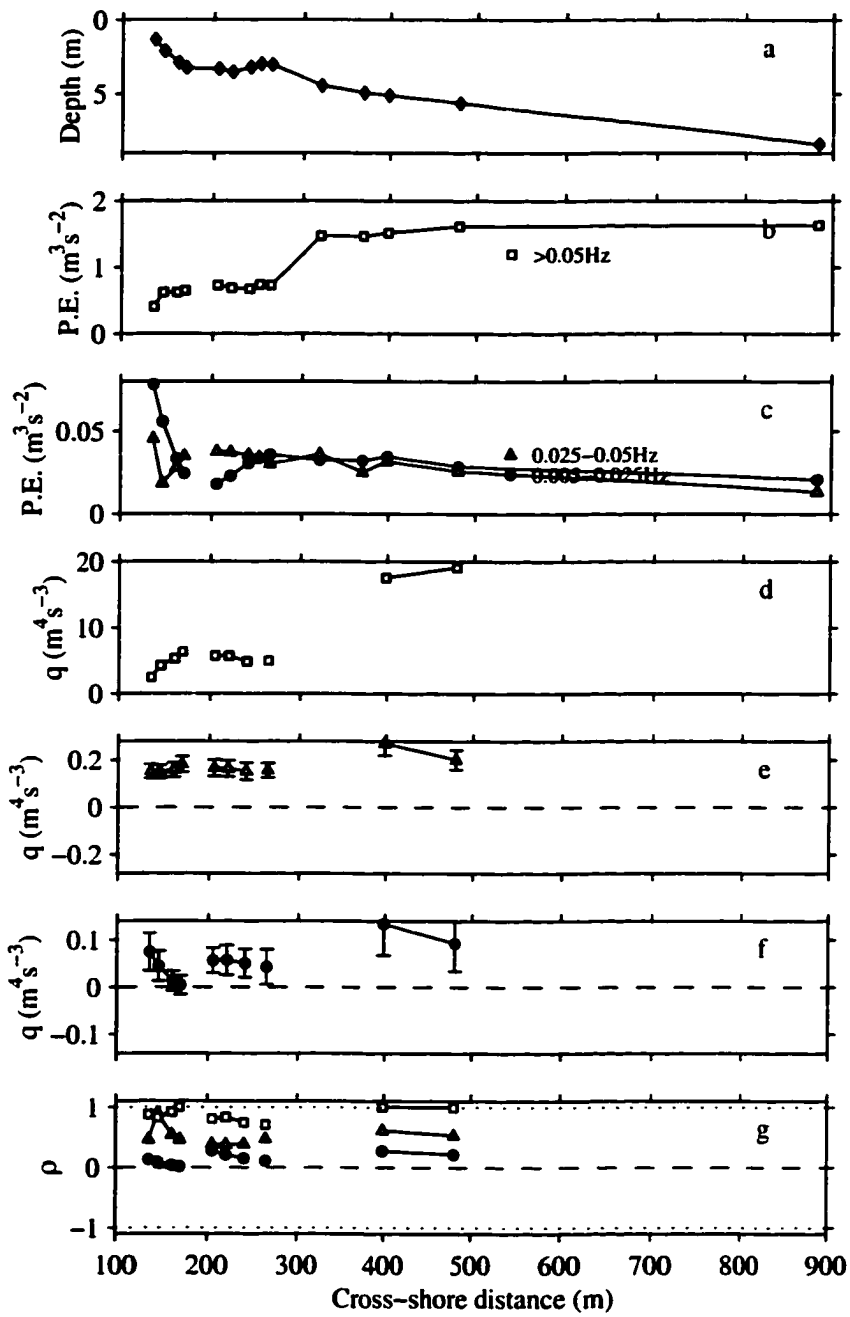

Figure 3.7: Water depth (a), potential energy density $P.E.$ (b: swell. c: surf beat), shoreward energy flux q (d: swell. e: high frequency surf beat. f: low frequency surf beat), and progressiveness parameter ρ (g) *versus* cross-shore distance. Values estimated from 3 hr time series on October 16th, $Hs = 2.3$ m. Squares: Swell (> 0.05 Hz). Triangles: High frequency surf beat (0.025–0.05 Hz). Circles: Low frequency surf beat (0.005–0.025 Hz).

3.5 Summary

Frequency-domain EOF's based on observations of near-bottom pressure and velocity along a cross-shore transect between the shore and 8 m water depth on a barred beach were used to identify the dominant spatially coherent components of surf beat. The dominant EOF's at relatively low beat frequencies (0.005–0.025 Hz) were consistent with standing wave theories. In contrast, the dominant EOF's at relatively high beat frequencies (0.03–0.05 Hz) displayed a mixture of progressive and standing wave behaviours. The net shoreward energy flux carried by propagating surf beat was sometimes as large as half the energy flux that could have been carried if all surf beat propagated directly shorewards, consistent with partially progressive waves.

Surf beat carried energy towards the shore, where it was lost in water less than about 1 m deep. The cross-shore surf beat energy flux also converged in the outer surf zone, suggesting strong surf beat dissipation there. The mechanism responsible for dissipating surf beat is not known, but bottom friction, wave breaking, and nonlinear wave interactions might play a role. The loss of infragravity energy in the outer surf zone is discussed further in Chapter 4.

Chapter 4

Simulations of dissipative surf beat

4.1 Introduction

So far, this thesis has been devoted to presenting field evidence of strong shoreward surf beat propagation, and an associated rapid loss of surf beat energy in the surf zone. After finishing the analysis on which Chapter 2 is based, I visited Alex Sheremet and Bob Guza at the Scripps Institution of Oceanography. I discovered that they had (independently and simultaneously) also found strong shoreward surf beat propagation. They discovered that they could not adequately fit pressure and velocity fluctuations measured by an extensive array of 35 instrumented frames with just a set of cross-shore standing waves — energetic shoreward-progressive waves were required (Sheremet *et al.*, 2001). They also found that most shoreward-progressive waves propagated at an oblique angle to the shore. Consequently, shoreward-propagating waves had the short longshore wavelengths that are characteristic of edge waves.

Previously-published edge wave models assume that dissipation is weak, and therefore predict that surf beat is cross-shore standing (Sections 1.3 and 2.5). Leaky wave models do predict cross-shore propagation, regardless of the strength of dissipation (Sections 1.3 and 2.5), but the shore-oblique propagation observed by Alex Sheremet and co-workers strongly suggests that the observed shoreward-propagating waves were not predominantly leaky waves.

This chapter presents a model of infragravity waves that includes dissipation at leading order. The model is introduced in Section 4.2. The model simulates only shore-oblique shallow water waves, and therefore can not simulate leaky waves. I discuss the possible importance of leaky waves in Sections 4.2, 4.3, & 4.5. Section 4.3 presents model results. As expected, dissipation introduces cross-shore propagating edge waves, which carry energy from regions of forcing to regions of dissipation. Perhaps more surprisingly, shore-oblique shallow water waves can be strongly modified by dissipation, even when dissipation is weak and $Q \gg 1$. In certain cases, including some high Q cases, evanescent waves can dominate over edge waves. Realistic forcing generates group-bound evanescent waves, which appear very similar to the group-bound waves described by Longuet-Higgins and Stewart (1962) and Hasselmann *et al.* (1963). However, group-bound evanescent waves are not released when wave groups are destroyed by breaking. Instead, incoming evanescent waves simply disappear when the reach the vicinity of the breakpoint. Weak dissipation ($Q \gg 1$) can also have a leading-order effect by decoupling bar- and shore-trapped edge waves. In Section 4.5 I summarise the effects of dissipation on simulated shore-oblique shallow water waves, and note several model predictions that could be tested using field data. Related results were presented by Henderson and Bowen (2001).

4.2 Model derivation

4.2.1 Governing equations

In this Section we derive a set of equations that governs the dynamics of forced, dissipative, shore-oblique shallow water waves.

Let

t = time,

x = distance from shore,

y = longshore position,

u = x component of Eulerian water velocity,

v = y component of Eulerian water velocity,

M_x = x component of Stokes drift,

M_y = y component of Stokes drift,

$\tilde{u} = u + M_x/h$,

$\tilde{v} = v + M_y/h$,

h = still water depth,

η = sea surface displacement,

g = gravitational acceleration.

Here, x is positive seawards, in contrast to Chapter 2. The definition of (M_x, M_y) as the Stokes drift conflicts with the definition of $\boldsymbol{M}$ used in Chapter 2 because the mean water depth differs from the still water depth. This error is small compared with other errors inherent in the model presented in this Chapter, and will be ignored. I have included the Stokes drift in the depth-averaged transport velocity $(\tilde{u}, \tilde{v})$ (c.f. Longuet-Higgins and Stewart (1962) and p.62 of Phillips (1977)).

The forced, dissipative shallow water equations are

$$\frac{\partial \tilde{u}}{\partial t} + g\frac{\partial \eta}{\partial x} + \lambda u = F_x, \tag{4.1}$$

$$\frac{\partial \tilde{v}}{\partial t} + g\frac{\partial \eta}{\partial y} + \lambda v = F_y, \tag{4.2}$$

$$\frac{\partial \eta}{\partial t} + \frac{\partial h\tilde{u}}{\partial x} + \frac{\partial h\tilde{v}}{\partial y} = 0, \tag{4.3}$$

where λ is a damping coefficient (here assumed constant). I have assumed that friction acts on the Eulerian flow, but not on the Stokes drift.

Let

$$h = \beta x, \tag{4.4}$$

where β is a constant beach slope.

I have assumed unrealistically simple forms for h and λ, but Appendix E shows how realistic conditions can be modeled by simply patching together solutions of eq.'s (4.1)–(4.4).

Assume solutions of the form $\eta = \hat{\eta}(x)e^{i(ky-\omega t)}$, and similarly for u, v, F_x, F_y, M_x, and M_y. Since we are interested in steady, longshore-homogeneous waves, I assume ω and k are real. The Fourier components defined here are a function of the longshore wavenumber k, and are denoted with a hat ($\hat{}$), whereas the Fourier components of Chapters 2 and 3 were evaluated at a point, were not associated with a particular wavenumber, and were denoted by angle brackets($\langle\,\rangle$). Solving eq.'s (4.1)–(4.4) for $\hat{\eta}$ gives

$$\frac{\partial}{\partial x}\left(x\frac{\partial\hat{\eta}}{\partial x}\right) + \left[\frac{\omega^2}{g\beta}\left(1 + i\frac{\lambda}{\omega}\right) - k^2 x\right]\hat{\eta} = \hat{F}, \tag{4.5}$$

where the dimensionless forcing is

$$\hat{F} = \frac{1}{g\beta}\left[\frac{\partial}{\partial x}\left(\beta x\hat{F}_x + \lambda\hat{M}_x\right) + ik\left(\beta x\hat{F}_y + \lambda\hat{M}_y\right)\right]. \tag{4.6}$$

If $\lambda = 0$ and $\hat{F} = 0$ then eq. (4.5) reduces to the free edge wave equation (Mei, 1983, p.155).

Boundary conditions are

$$\lim_{x\to 0} x\frac{\partial\hat{\eta}}{\partial x} = 0, \tag{4.7}$$

and

$$\hat{\eta} \text{ is bounded as } x \to \infty. \tag{4.8}$$

Equations (4.5), (4.7) & (4.8) govern forced, dissipative, shore-oblique shallow water waves.

4.2.2 Forcing

The special case where $\hat{F}(x)$ is a Dirac delta-function (denoted by δ) will play an important role in the remainder of this Chapter. I refer to such forcing as 'point forcing', because it is

applied at a single cross-shore location, but recall that forcing is assumed to be sinusoidal alongshore.

Many different fields of applied force $\boldsymbol{F} = (F_x, F_y)$ can produce the same forcing $\hat{F}$ in the sea level equation (eq. 4.5). By choosing appropriate potentials P_1 and P_2, we can decompose the total force field into divergent and non-divergent parts:

$$\boldsymbol{F} = \frac{1}{h}[\nabla P_1 + \nabla \times (P_2 \boldsymbol{z})], \tag{4.9}$$

where $\boldsymbol{z}$ is a vertical unit vector. Only the divergent part of the forcing (∇P_1) appears in the sea level equation (eq. 4.5). Similarly, only the divergent part of the Stokes Drift appears in the sea level equation. However, non-divergent components of the applied force and Stokes Drift do appear the momentum equations.

Most results presented in this Chapter concern sea level fluctuations, not water velocity fluctuations. Consequently, we seldom need to specify the non-divergent forcing. However, non-divergent forcing will become important when we discuss the energy flux carried by edge waves. When discussing energy fluxes, I will avoid ambiguity by partitioning $\hat{F}$ as follows:

$$\hat{F} = \hat{F}_1 + \hat{F}_2, \tag{4.10}$$

$$\hat{F}_1 = \frac{\partial}{\partial x}\left(\frac{\beta x \hat{F}_x + \mathrm{i}\omega \hat{M}_x}{g\beta}\right), \tag{4.11}$$

$$\hat{F}_2 = \mathrm{i}k\left(\frac{\beta x \hat{F}_y + \lambda \hat{M}_y}{g\beta}\right) + \frac{\partial}{\partial x}\left[\frac{(\lambda - \mathrm{i}\omega)\hat{M}_x}{g\beta}\right]. \tag{4.12}$$

If $\hat{F} = \delta(x - x_F)$, then F_2 is associated with point forcing (at x_F) in the longshore momentum and mass conservation equations (eq. 4.2 & 4.3), whereas F_1 is associated with distributed forcing (seaward of x_F) in the cross-shore momentum equation (eq. 4.1).

If surf beat is forced by the radiation stress, S, then

$$F_x = -\frac{1}{\varrho h}\left(\frac{\partial S_{xx}}{\partial x} + \frac{\partial S_{xy}}{\partial y}\right), \tag{4.13}$$

$$F_y = -\frac{1}{\varrho h}\left(\frac{\partial S_{yy}}{\partial y} + \frac{\partial S_{xy}}{\partial x}\right), \tag{4.14}$$

and

$$\hat{F} = -\frac{1}{\varrho g\beta}\left(\frac{\partial^2 \hat{S}_{xx}}{\partial x^2} + 2ik\frac{\partial \hat{S}_{xy}}{\partial x} - k^2\hat{S}_{yy}\right) + \frac{\lambda}{g\beta}\left(\frac{\partial \hat{M}_x}{\partial x} + ik\hat{M}_y\right), \tag{4.15}$$

where ϱ = water density.

4.2.3 Solution

Two linearly-independent homogeneous solutions of eq. (4.5), f_A and f_B, are derived in Appendix D. f_B satisfies the shoreline boundary condition (eq. (4.7)), but not the seaward boundary condition (eq. (4.8)), whereas f_A satisfies the seaward boundary condition but not the shoreline boundary condition. Since no linear combination of f_A and f_B satisfies both boundary conditions, no steady homogeneous solution of eq.'s (4.5), (4.7) & (4.8) exists. This is not surprising, since no steady unforced wave field can exist in the presence of dissipation.

f_A and f_B can be used to construct forced solutions to eq.'s (4.5), (4.7) & (4.8). The dimensionless Green's function

$$G(x, x_F) = \begin{cases} Bf_B(kx) & x \leq x_F \\ Af_A(kx) & x > x_F \end{cases}, \tag{4.16}$$

where A and B are chosen to satisfy

$$\lim_{x \to x_F+} G(x, x_F) = \lim_{x \to x_F-} G(x, x_F), \tag{4.17}$$

and

$$\lim_{x \to x_F+} \frac{\partial G(x, x_F)}{\partial x} - \lim_{x \to x_F-} \frac{\partial G(x, x_F)}{\partial x} = \frac{1}{x_F}, \tag{4.18}$$

is the response at x to point forcing $\hat{F} = \delta(x - x_F)$, where δ is the Dirac delta function. Therefore, f_A represents the wave field seaward of the point of forcing, whereas f_B represents the wave field shoreward of the point of forcing.

The particular solution of eq.'s (4.5), (4.7) & (4.8) for arbitrary $\hat{F}(x)$ is (Arfken and Weber, 2001, p.618)

$$\hat{\eta}(x) = \int_{x_F} G(x, x_F)\hat{F}(x_F)\, dx_F. \tag{4.19}$$

Therefore, the response to forcing at one cross-shore location is described by a Green's function, and the response to distributed forcing given by an integral of Green's functions. The behaviour of the Green's functions is described in Sections 4.3.1–4.3.3, and the response to distributed forcing (by groups of incident breaking waves) is discussed in Section 4.3.4.

Appendix E shows how forced, dissipative shallow water waves can be simulated for complex profiles of water depth and dissipation strength by patching together the planar beach solutions discussed in this Section.

f_A and f_B are functions of the non-dimensional cross-shore distance

$$\chi = 2kx, \tag{4.20}$$

the dissipation strength λ/ω, and the mode number

$$n = \frac{1}{2}\left(\frac{\omega^2}{kg\beta} - 1\right). \tag{4.21}$$

Eckart (1951) showed that, in the absence of forcing and dissipation, edge waves exist on a planar beach only for integer values of the mode number n. In contrast, forced waves have the wavenumber and frequency of the applied forcing, and exist for non-integer values of n. I refer to n as the mode number, even when n takes non-integer values.

Figure 4.1 summarises the behaviour of f_A for n between -0.5 and 4.5. A vertical section through each plot gives the cross-shore structure of the wave field for a particular value of n. Figure 4.1a,b shows weakly-dissipative waves, and fig. 4.1c,d shows strongly-dissipative waves. Since f_A is a homogeneous solution, its amplitude is arbitrary. In fig.4.1a,c, f_A has been renormalised so that the mean square value of f_A shoreward of the edge wave turning point (where $(gh)^{1/2} = \omega/k$, dashed line in fig. 4.1) equals one. Recall that f_A represents the wave field seaward of regions of forcing. Waves propagating seawards, away from regions of forcing, are reflected from the turning point. Outside the turning point the magnitude of f_A decays almost exponentially. Waves reflected from the turning point interfere with outgoing waves, setting up a cross-shore standing pattern, with nodes and antinodes (light and dark bands in fig. 4.1a), and 180 degree phase jumps at the nodes (fig. 4.1b). The cross-shore standing structure, clear in the weakly-dissipative case

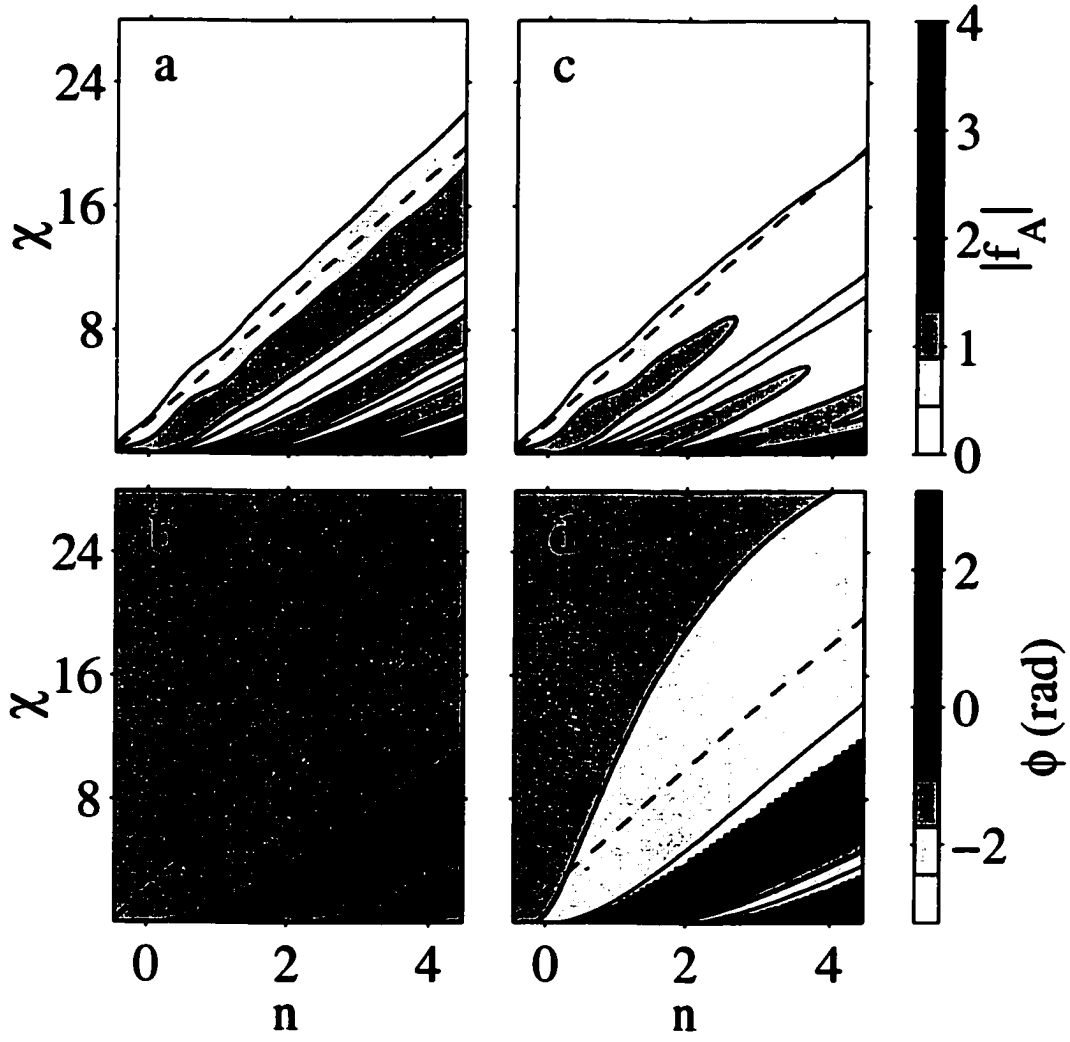

Figure 4.1: Dependence of homogeneous solution f_A on mode number n and distance from shore $\chi = 2kx$. Dashed line is edge wave turning point. a,c: magnitude $|f_a|$, b,d: phase ϕ, where $f_A = |f_A|e^{i\phi}$. a,b: $\lambda/\omega = 3 \times 10^{-3}$, c,d: $\lambda/\omega = 8 \times 10^{-2}$.

(fig. 4.1a,b), is modified by dissipation, as shown most clearly in the strongly-dissipative case (fig. 4.1c,d). Since energy is dissipated as waves propagate to the turning point and back, the nodal structure is incomplete (weakly-developed light and dark bands in fig. 4.1c) and net seaward propagation results (except for 2π wraps, the phase increases smoothly with distance from shore in fig. 4.1d).

Figure 4.2 summarises the behaviour of f_B. Inside the edge wave turning point, waves propagate shorewards, away from regions of forcing, and reflect from the shore, setting up a standing wave structure (fig. 4.2a,b). Dissipation leads to net shoreward propagation (fig. 4.2d), and weakened nodal structure (fig. 4.2c). For non-integer mode numbers, f_B grows almost exponentially with distance seaward of the turning point. For near-integer mode numbers, the exponential growth of f_B begins far seaward of the turning point. Note that all magnitudes greater than 4 are represented by black shading in fig. 4.2a,c. Consequently, the region of exponential growth seaward of the turning point, where magnitudes often greatly exceed 4, is black in fig. 4.2a,c.

For integer mode numbers, both f_A and f_B converge to the classical non-dissipative solution of Eckart (1951) as λ tends to zero. However, this convergence is non-uniform. For finite λ, there is always a neighborhood of $x = 0$ in which f_A differs greatly from the non-dissipative solution. Similarly, for finite λ, f_B differs greatly from the non-dissipative solution for sufficiently large x.

All shore-oblique shallow water waves have a turning point at $\chi = 4n + 2$. Near the turning point, waves propagate almost parallel to the shore. However, when n becomes large, the turning point moves far offshore, and near the shore the wave field becomes almost shore-normal. When $n \to \infty$ and x is fixed, f_B tends towards the dissipative shore-normal homogeneous solution

$$\hat{\eta}(x) = J_0\left[2\left(\frac{\omega^2(1 + i\lambda/\omega)x}{g\beta}\right)^{1/2}\right], \tag{4.22}$$

where J_0 is the zero-order Bessel function (Magnus *et al.*, 1966, 2nd identity, Section 6.7.1). However, at the turning point,

$$kh = \beta(2n + 1). \tag{4.23}$$

For sufficiently large n, kh is order-one at the turning point, and the shallow water approximation fails. If β is small, this problem can be overcome by matching the shallow water solution to a fully-dispersive WKB solution. If $\beta(2n+1) > 1$, the resulting waves are leaky waves. I have assumed that shallow water theory holds at leading order, which is true at the turning point only when $\beta(2n+1) \ll 1$. Consequently, leaky waves are excluded from my analysis. I discuss the possible importance of leaky waves in Sections 4.3.2 & 4.3.4.

4.3 Model results

The functions f_A and f_B shown in fig.'s 4.1 & 4.2, together with conditions (4.17) & (4.18), determine the wave field generated by point forcing. The wave field generated by distributed forcing is an integral of responses to point forcing (eq. (4.19)). Consequently, much of the qualitative behaviour of forced, dissipative shallow water waves can be determined by inspection of fig.'s 4.1 & 4.2. This Section contains examples of forced, dissipative shallow water waves, which illustrate physical phenomena such as refractive trapping, resonance, evanescence, and dissipative decoupling.

4.3.1 Edge waves

Figure 4.3 shows Green's functions for dissipative waves of 40 s period, forced shoreward of the edge wave turning point (at $x = 140$ m), on a planar beach of slope 0.02. The cross-shore structure of the weakly-dissipated mode 2 wave (fig. 4.3a,b) is very similar to the cross-shore structure of a free mode 2 edge wave (Mei, 1983, p.156). The cross-shore structure of the weakly-dissipated mode 2.5 wave (fig. 4.3c,d) depends strongly on the location of the forcing, and differs from the structure of free waves. I refer to both mode 2 and mode 2.5 waves as 'edge waves', because both are trapped close to the shore (near the edge of the ocean) by refraction. Figure 4.3e–h shows strongly-dissipated mode 2 and 2.5 waves. The wave field is now a mixture of cross-shore standing waves and cross-shore progressive waves. The waves are still trapped near the shore by refraction, and therefore can still be called 'edge waves'. Since edge waves also propagate alongshore (with speed

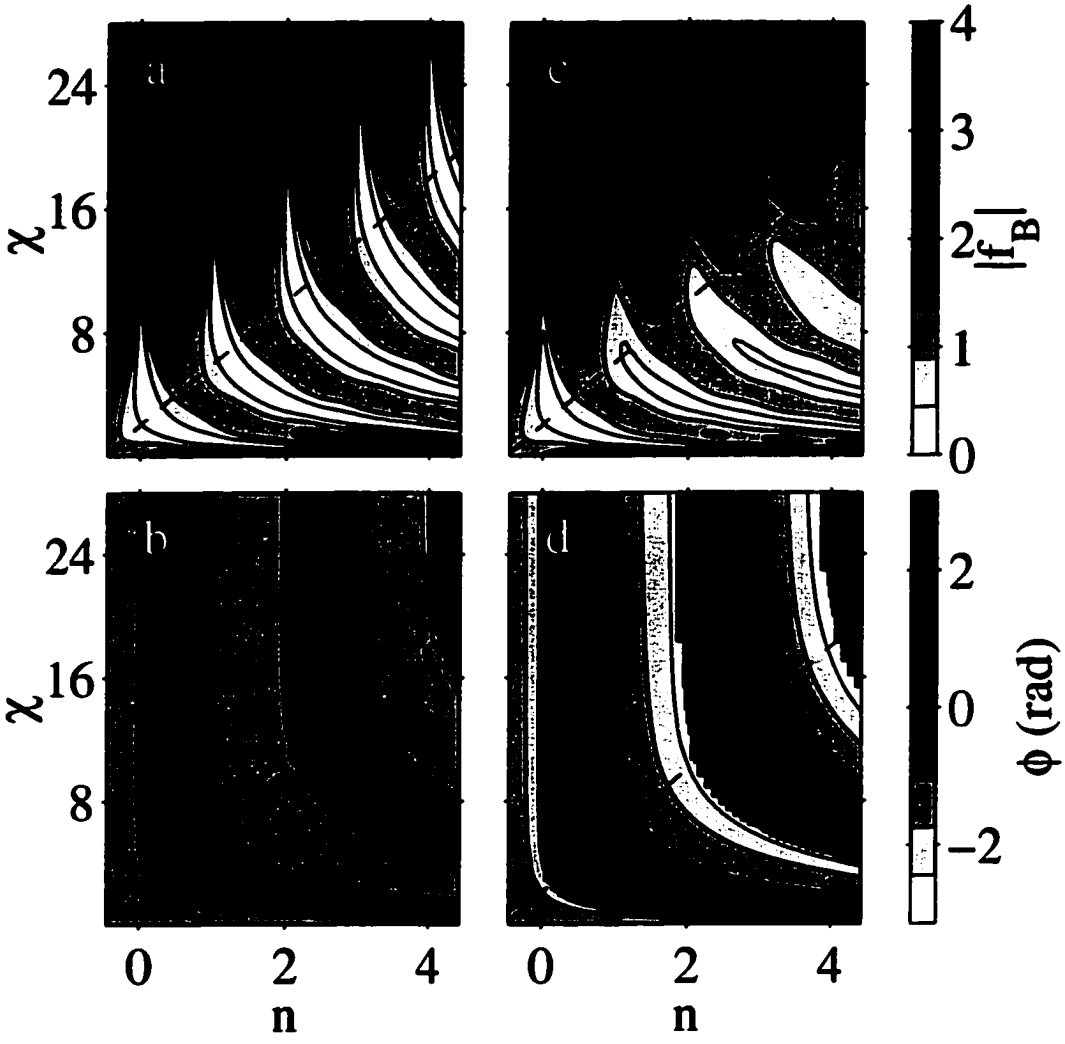

Figure 4.2: Dependence of homogeneous solution f_B on mode number n and distance from shore $\chi = 2kx$. Dashed line is edge wave turning point, at which $(gh)^{1/2} = \omega/k$. a,c: magnitude $|f_B|$, b,d: phase ϕ, where $f_B = |f_B|e^{i\phi}$. a,b: $\lambda/\omega = 3 \times 10^{-3}$, c,d: $\lambda/\omega = 8 \times 10^{-2}$.

ω/k), the cross-shore propagating waves of fig. 4.3 propagate at an oblique angle to the shore.

Shoreward-propagating waves reflect from the shore, resulting in the modal structure described by the function f_B, whereas seaward-propagating waves reflect from the edge wave turning point, resulting in the modal structure described by f_A. If the mode number n is an integer, the two modal structures coincide and resonant edge waves are generated. For this reason, the mode 2 edge waves of fig. 4.3 have larger amplitudes than the mode 2.5 waves, although this difference was small when dissipation was strong. Figure 4.4 shows how the total potential energy

$$V = \frac{g}{2} \int_{x=0}^{\infty} |\hat{\eta}(x)|^2 \, dx \tag{4.24}$$

of weakly-dissipative edge waves ($\lambda = 2.5 \times 10^{-3}$ s^{-1}) depends on the cyclic frequency and wavenumber of unit forcing applied 1 m from the shore ($\hat{F} = \delta(x - 1 \text{ m})$) on a planar beach of slope 0.02 (the cyclic wavenumber and frequency are $k_c = k/(2\pi)$ and $\omega_c = \omega/(2\pi)$ respectively). Figure 4.5 shows $V(\omega_c, k_c)$ for strongly-dissipative edge waves ($\lambda = 5 \times 10^{-2}$ s^{-1}) forced at the same location on the same beach. V was not calculated in the region $\omega^2 > gk/2$, where shallow water theory is inaccurate (Section 4.2.3). The solid curves indicate the wavenumbers and frequencies of resonant edge waves ($n = \{0, 1, 2, \ldots, 7\}$, see eq. (4.21)). As expected, resonant edge waves dominate when dissipation is weak. Strong dissipation limits resonance. Extensive experiments with the model indicate that, when broad-banded forcing is applied near the shore, the energy density of strongly resonant modes is $O(Q^2)$ times greater than the energy density of non-resonant modes (Q calculated from eq. (1.1), where the total dissipation rate equals the cross-shore integral of $h\lambda\overline{(|u|^2 + |v|^2)}$). Also, the bandwidth of resonances is $O(Q^{-1})$, so the total energy of resonant edge waves is $O(Q)$ times larger than the energy of non-resonant edge waves. These results are standard for resonant systems (Green, 1955). λ^{-1} is a time scale for dissipation, so Q scales with ω/λ. In Appendix F, these results are derived in a more elegant manner, using normal modes theory. Very different results were obtained when forcing was applied seaward of the edge wave turning point, as will be discussed in Section 4.3.2.

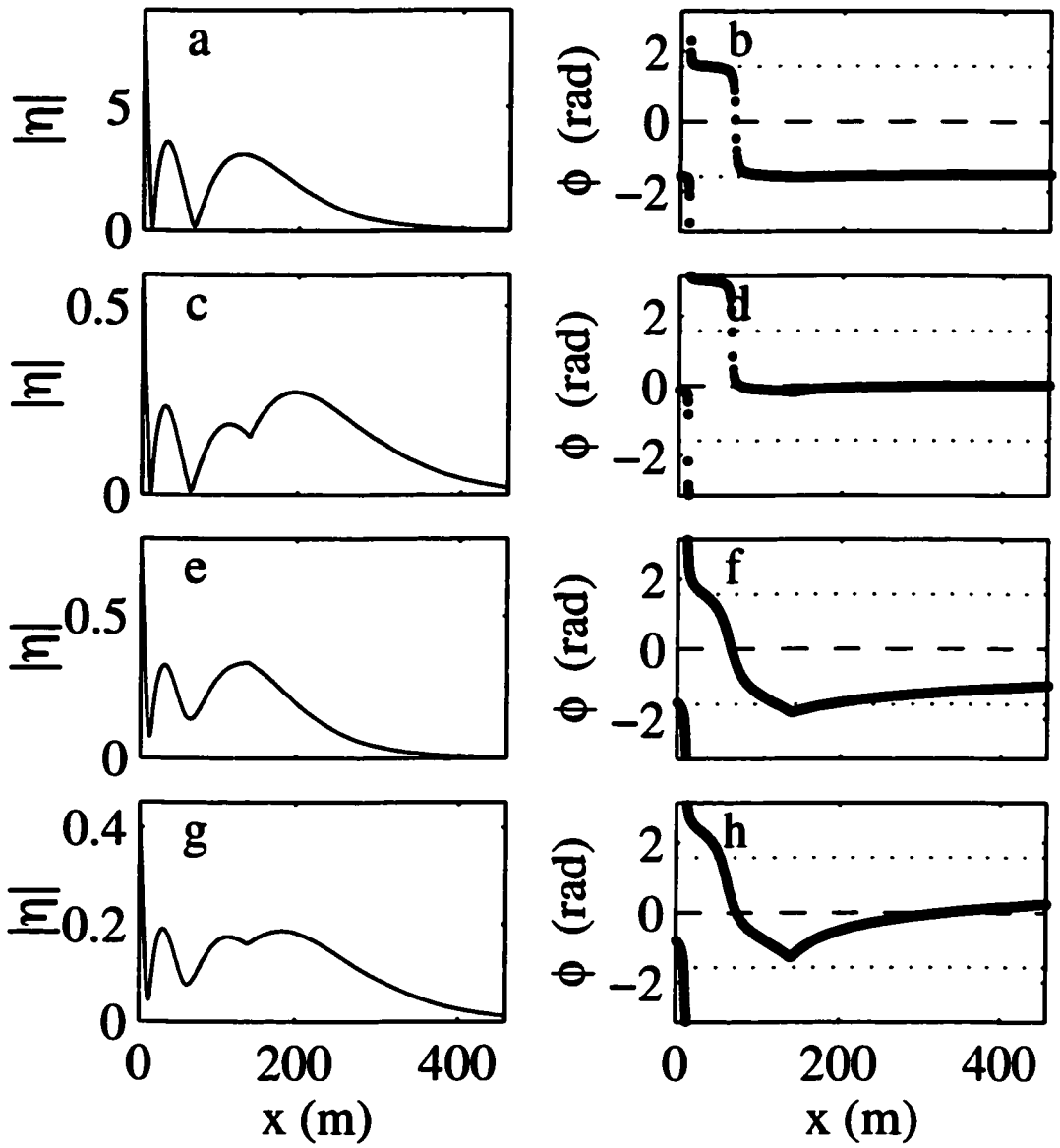

Figure 4.3: Edge waves forced at $x = 140$ m. a,c,e,g: magnitude $|\eta|$. b,d,f,h: phase ϕ. a,b: resonant ($n = 2$), weak dissipation ($\lambda/\omega = 1.6 \times 10^{-2}$). c,d: non-resonant ($n = 2.5$), weak dissipation ($\lambda/\omega = 1.6 \times 10^{-2}$). e,f: resonant ($n = 2$), strong dissipation ($\lambda/\omega = 1.6 \times 10^{-1}$). g,h: non-resonant ($n = 2.5$), strong dissipation ($\lambda/\omega = 1.6 \times 10^{-1}$).

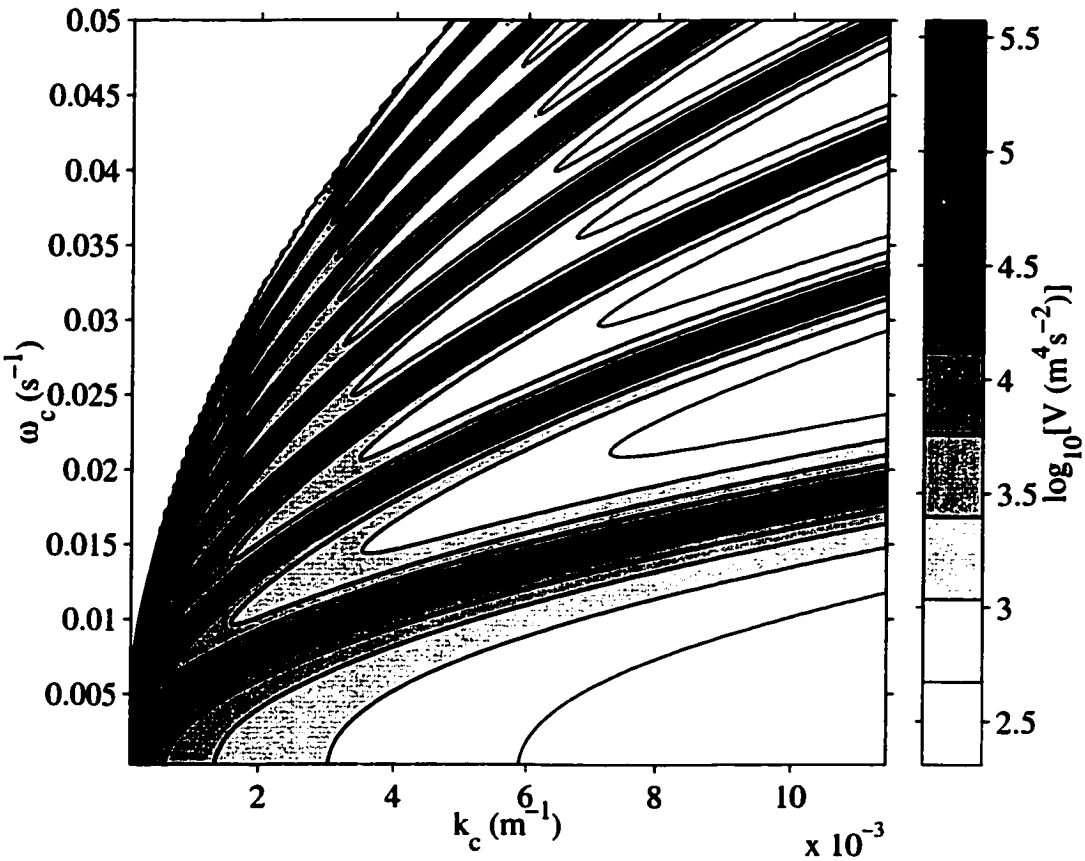

Figure 4.4: Potential energy V of forced, weakly-dissipative ($\lambda = 2.5\times10^{-3}$ s^{-1}) edge waves *versus* cyclic wavenumber k_c and cyclic frequency ω_c. Solid lines indicate integer mode numbers.

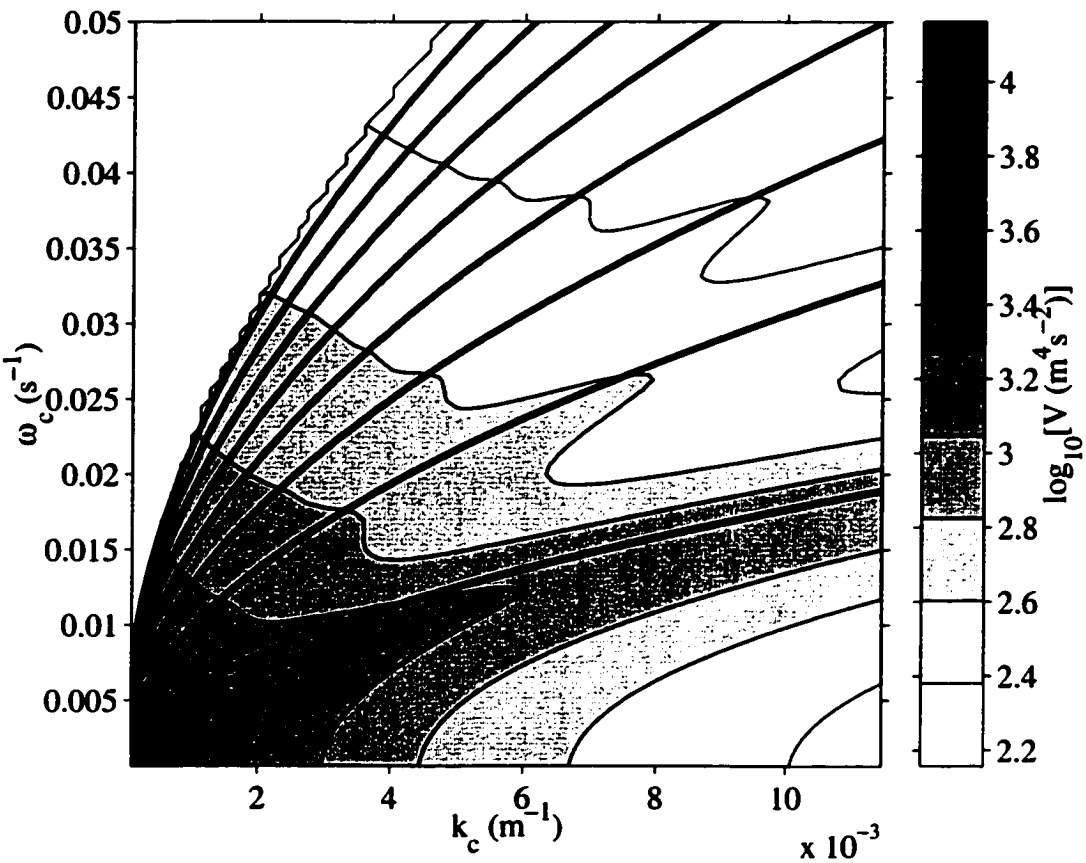

Figure 4.5: Potential energy of forced, dissipative ($\lambda = 5\times10^{-2}$ s^{-1}) edge waves V *versus* cyclic wavenumber k_c and cyclic frequency ω_c. Solid lines indicate integer mode numbers.

Propagating shallow water waves carry an energy flux, equal to the mean depth-integrated product of water pressure and velocity (Section 2.2). The divergence of the energy flux equals the rate of net generation of surf beat energy (negative if dissipation exceeds generation) (Section 2.2).

As was discussed in Section 4.2.2, the sea level fluctuates in response to the forcing $\hat{F} = \hat{F}_1 + \hat{F}_2$ (eq.'s (4.5), (4.10), (4.11), and (4.12)), whereas the cross-shore velocity is unaffected by $\hat{F}_2$ (eq.'s (4.1) & (4.12)). Consequently, the cross-shore energy flux depends not only on $\hat{F}$, but also on the manner in which $\hat{F}$ is partitioned into $\hat{F}_1$ and $\hat{F}_2$. Figure 4.6a,c,e,g shows the shoreward energy flux carried by the edge waves of fig. 4.3 when $\hat{F} = \hat{F}_2$ (so $\hat{F}_1 = 0$). Infragravity energy is generated at the point of forcing (where the divergence of the energy flux is singular and positive), and carried to surrounding regions of dissipation (where the energy flux converges). Figure 4.6b,d,f,h shows the cross-shore energy flux carried by the edge waves of fig. 4.3 when $\hat{F} = \hat{F}_1$ (so $\hat{F}_2 = 0$). Shoreward of x_F, the motion is unforced and the shoreward energy flux is the same as it was when $\hat{F} = \hat{F}_2$. Seaward of x_F, $hF_x - \partial M_x/\partial t$ is non-zero, and the energy flux usually diverges, indicating that the work done by the forcing usually exceeds dissipation. However, in some parts of the region $x > x_F$, dissipation exceeds forcing and the energy flux converges.

In the field, the non-dimensional energy flux ρ (eq. (2.33)) is as large as 0.5 during storms, indicating strong shoreward propagation. Figure 4.7 shows the non-dimensional energy flux ρ for the edge waves presented in fig. 4.3. Shoreward of the turning point, both resonant and non-resonant weakly-dissipative edge waves are almost cross-shore standing, so $\rho \approx 0$ (fig. 4.7a–d). In contrast, strongly-dissipative edge waves propagate across-shore (fig. 4.3e–h), and have $|\rho|$ values as large as 0.5. Outside the turning point, ρ departs from zero in the weakly-dissipative, resonant case shown in fig. 4.7b, although the associated energy flux is very small (fig. 4.6b). Cross-shore energy transport outside the turning point is discussed in the next section.

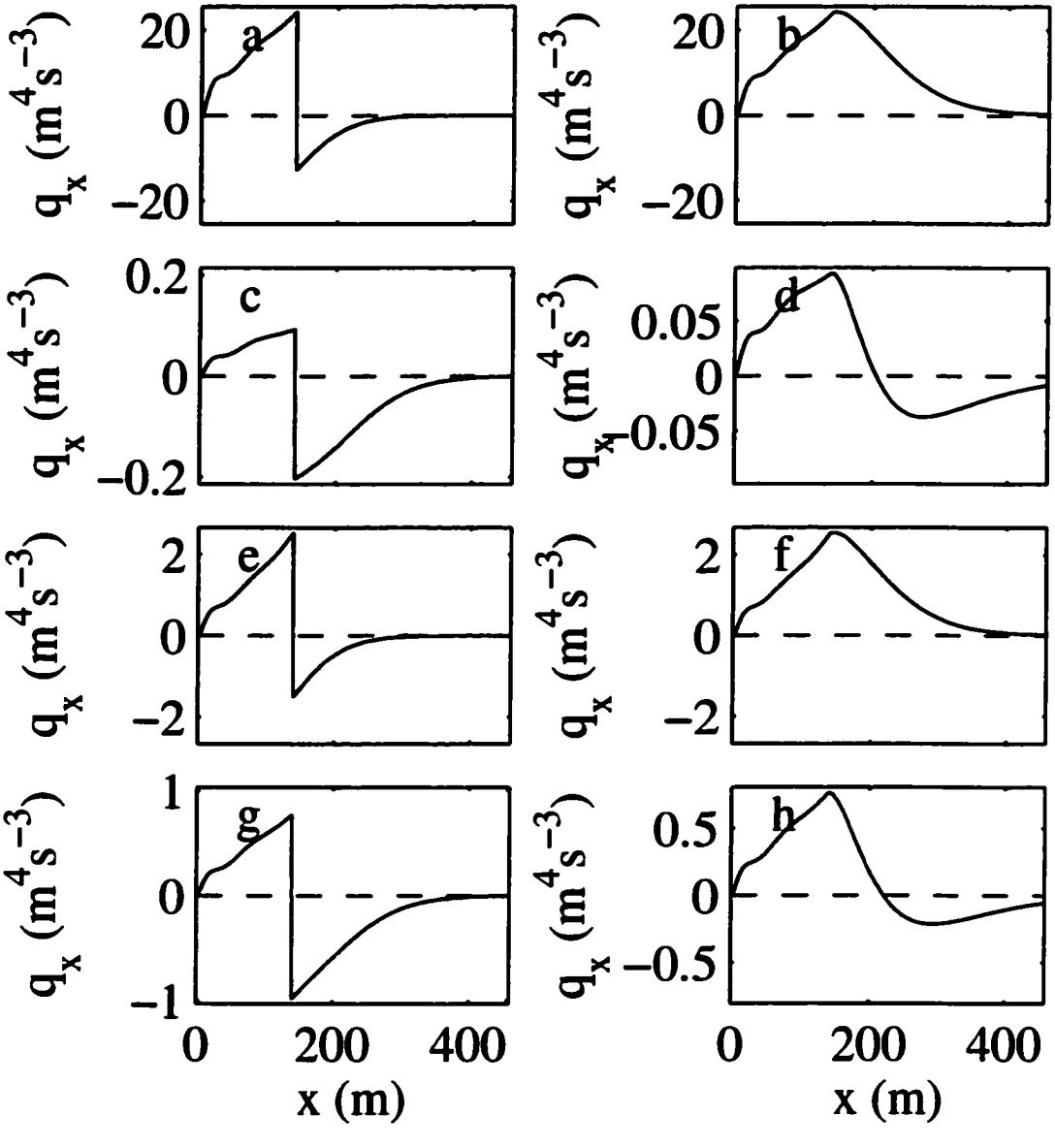

Figure 4.6: Shoreward energy flux q_x carried by edge waves of fig. 4.3. a,c,e,g: Longshore forcing ($\hat{F}_1 = 0$). b,d,f,h: Cross-shore forcing ($\hat{F}_2 = 0$). For a discussion of longshore and cross-shore forcing, see Section 4.2.2. a,b: $n = 2$, $\lambda/\omega = 1.6 \times 10^{-2}$. c,d: $n = 2.5$, $\lambda/\omega = 1.6 \times 10^{-2}$. e,f: $n = 2$, $\lambda/\omega = 1.6 \times 10^{-1}$. g,h: $n = 2.5$, $\lambda/\omega = 1.6 \times 10^{-1}$.

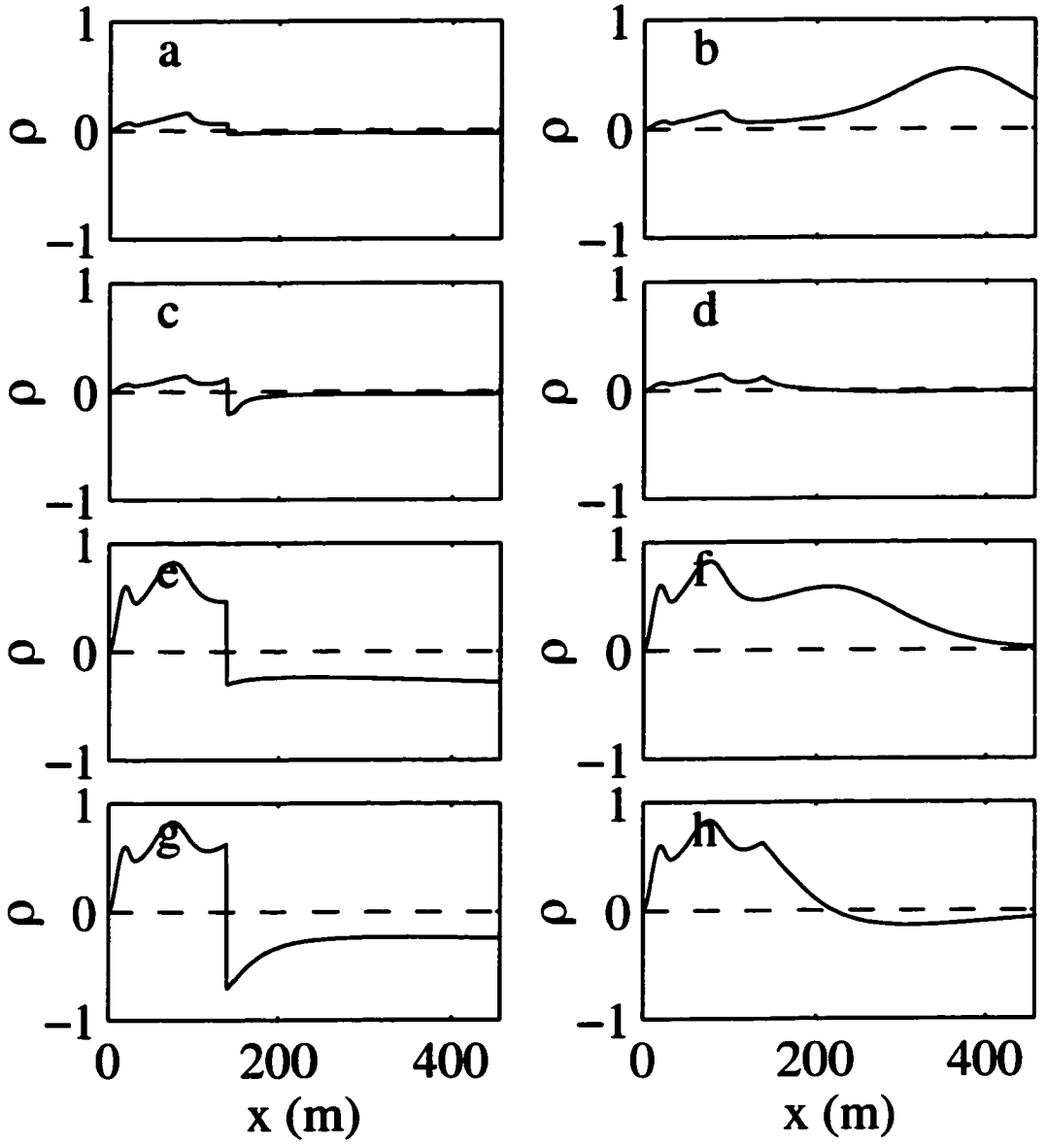

Figure 4.7: Dimensionless shoreward energy flux ρ carried by edge waves of fig. 4.3. a,c,e,g: Longshore forcing ($\hat{F}_1 = 0$). b,d,f,h: Cross-shore forcing ($\hat{F}_2 = 0$). For a discussion of longshore and cross-shore forcing, see Section 4.2.2. a,b: $n = 2$, $\lambda/\omega = 1.6 \times 10^{-2}$. c,d: $n = 2.5$, $\lambda/\omega = 1.6 \times 10^{-2}$. e,f: $n = 2$, $\lambda/\omega = 1.6 \times 10^{-1}$. g,h: $n = 2.5$, $\lambda/\omega = 1.6 \times 10^{-1}$.

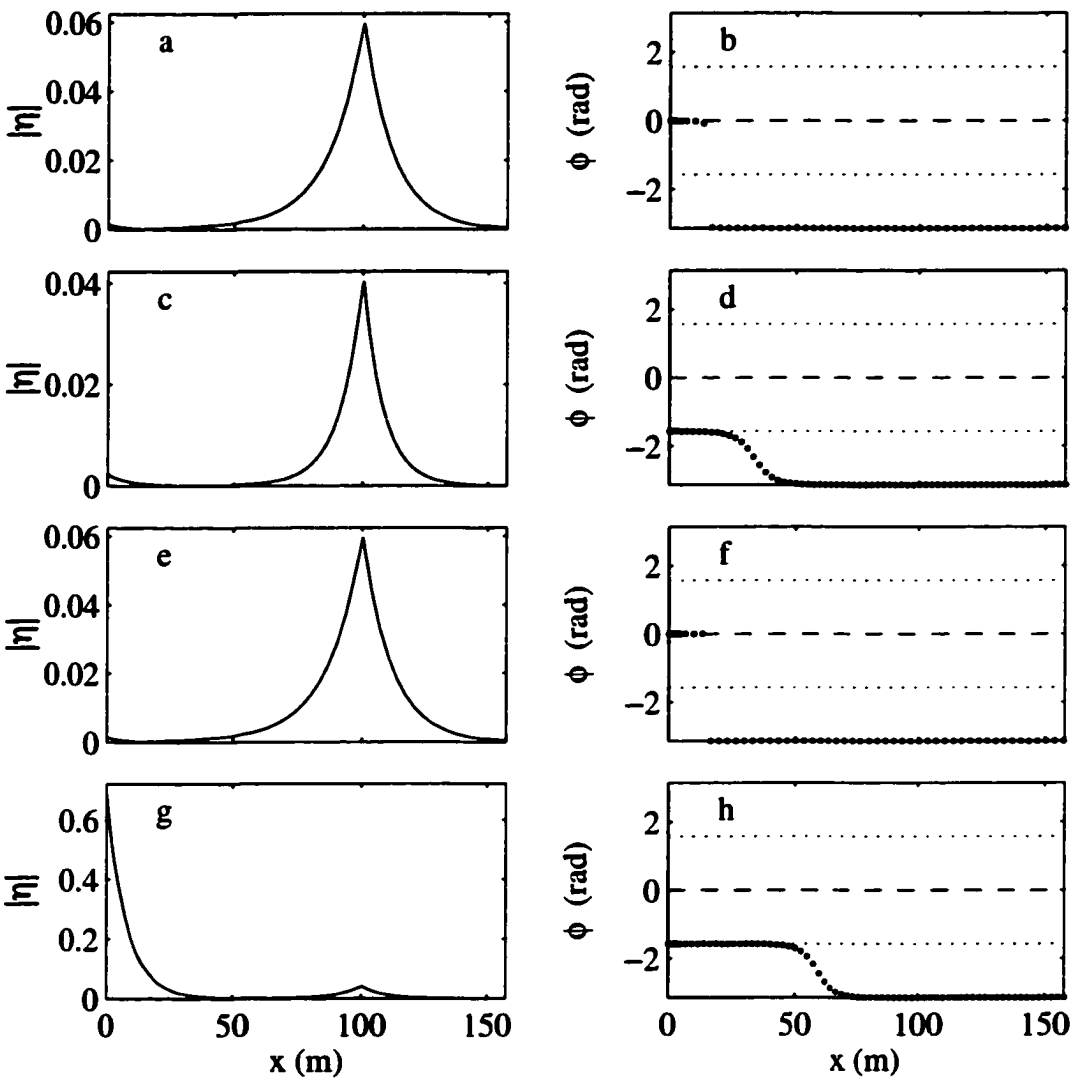

Figure 4.8: Point-forced evanescent and edge waves. Wave period is 40 s. a,c,e,g: magnitude $|\eta|$. b,d,f,h: phase ϕ. a,b: non-resonant ($n = 0.2$), weak dissipation ($\lambda/\omega = 3 \times 10^{-3}$). c,d: resonant ($n = 0$), weak dissipation ($\lambda/\omega = 3 \times 10^{-3}$). e,f: non-resonant ($n = 0.2$), very weak dissipation ($\lambda/\omega = 1 \times 10^{-5}$). g,h: resonant ($n = 0$), very weak dissipation ($\lambda/\omega = 1 \times 10^{-5}$).

4.3.2 Evanescent waves

Forcing applied shoreward of the edge wave turning point generates edge waves (Section 4.3.1). Figure 4.8 shows that very different behaviour can result when forcing is applied seaward of the turning point ($x_F = 100$ m, $x_T \approx 8$ m). Only when forcing was resonant, and dissipation was extremely weak, were energetic edge waves excited (fig. 4.8g,h). Otherwise, only localised waves were generated (fig. 4.8a–f). These localised waves were 'evanescent', that is, they did not propagate freely, but decayed approximately exponentially with cross-shore distance away from the point of forcing.

A simple model explains the behaviour shown in fig. 4.8. From eq. (1.1), the edge wave energy dissipated in a single period is

$$\mathcal{D} = \frac{2\pi g a_{edge}^2 x_T}{Q}, \tag{4.25}$$

where $g a_{edge}^2 x_T$ is the total energy of the edge wave, and a_{edge} is a typical edge wave amplitude.

Forcing is applied only outside the turning point, so the energy flux carried to the turning point by evanescent waves must balance the edge wave dissipation $\mathcal{D}$. I will derive an approximate expression for the energy flux carried to the turning point by evanescent waves, and then calculate the relative amplitudes of edge and evanescent waves by equating this energy flux with edge wave dissipation. The energy flux carried by evanescent waves is mathematically analogous to the probability flux carried by quantum-mechanical particles tunneling through a potential barrier (Ohanian, 1990, Section 3). Consequently, the evanescent wave energy flux can be estimated using standard methods of quantum mechanics. A crude approximation of the cross-shore structure of evanescent waves is

$$\hat{\eta} \approx a_1 e^{i\phi_1} e^{-K(x-x_T)} + a_2 e^{i\phi_2} e^{K(x-x_F)}, \tag{4.26}$$

where a_1 and a_2 are approximately the evanescent wave amplitudes at x_T and x_F respectively, ϕ_1 and ϕ_2 are real constants, and $K > 0$. The cross-shore e-folding distance for evanescent waves is (Longuet-Higgins, 1967, p.788)

$$K^{-1} \approx [k^2 - \omega^2/(gh)]^{-1/2}. \tag{4.27}$$

Equation (4.27) is simplified by assuming $h \approx \beta(x_T + x_F)/2$, which is the water depth half way between the point of forcing and the turning point. From eq.'s (2.21), (4.1), (4.26) & (4.27), the amount of energy carried to the turning point by evanescent waves in a single period is

$$\frac{2\pi q_x}{\omega} \approx \frac{4\pi K h g^2}{\omega^2} \mathrm{e}^{-KL} a_1 a_2 \sin(\phi_1 - \phi_2), \tag{4.28}$$

where $L = x_F - x_T$. When KL is large, evanescent waves decay greatly between the point of forcing and the turning point, and therefore can carry very little energy to the turning point.

Equating edge wave forcing and dissipation, noting that $h/x_T \approx \beta$, $a_1 \approx a_{edge}$, $a_2 \approx a_{ev}$ (where a_{ev} is the evanescent wave amplitude at x_F), leads to

$$\frac{a_{edge}}{a_{ev}} = O\left(\frac{K}{k}\left[\frac{\sin(\phi_1 - \phi_2)}{n + 1/2}\right] Q\mathrm{e}^{-KL}\right). \tag{4.29}$$

(eq. (4.29) has been simplified using eq. (4.21)). The ratio between edge and evanescent wave amplitudes depends on their relative phase $\phi_1 - \phi_2$. For resonant edge waves, $\phi_1 - \phi_2 \approx \pi/2$, so $\sin(\phi_1 - \phi_2) \approx 1$ (eg. fig. 4.8d,h). In contrast, $\phi_1 - \phi_2$ can be close to π or 0 (so $\sin(\phi_1 - \phi_2)$ can be much less than one) if edge waves are non-resonant (eg. fig. 4.8b,f). Figure 4.9 shows that eq. (4.29), with $\sin(\phi_1 - \phi_2) = 1$, predicted the ratio between evanescent and resonant edge wave amplitudes to within a factor of 2, except when edge waves were much larger than evanescent waves ($a_{edge}/a_{ev} \approx 10$) and KL is small ($KL = 2$). For $KL < 2$, forcing is very close to the turning point, and eq. (4.29) fails. Non-resonant edge waves are much smaller than evanescent waves when KL is large. If forcing is broad-banded, then the bandwidth of the spectral peaks associated with resonant edge waves is $O(Q^{-1})$ (Section 4.3.1), so the ratio between total edge and evanescent wave energy scales with $Q\mathrm{e}^{-2KL}/[(n + 1/2)k/K]^2$. When KL is large, evanescent waves can dominate over edge waves, even if $Q \gg 1$.

According to shallow water theory, all shore-oblique waves have a turning point, seaward of which waves are evanescent. In reality, waves have a turning point if and only if $\omega^2 < gk$. If $\omega^2 > gk$, waves are leaky and are nowhere evanescent. Therefore, when

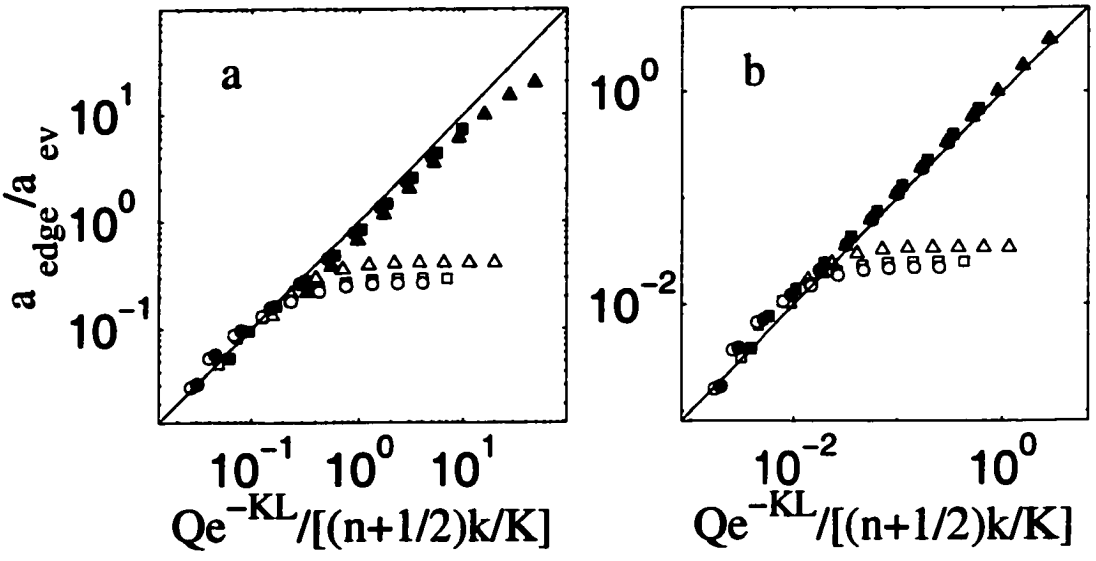

Figure 4.9: Ratio between edge and evanescent wave amplitudes, a_{edge}/a_{ev}, *versus* ratio predicted by eq. (4.29), with $\sin(\phi_1 - \phi_2) = 1$. Wave period is 40 s. a: $KL = 2$. b: $KL = 5$. Solid black symbols indicate resonant waves, n = 0,1,2 for triangles, squares, and circles respectively. Empty symbols indicate non resonant waves, n = 0.25,1.25,2.25 for triangles, squares, and circles respectively.

$\omega^2 < gk$, forcing sufficiently far offshore produces only a localised evanescent response, whereas when $\omega^2 > gk$, energy can always be radiated far from the point of forcing.

4.3.3 Dissipative decoupling

Schönfeldt (1995), Bryan and Bowen (1996), and Bryan *et al.* (1998) showed that refraction can trap edge waves over sandbars. When waves are trapped over sandbars, evanescent waves exist between the sandbar and the beach. Evanescent waves transport very little energy over cross-shore distances large compared with $(k^2 - \omega^2/gh)^{-1/2}$ (Section 4.3.2). Consequently, the region of evanescent waves shoreward of the sandbar is a barrier to energy transport which can effectively decouple dissipative bar- and shore-trapped waves.

If forcing is applied only over the sandbar, and a region of evanescent waves exists between the sandbar and the shore, then an argument similar to the one used to derive eq. (4.29) leads to

$$\frac{a_{shore}}{a_{bar}} = O\left(\frac{K}{k}\left[\frac{\sin(\phi_s - \phi_b)}{n + 1/2}\right] Q\mathrm{e}^{-KL}\right), \tag{4.30}$$

where a_{shore} and a_{bar} are the amplitudes of shore- and bar-trapped waves respectively, L is the width of the region of evanescent waves in the trough, ϕ_b and ϕ_s are the respective phases of bar- and shore-trapped waves at their turning points, and n is the mode number of the shore-trapped wave. K^{-1} is the e-folding distance for evanescent waves in the trough, which I crudely approximate by $[k^2 - 2\omega^2/g(h_T + h_{trough})]^{-1/2}$, where h_T is the turning depth, and h_{trough} is the maximum water depth in the trough. As in Section 4.3.2, $\sin(\phi_b - \phi_s)$ is about one (zero) if shore-trapped waves are (are not) resonant.

If forcing is applied at the shoreface, then a_{bar}/a_{shore} approximately equals the negative of the right-hand side of eq. (4.30) (the term $n+1/2$ is modified, but on realistic beaches the order of magnitude of a_{bar}/a_{shore} remains unchanged). If $Q\mathrm{e}^{-KL}/[(n + 1/2)k/K] \ll 1$, then forcing over the bar does not generate significant shore-trapped waves, and forcing over the shoreface does not generate significant bar-trapped waves. In this case, bar- and shore-trapped waves have negligible influence on one-another, and we say that they are 'dissipatively decoupled'. If the trough is wide and deep, then even high Q waves can be

decoupled.

An example of a barred beach is shown in fig. 4.10. I solve eq.'s (4.1), (4.2) & (4.3) for the beach shown in fig. 4.10 by patching together planar beach solutions, as described in Appendix E.

Figure 4.11 shows how the total potential energy of weakly-dissipative waves V (eq. (4.24)) depends on the wavenumber and frequency of unit forcing applied 0.3 m from the shore ($\hat{F} = \delta(x - 0.3\text{ m})$). V is presented for both infragravity and incident frequencies, because field observations show that bar-trapped waves can be important at incident frequencies (Bryan *et al.*, 1998). Shoreward of the trough, the barred beach of fig. 4.10 has a slope of 0.045, so resonant waves trapped shoreward of the trough will have wavenumbers and frequencies close to the wavenumbers and frequencies of resonant edge waves on a planar beach of slope 0.045. The solid curves of fig. 4.11 mark these planar-beach resonance curves ($n = \{0, 1, 2, 3\}$, see eq. (4.21)).

If the edge wave turning depth (h_T) is greater than the maximum water depth in the trough (h_{trough}), then oscillatory edge waves exist over the entire region from the shore to the bar, and evanescent waves exist only seaward of the bar (Bryan and Bowen, 1996). I will call the region of wavenumber-frequency space where $h_T > h_{trough}$ 'Region 1'. The dash-dotted line in fig. 4.11 marks $h_T = h_{trough}$, so Region 1 lies above and to the left of this line.

When $h_{bar} < h_T < h_{trough}$, oscillatory waves exist over both the shoreface and the bar, and evanescent waves exist both in the trough and seaward of the bar. I will call the region of wavenumber-frequency space where $h_{bar} < h_T < h_{trough}$ Region 2. The dashed line in fig. 4.11 marks $h_T = h_{bar}$, so Region 2 lies between the dashed and dash-dotted lines. Trapping and amplification of edge waves over the bar occurs only in Region 2. Resonance curves for bar-trapped waves are lines in Region 2 lying almost parallel to $h_T = h_{bar}$ (Bryan and Bowen, 1996).

If $h_T < h_{bar}$, then oscillatory waves exist only on the shoreface, whereas evanescent waves exist over the trough, the bar, and seaward of the bar. The region of wavenumber-frequency space where $h_T < h_{bar}$, which I call Region 3, lies below and to the right of the

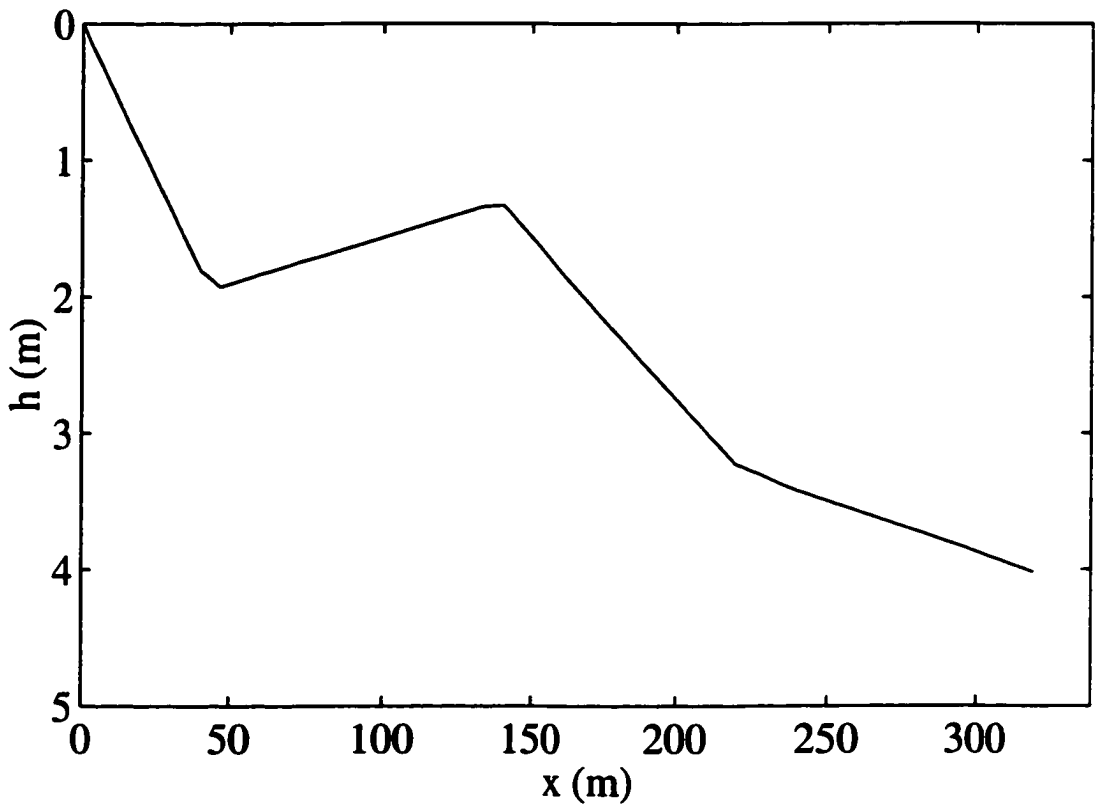

Figure 4.10: Barred beach profile. Water depth h *versus* distance from shore x. Beach slope is constant seaward of $x = 220$ m.

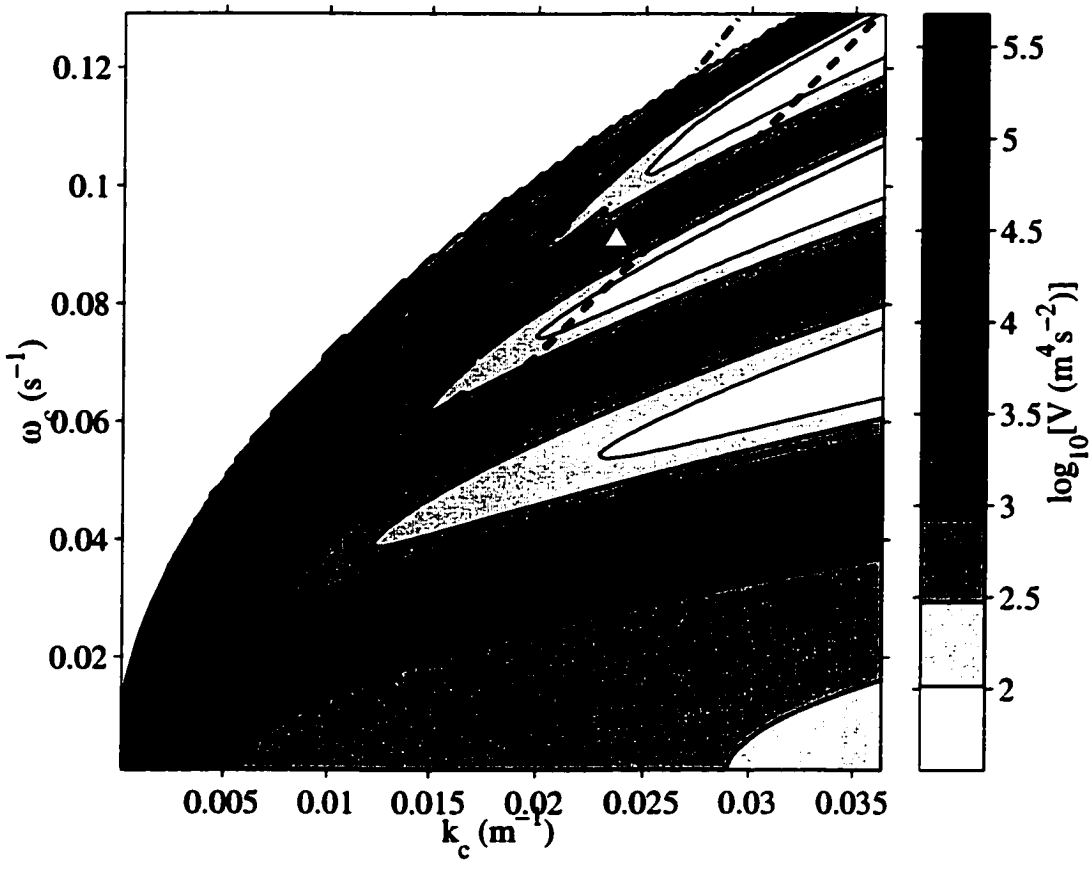

Figure 4.11: Potential energy V of weakly-dissipative ($\lambda = 5 \times 10^{-3}$ s^{-1}) waves forced near the shore *versus* cyclic frequency ω_c and longshore cyclic wavenumber k_c. Solid lines indicate resonances on a planar beach of slope 0.045. Dashed and dash-dotted lines indicate $\omega/k = (gh_{bar})^{1/2}$ and $\omega/k = (gh_{trough})^{1/2}$ respectively.

dashed line of fig. 4.11.

When forcing was applied close to the shore, energy in Region 1 was concentrated along curves that do not coincide with the planar-beach resonance curves (fig. 4.11). This is to be expected, since these waves were not trapped shoreward of the trough, where the beach was planar. In Regions 2 and 3, forcing close to the shore excited strongly resonant shore-trapped waves, so energy was concentrated along the predicted planar-beach resonance curves (fig. 4.11). At incident frequencies, dissipation has decoupled shore- and bar-trapped motions, so forcing over the shore has not excited bar-trapped waves. Consequently, at incident frequencies, there is no sign of the energy concentration along lines parallel to $h_T = h_{bar}$ in Region 2 that would indicate resonant bar-trapped waves. At low infragravity frequencies (<0.02 Hz), resonant waves have wavelengths comparable to the distance between the bar and the shore, so bar- and shore-trapped waves are not decoupled (KL is not large, see eq. (4.30)). Energy is concentrated along a line close to $h_T = h_{bar}$ at low infragravity frequencies, indicating that the bar had some influence on these waves.

When forcing was applied over the bar ($x = 140$ m), resonant bar-trapped waves were generated. Consequently, much energy was concentrated along resonance lines lying almost parallel to $h_{bar} = h_T$ in Region 2 (fig. 4.12). In Region 1, resonance curves did not coincide with shore-trapped resonance curves, due to the presence of the bar. Dissipative decoupling ensured that shore-trapped waves were not excited in Region 2, except at low infragravity frequencies (<0.02 Hz). In Region 3, forcing was applied far seaward of the turning point, where waves were evanescent, so shore-trapped waves were not excited for the reasons outlined in Section 4.3.2. Consequently, there was no energy concentration along planar-beach resonance curves. Comparison of fig.'s 4.11 & 4.12 shows that the number of resonance curves, and their location in (ω, k) space, can depend on the location of the forcing, even when $Q \gg 1$ (in this case $Q \approx 60$ for $(\omega, k) = (0.09096$ Hz, 0.0236 m$^{-1})$).

At the point $(\omega, k) = (0.09096$ Hz, 0.0236 m$^{-1})$ (marked with triangles in fig.'s 4.11 & 4.12), the resonance curves for bar-forced and shore-forced motions cross, and the cross-shore structure of waves depends entirely on the location at which they are forced

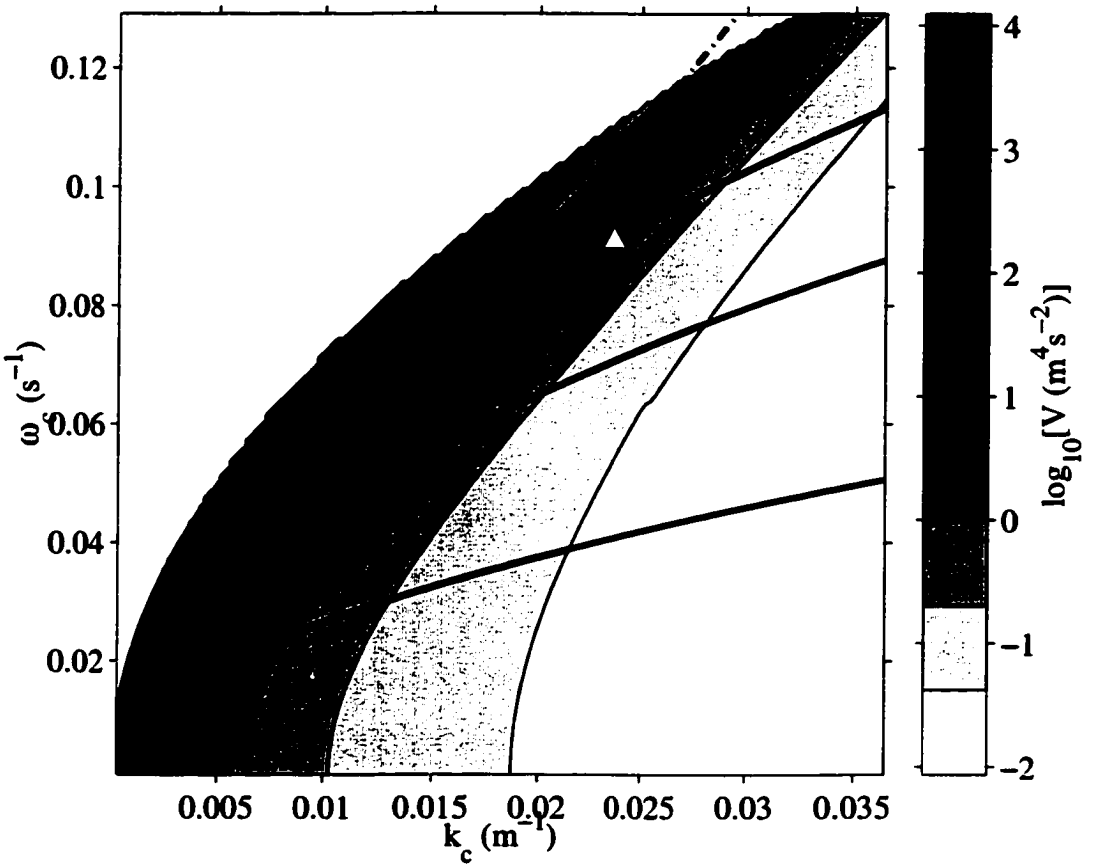

Figure 4.12: Potential energy V of weakly-dissipative ($\lambda = 5 \times 10^{-3}$ s^{-1}) waves forced near the bar crest *versus* cyclic frequency ω_c and longshore cyclic wavenumber k_c. Solid lines indicate resonances on a planar beach of slope 0.045. Dashed and dash-dotted lines indicate $\omega/k = (gh_{bar})^{1/2}$ and $\omega/k = (gh_{trough})^{1/2}$ respectively.

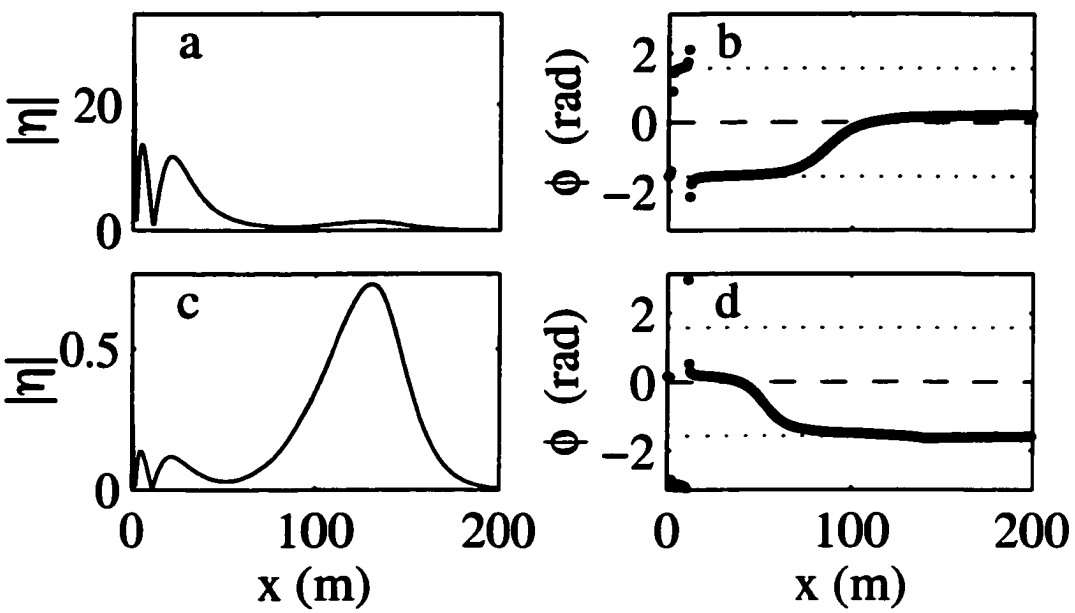

Figure 4.13: Weakly-dissipative ($\lambda = 5 \times 10^{-3}$ s^{-1}) waves of cyclic frequency 0.09096 Hz and cyclic wavenumber 0.0236 m^{-1}. a,c: magnitude $|\eta|$. b,d: phase ϕ. a,b: Forced near shore. c,d: Forced near bar crest.

(fig. 4.13). The shore-forced wave is a resonant mode 2 shore-trapped wave (fig. 4.13a,b). The bar-forced wave is a resonant mode zero bar-trapped wave (fig. 4.13c,d). Equation (4.30) predicts that the ratio between these shore- and bar-trapped amplitudes should be 0.13 when forcing is applied over the bar, roughly consistent with fig. 4.13.

Figure 4.14 shows the spectrum generated by forcing over the bar when dissipation was very weak. This spectrum is presented for only a small range of wavenumbers and frequencies, centered on $(\omega, k) = (0.09096 \text{ Hz}, 0.0236 \text{ m}^{-1})$. The bar-trapped resonance curve, which was present in the moderately dissipative case of fig. 4.12, is still clear in this very weakly-dissipative case. However, in contrast to the weakly-dissipative case, weak resonance curves now bifurcate from the bar-trapped resonance curve (fig. 4.14) at about the point $(\omega, k) = (0.09096 \text{ Hz}, 0.0236 \text{ m}^{-1})$. Figure 4.15 shows that these new resonance curves were associated with shore-trapped waves (dissipation was very weak and did not fully decouple bar-and shore-trapped waves). At the point $(\omega, k) = (0.09096 \text{ Hz}, 0.0236 \text{ m}^{-1})$, shore-trapped waves were slightly larger than bar-trapped waves (fig. 4.15c), consistent with eq. (4.30), which predicted $a_{shore}/a_{bar} = 1.3$.

Figure 4.16 shows the spectrum generated by forcing over the bar when dissipation was extremely weak, and fig. 4.17 shows the cross-shore structure of the associated resonant waves. At frequencies and wavenumbers sufficiently far from $(\omega, k) = (0.09096 \text{ Hz}, 0.0236 \text{ m}^{-1})$, both shore-trapped (fig. 4.17a,b,g,h) and bar-trapped (fig. 4.17e,f,k,l) resonances can be identified. At frequencies and wavenumbers very close to $(\omega, k) = (0.09096 \text{ Hz}, 0.0236 \text{ m}^{-1})$, resonant bar- and shore-trapped waves are excited simultaneously (fig. 4.17c,d,i,j). In these last cases bar- and shore-trapped waves were coupled by the small evanescent motions between the bar and the shoreface. This coupling modified resonance curves so that they did not cross (unlike in the partially-decoupled resonance curves of fig. 4.15).

Equation (4.30) predicts $a_{shore}/a_{bar} = 13$ at the point $(\omega, k) = (0.09096 \text{ Hz}, 0.0236 \text{ m}^{-1})$. Since this point lies between the two resonance curves shown in fig. 4.16, the associated waves are relatively small, and probably not important to the total flow field.

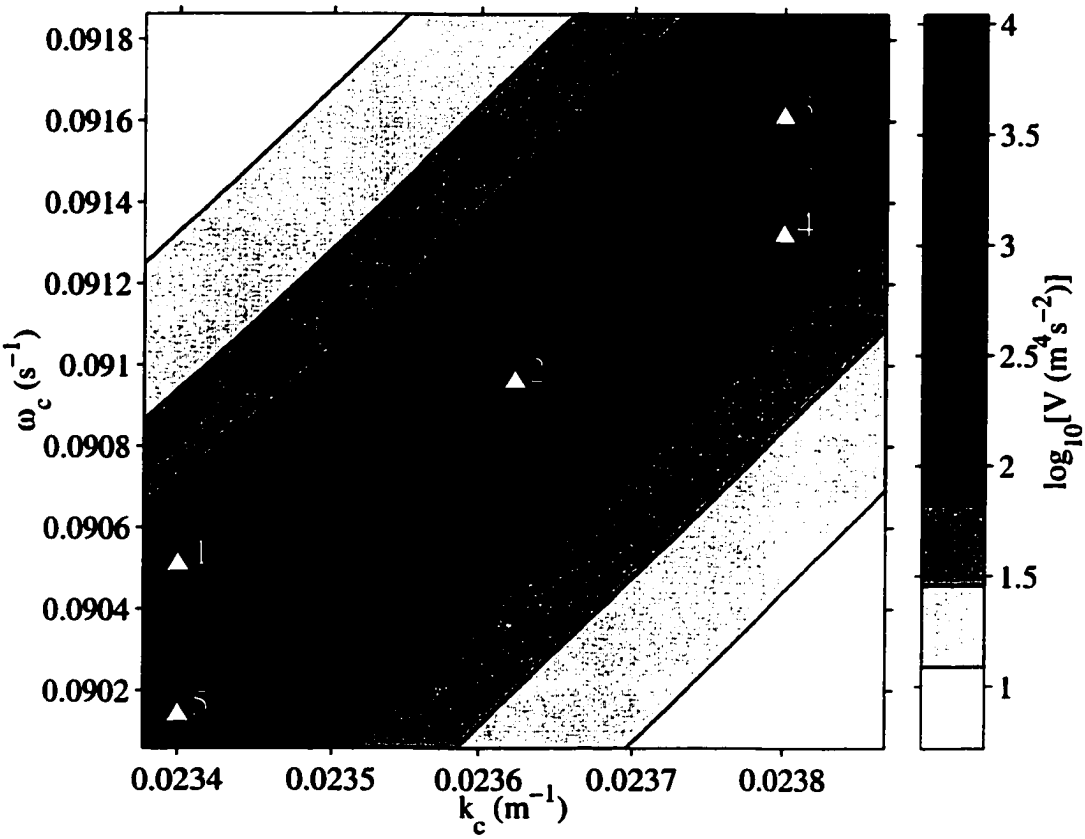

Figure 4.14: Potential energy V of very weakly-dissipative ($\lambda = 5 \times 10^{-4}$ s^{-1}) waves forced near the bar crest *versus* cyclic frequency ω_c and longshore cyclic wavenumber k_c. Solid line indicates mode 2 resonance on a planar beach of slope 0.045.

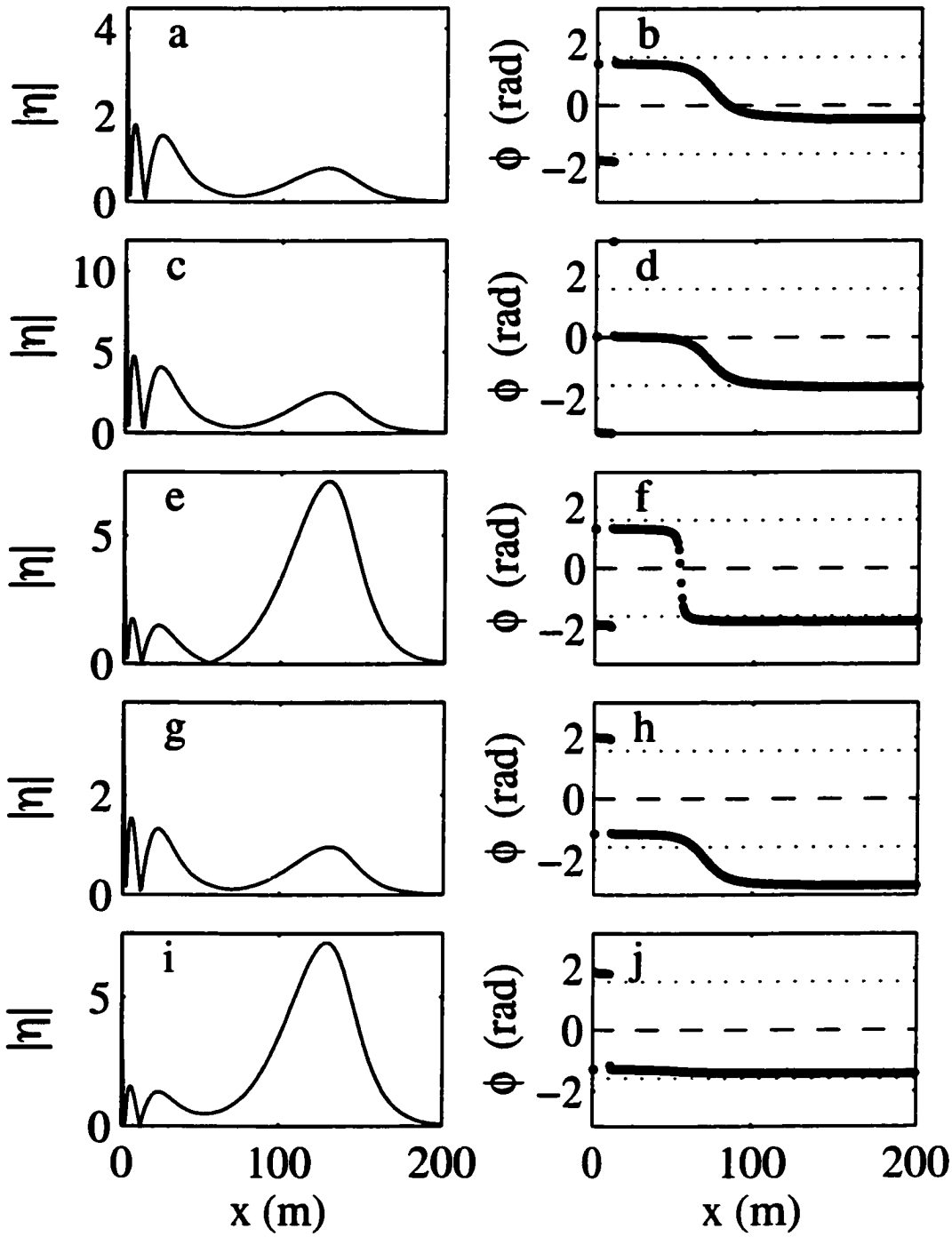

Figure 4.15: Very weakly-dissipative ($\lambda = 5 \times 10^{-4}$ s^{-1}) waves forced near bar-crest. a,c,e,g: magnitude $|\eta|$. b,d,f,h: phase ϕ. Wavenumbers and frequencies of waves are marked by triangles of fig. 4.14 as follows: a,b: triangle 1. c,d: triangle 2. e,f: triangle 3. g,h: triangle 4. i,j: triangle 5.

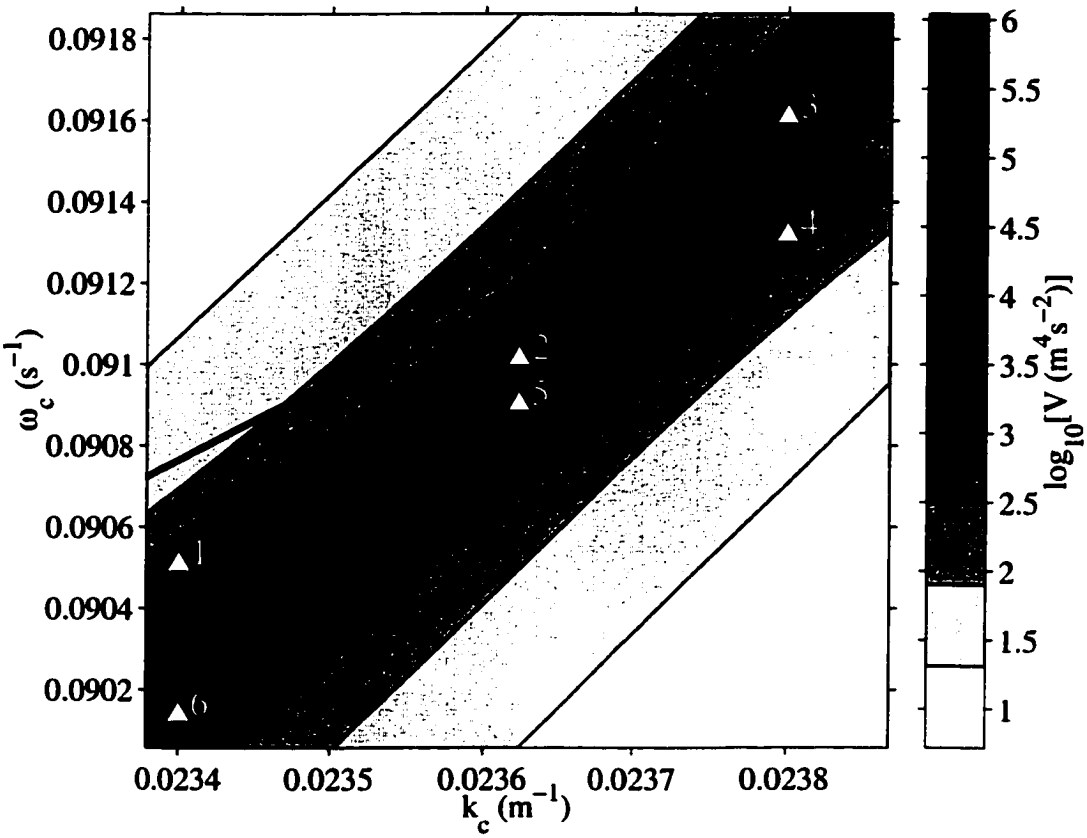

Figure 4.16: Potential energy V of extremely weakly-dissipative ($\lambda = 5 \times 10^{-5}$ s^{-1}) waves forced near the bar crest *versus* cyclic frequency ω_c and longshore cyclic wavenumber k_c. Solid line indicates mode 2 resonance on a planar beach of slope 0.045.

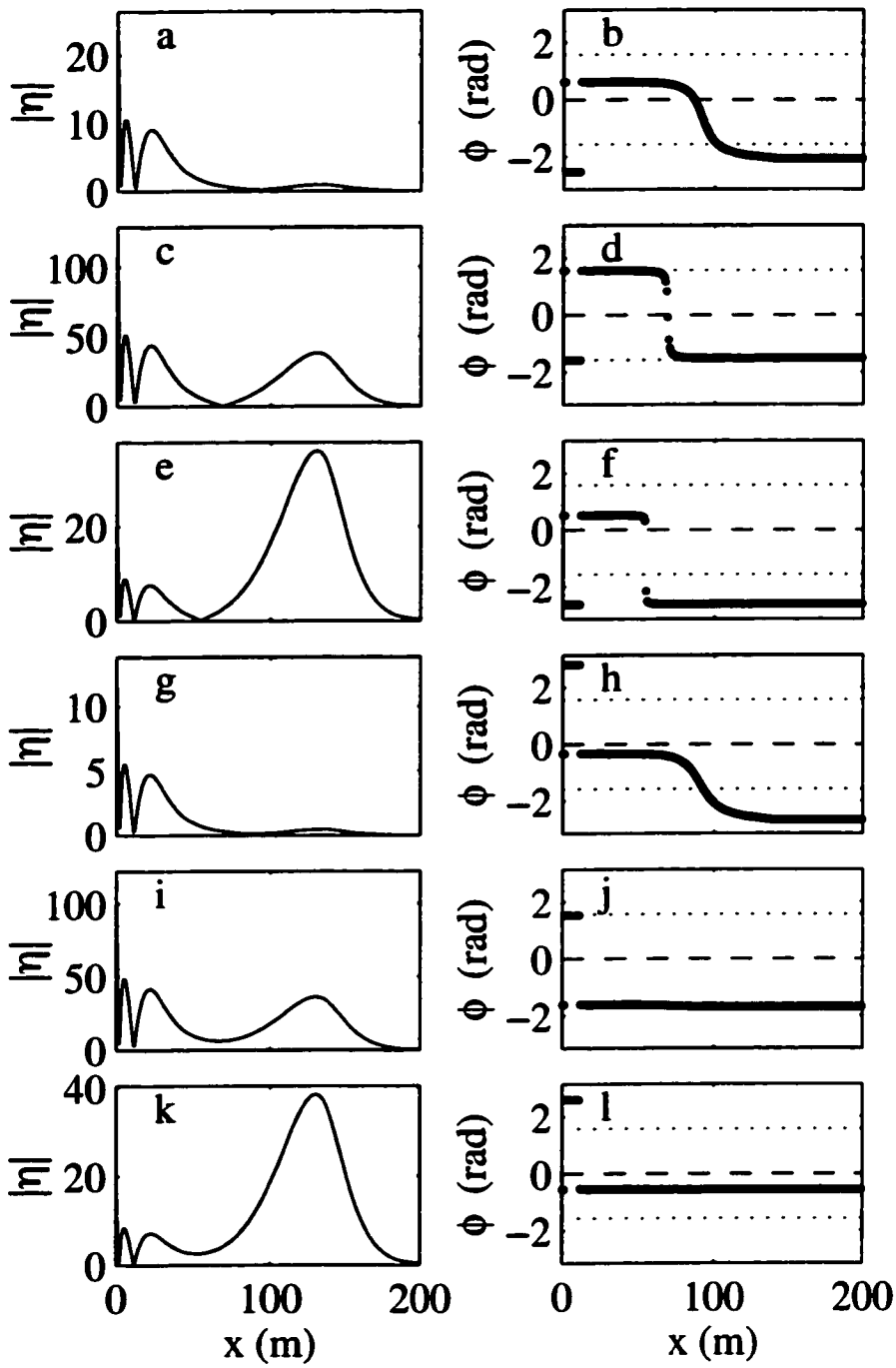

Figure 4.17: Extremely weakly-dissipative ($\lambda = 5 \times 10^{-5}$ s^{-1}) waves forced near bar-crest. a,c,e,g,i,k: magnitude $|\eta|$. b,d,f,h,j,l: phase ϕ. Wavenumbers and frequencies of waves are marked by triangles of fig. 4.14 as follows: a,b: triangle 1. c,d: triangle 2. e,f: triangle 3. g,h: triangle 4. i,j: triangle 5. k,l: triangle 6.

Nevertheless, shore-trapped waves were indeed an order of magnitude larger than bar-trapped waves at $(\omega, k) = (0.09096 \text{ Hz}, 0.0236 \text{ m}^{-1})$. Generally, whenever eq. (4.30) predicts that the indirectly-forced wave is much larger than the directly-forced wave, the time scale for dissipation is much longer than the time scale for energy exchange between bar- and shore-trapped waves, and separated resonance curves similar to the ones shown in fig. 4.16 are expected.

For the beach considered above, coupling between bar- and shore-trapped waves was so weak (Q was 6×10^3 for the waves of fig.'s 4.16 & 4.17) that they would almost certainly have been decoupled in the field. If the bar had been closer to the shore, or the trough had been shallower, or the wave frequency had been lower, then decoupling would not have been so certain (eq. (4.30)).

Mode coupling, of which coupling between shore- and bar-trapped waves is an example, occurs in many branches of physics. Coupling between free, non-dissipative modes has received a great deal of attention (eg. Eckart (1961) considered coupling between internal waves on two separate pycnoclines, Parrish and Niiler (1971) considered coupling between surface and internal waves over the shelf break, Louisell (1960) considered coupled electrical circuits, and Flynn and Littlejohn (1994) considered coupling in quantum mechanics). Coupling between dissipative modes has received much less attention, although Garrett (1969) pointed out that dissipation might decouple free modes in the atmosphere (we have considered forced modes), and Grimshaw and Allen (1982) examined the effects of dissipation on coupled unforced modes in a slowly-varying medium.

4.3.4 Realistic forcing and dissipation

So far, I have presented only point-forced waves, and have assumed that the dissipation factor λ is constant. This Section presents simulations of wave fields generated by more realistic, distributed forcing in the presence of spatially-varying dissipation. These simulations are of waves on the barred beach shown in fig. 4.10.

A standard bottom friction parameterisation (Section 2.4) suggests

$$\lambda = C|\boldsymbol{u}|/h, \tag{4.31}$$

where $|\boldsymbol{u}|$ is a typical water speed, and C is a constant, here assumed to be 10^{-2}. To simulate dissipation when incident waves were small (large), I assume $|\boldsymbol{u}| = 0.3$ ms^{-1} ($|\boldsymbol{u}| = 1$ ms^{-1}). Equation (4.31) fails at the shore, since λ tends to infinity as the depth tends to zero. Miles (1990) showed that, in the absence of capillary forces, eq. (4.31) incorrectly predicts total absorption (zero reflection) of linear waves at the shore. To avoid this problem, I arbitrarily set all values of λ shoreward of $h = 0.5$ m equal to $C|\boldsymbol{u}|/(0.5$ m). I divided the region seaward of $h = 0.5$ m into a series of segments, each 10 m wide, and calculated one value of λ for each segment using the local mean depth and eq. (4.31).

Forcing is due to wave groups with frequency ω and wavenumber k, which are produced by interference between two sinusoidal wave trains with frequencies ω_s and $\omega_s + \omega$, and longshore wavenumbers k_s and $k_s + k$. Spectral forcing could be represented by simply summing over all such wave groups, but this Section presents simulations for only two infragravity frequencies (0.017 Hz and 0.037 Hz) and a single longshore infragravity wavenumber (0.005 m^{-1}). Only the case $\omega_s = 2\pi/(10\ s)$, $k_s = -k/2$ is considered. The complex amplitudes a_{s1} and a_{s2} of the two wave trains are calculated by assuming linear, non-dissipative, WKB shoaling of shoreward-propagating waves over a longshore-uniform beach (giving eq.(2) of Guza and Bowen (1976b), with $r = 0$, for each velocity potential). The assumptions of zero reflection and zero dissipation are inconsistent. Consequently, the complex amplitude of group-frequency energy fluctuations ($a_G^{(1)} = g a_{s1} a_{s2}^*$) tends to infinity as groups approach the shore. During storms, breaking dissipates wave energy, and destroys wave groups as they approach the shore (Symonds *et al.*, 1982; List, 1991). Breaking is simulated by assuming

$$a_G(x) = \frac{1 + \tanh[\zeta(x - x_b)]}{2} a_G^{(1)}(x), \tag{4.32}$$

where $a_G(x)$ is the amplitude of group-frequency energy fluctuations in the presence of breaking. The constants x_b and ζ determine respectively the location of the outer edge of the surf zone, and the width of the region over which wave groups are destroyed. When

incident waves are very small they do not break, but we can not set $a_G = a_G^{(1)}$ at the shore, since this would give infinite forcing. To simulate small non-breaking waves, we set $a_G = a_G^{(1)}$ in water depths greater than 30 cm, and simply ignore forcing in water depths less than 30 cm. The amplitude a_G was substituted into energy-based formulas for the Stokes drift and radiation stress (Whitham, 1962), and the nonlinear forcing $\hat{F}$ was then calculated from eq. (4.15).

The above method for calculating the cross-shore structure of surf beat forcing relies on many dubious assumptions. Linear shoaling neglects nonlinear triad interactions, which transfer energy to harmonics of the primary incident frequencies (Freilich and Guza, 1984; Elgar and Guza, 1985a, 1985b). The longshore wavenumber of linear waves is conserved during shoaling over a longshore-uniform beach, but in the field the longshore wavenumber of breaking waves is not conserved, for reasons that are not understood (Herbers *et al.*, 1999). In the absence of field-tested models for the destruction of wave groups by breaking, I arbitrarily assumed that wave group destruction could be represented by the simple tanh window of eq. (4.32). I have ignored forcing by unbroken incident waves in very shallow water, as well as reflection of unbroken waves from the shore. Due these shortcomings, only the gross features of the model predictions are significant.

When incident waves are very small, groups propagate into very shallow water, and even those edge waves that are trapped very close to the shore are excited. Figure 4.18 shows that very low frequency (0.017 Hz) groups of small unbroken incident waves generated a strongly-resonant, cross-shore standing, mode zero edge wave. Figure 4.19 shows that higher frequency (0.037 Hz) groups of unbroken waves generated a strongly-resonant, cross-shore standing, mode five edge wave.

When incident waves are large, breaking destroys wave groups far offshore, and those edge waves that are trapped very close to the shore not excited. Figure 4.20 shows that, when incident waves broke far offshore, very low frequency (0.017 Hz) groups did not excite an energetic edge wave, even though forcing resonated with a mode zero edge wave (cf. fig. 4.18). Instead, only evanescent waves were generated. These evanescent waves propagated shorewards with the short-wave groups, and the associated sea level fluctuations were

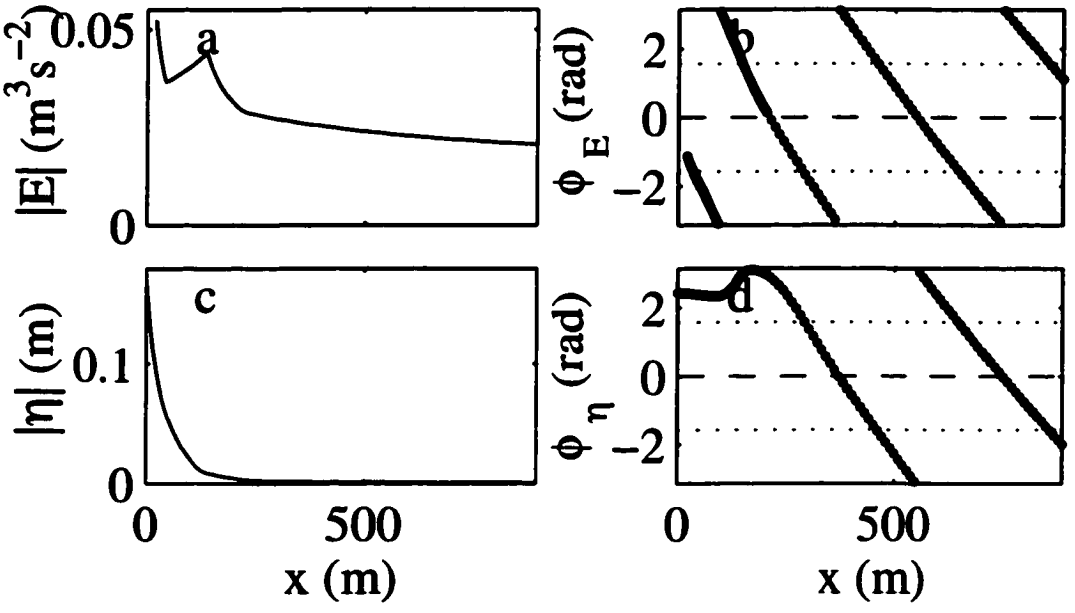

Figure 4.18: Low frequency (0.017 Hz) groups of non-breaking incident waves (a,b), and associated infragravity waves (c,d). a,c: Magnitude. b,c: Phase.

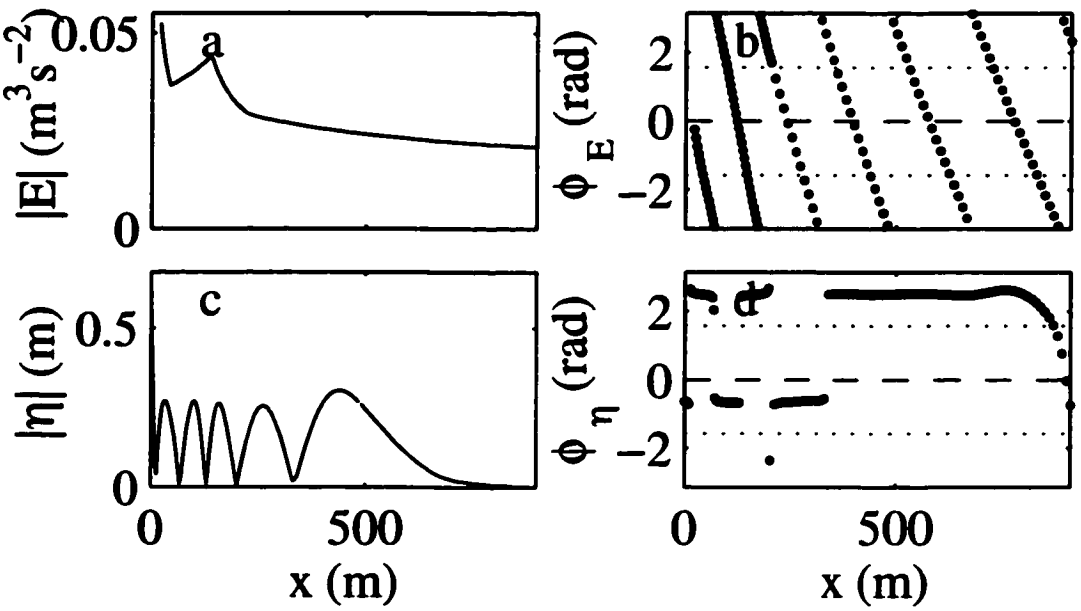

Figure 4.19: High frequency (0.037 Hz) groups of non-breaking incident waves (a,b), and associated infragravity waves (c,d). a,c: Magnitude. b,c: Phase.

180 degrees out of phase with co-located fluctuations in short-wave energy. In this regard, these waves were similar to the bound waves described by Longuet-Higgins and Stewart (1962), so we call them 'evanescent bound waves'. However, evanescent waves do not propagate freely across-shore (Section 4.3.2). Instead, the shoreward propagation evident in fig. 4.20d was entirely due to the shoreward propagation of the short-wave groups. This is most obvious at about $x = 400$ m, where short-wave groups were destroyed by breaking. Whereas Longuet-Higgins and Stewart (1962) suggested that bound waves are released when short waves break, the simulated evanescent bound waves simply disappeared.

Evanescent bound waves propagate shorewards, and carry a shoreward energy flux. Associated with the loss of evanescent bound wave energy at the breakpoint is a loss of the shoreward energy flux carried by evanescent waves. Section 3.4 showed that marked reductions in the shoreward energy flux carried by low frequency surf beat often accompanied wave breaking in the field. The observed loss of surf beat energy at the breakpoint might have been due to the presence of evanescent bound waves. However, marked reductions in the energy flux carried by relatively high frequency surf beat were not usually observed, and further field observations will be required to determine the importance of evanescent bound waves.

Infragravity energy was lost near the breakpoint, as shown in fig. 4.20c, because the breakpoint was outside the turning point and bound waves were evanescent. Figure 4.21 shows the response to higher frequency (0.037 Hz) forcing, which resonates with a much higher mode number ($n = 5$) edge wave. Now the turning point is seaward of the breakpoint, and energetic edge waves propagate shorewards, radiating energy away from the breakpoint. Outside the edge wave turning point, shoreward-propagating evanescent bound waves can still be seen.

Forcing with a frequency greater than $(gk)^{1/2}$ generates leaky waves. These leaky waves have no turning point, and always radiate energy away from the breakpoint. The bound wave model of Longuet-Higgins and Stewart (1962) assumes that waves are unidirectional ($k = 0$). Consequently, the bound waves simulated by Longuet-Higgins and Stewart are not evanescent, and always radiate energy away from the breakpoint. The

model of Hasselmann *et al.* (1963) does simulate evanescent bound waves, but forcing is assumed to be homogeneous, so evanescence has no striking effect.

4.4 Comment on normal modes

I have used Green's functions to solve the dissipative edge wave problem. I could also have used normal modes, by extending previous analysis (eg. Bowen and Guza (1978), Lippmann *et al.* (1997)) to allow for strong dissipation. Normal modes have the advantage that they provide very simple expressions for the amplitude and cross-shore structure of high Q edge waves. I discuss the representation of forced, dissipative edge waves by normal modes in Appendix F. I chose not to base this chapter on normal mode theories for two reasons. Firstly, the use of normal modes complicates the discussion of cross-shore propagation, evanescence and dissipative decoupling, all of which are associated with coherence between normal modes (Appendix F). Secondly, I do not know how to calculate normal modes for complex profiles of water depth and dissipation strength without resorting to numerical methods.

4.5 Discussion and conclusions

Field observations show that much infragravity energy exists in the form of shoreward-propagating waves (Chapters 2 and 3). This chapter has shown that shoreward propagation can be simulated using a dissipative shallow water model. This dissipative model predicts several additional phenomena that might be important to surf beat dynamics, such as non-resonant edge waves, evanescent bound waves, and dissipative decoupling. However, given the current lack of understanding of both incident wave breaking and infragravity wave dissipation, field observations will be required to test whether these phenomena are in fact important on natural beaches.

Strongly-dissipative edge waves propagate obliquely across-shore, carrying energy from regions of forcing to regions of dissipation. If forcing is weaker than dissipation

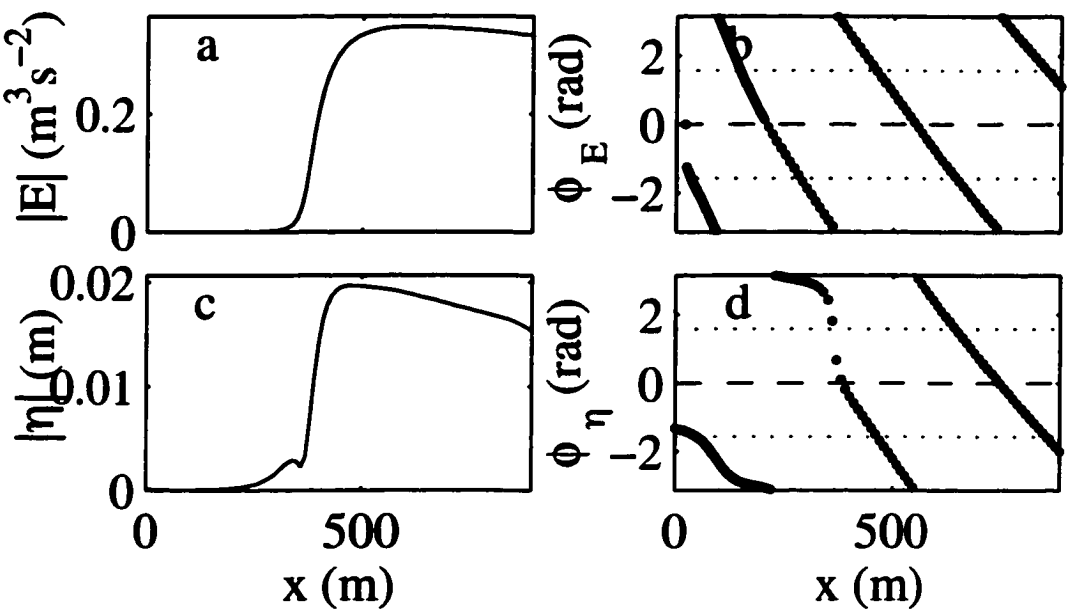

Figure 4.20: Low frequency (0.017 Hz) groups of breaking incident waves (a,b), and associated infragravity waves (c,d). a,c: Magnitude. b,c: Phase.

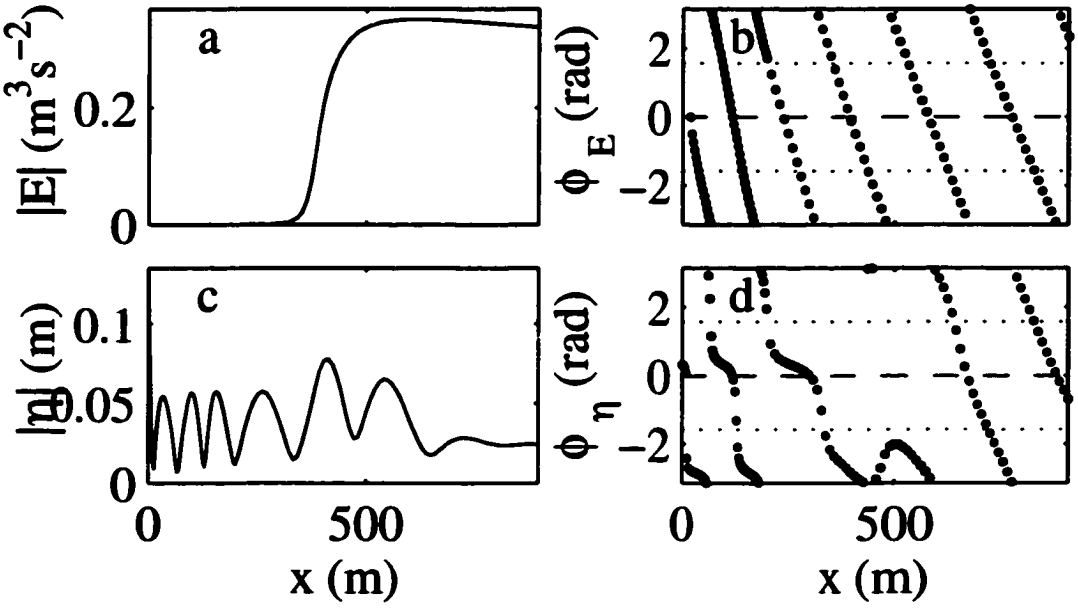

Figure 4.21: High frequency (0.017 Hz) groups of breaking incident waves (a,b), and associated infragravity waves (c,d). a,c: Magnitude. b,c: Phase.

inside the surf zone, then edge waves propagate shorewards into the surf zone. Outside the edge wave turning point, wave groups generate evanescent bound waves, which propagate shorewards with the wave groups. I suggest that the shoreward-propagating surf beat observed near the surf zone on natural beaches might be comprised of dissipative edge waves or evanescent bound waves. In contrast to the bound waves of Longuet-Higgins and Stewart (1962), whose energy radiates freely away from the breakpoint, evanescent bound waves simply disappear near the breakpoint. Therefore, field evidence for the existence of evanescent bound waves might include a major reduction in the shoreward energy flux near the edge of the surf zone. Field observations of such a reduction in the shoreward energy flux were presented in Section 3.4, although further evidence will be required before solid conclusions can be drawn. Field evidence for the existence of shoreward-propagating edge waves might include observations of shoreward-propagating waves with edge-wave frequencies and longshore wavenumbers inside the edge wave turning point.

Dissipation can decouple bar- and shore-trapped waves. Consequently, forcing over the sandbar can generate bar-trapped waves without generating shore-trapped waves. Similarly, forcing over the shoreface can generate shore-trapped waves without generating bar-trapped waves.

Chapter 5

Conclusions

5.1 Summary

This thesis has investigated the effects of forcing and dissipation on surf beat behaviour. Field observations have shown that, when incident waves are large, rapid damping of infragravity waves in the surf zone leads to net shoreward infragravity wave propagation. When incident waves are small, net infragravity wave damping is relatively weak, and infragravity waves are almost cross-shore standing.

A model of dissipative, shore-oblique shallow water waves suggests that the observed shoreward-propagating infragravity waves could be either dissipative edge waves or evanescent bound waves. When dissipation is very weak, forcing close to the shore generates cross-shore standing edge waves. Stronger dissipation introduces edge waves that progress obliquely across-shore, carrying energy from regions of forcing to regions of dissipation. Evanescent waves, which decay almost exponentially away from regions of forcing, dominate over resonant edge waves when forcing is applied sufficiently far outside the edge wave turning point. Group-bound evanescent waves propagate shorewards with short-wave groups and remain about 180 degrees out of phase with co-located short-wave energy but, unlike the group-bound waves described by previous researchers, they simply disappear when short waves break. In the field, marked reductions in the shoreward energy flux carried by low frequency surf beat often accompanied wave breaking, suggesting

that evanescent bound waves were present. However, this result is not conclusive, and shoreward energy fluxes associated with relatively high frequency surf beat did not usually decrease greatly in the outer surf zone. Leaky waves can also propagate shorewards, but observations of oblique shoreward propagation reported by Sheremet *et al.* (2001) seem to rule out leaky waves as the main source of shoreward-propagating infragravity energy.

Model results suggest that dissipation might decouple bar- and shore-trapped waves. Decoupling is strongest when the trough between the shore and the bar is wide and deep.

5.2 Possible future research

I have not identified the mechanism responsible for the strong surf beat damping observed during storms. Possible mechanisms include bottom friction, breaking, and nonlinear damping. Three-dimensional flow structure could also lead to shear-dispersive mixing (Svendsen and Putrevu, 1994; Van Dongeren *et al.*, 1998). Longuet-Higgins (1967) showed that the time scale for dissipation in a wave bottom boundary layer with constant eddy viscosity is $O(h/h_\delta)$ wave periods, where h is the water depth and h_δ is the boundary layer thickness. I expect that a similar result holds when the eddy viscosity is not constant. If so, then measurements of the thickness of the surf beat bottom boundary layer might be used to determine whether bottom friction is responsible for much of the observed surf beat energy loss. The importance of nonlinear damping could be estimated by direct evaluation of the nonlinear terms in the energy equation (2.11), using measured water pressures and velocities and the nonlinear spectral techniques described in Appendix B. Estimation of the roller contributions to wave momentum (eq. (2.18)) and momentum flux (eq. (2.17)) would be difficult. Dense arrays of instruments would be required to resolve spatial gradients of the momentum flux.

Observations from longshore arrays of current meters or pressure gauges could be used to distinguish between edge and evanescent waves. The proportion of energy carried by

evanescent waves could be determined from such data using the 'direct estimator' of Elgar *et al.* (1994) (evanescent waves have wavenumbers greater than $\omega/(gh)^{1/2}$). Band-integrated cross-spectra could be estimated using a generalisation of the direct estimator, so that shoreward energy fluxes carried by evanescent waves might also be calculated. To measure evanescent bound waves, longshore arrays should be located near the outer edge of surf zone. Evanescent waves are most likely to be found when the height and directional spread of incident waves are both large. The loss of evanescent wave energy in the outer surf zone is associated with rapid nonlinear surf beat damping in the outer surf zone. Therefore, if evanescent waves are energetic, then direct evaluation of the nonlinear terms in the energy equation, as outlined in the previous paragraph, should show strong nonlinear damping in the outer surf zone.

Predictions of dissipative decoupling of bar- and shore-trapped waves might be tested by comparing waves observed near the shore with waves observed over a well-developed bar. Observations of coherence and relative energy levels might be particularly useful. However, interpretation of coherence between bar- and shore-trapped waves would require care, because forcing over the bar might be coherent with forcing near the shore.

Observed surf beat energy levels do not decay seawards at the rate predicted by free wave theories (Ruessink, 1998b; Lippmann *et al.*, 1998, 2001). Chapter 4 showed that forcing and dissipation modify the cross-shore structure of surf beat. It would be interesting to see whether the cross-shore variation in surf beat energy levels can be predicted by a simple dissipative model.

Thorough calibration and testing of a dissipative surf beat model would be valuable. Such calibration might improve our understanding of surf beat dissipation. Furthermore, calibration of a dissipative model would be an important step towards the ultimate goal of predicting the infragravity wave field from the incident wave field. Existing models of shoaling incident waves seriously underpredict the directional spread of incident waves, and therefore the longshore wavenumbers at which surf beat is forced. The longshore structure of surf beat forcing is important, since it determines whether leaky, edge, or evanescent

waves are forced. Therefore, accurate simulation of surf beat will require either direct evaluation of nonlinear forcing from field data, or improved models of incident waves.

Appendix A

Derivation of a nonlinear frequency-domain energy equation

A.1 Mass and momentum conservation

An exact, depth-integrated momentum equation for waves in water of constant density and arbitrary depth is (eq. 3.6.7 of Phillips (1977))

$$\frac{\partial}{\partial t}\int_{-h}^{\eta} u_j\,dz + \frac{\partial}{\partial x_k}\int_{-h}^{\eta} u_j u_k\,dz + \frac{\partial}{\partial x_j}\int_{-h}^{\eta}\frac{p}{\varrho}\,dz - \frac{p}{\varrho}\frac{\partial h}{\partial x_j} = 0, \tag{A.1}$$

$$\Rightarrow \int_{-h}^{0}\frac{\partial u_j}{\partial t}\,dz + \int_{-h}^{0}\frac{\partial (p/\varrho)}{\partial x_j}\,dz + \frac{\partial T_{j,k}}{\partial x_k} + \frac{\partial M_j}{\partial t} = 0, \tag{A.2}$$

where T and $\boldsymbol{M}$ are defined by eq.'s (2.17) & (2.18), p = water pressure, and ϱ = water density.

Equation (A.2) can be rewritten using the Fourier components defined by eq.'s (2.8) & (2.10):

$$\int_{-h}^{0}\left\langle\frac{\partial u_j}{\partial t}\right\rangle_{\omega} dz + \frac{1}{\varrho}\int_{-h}^{0}\frac{\partial \langle p\rangle_{\omega}}{\partial x_j}\,dz + \frac{\partial \langle T_{j,k}\rangle_{\omega}}{\partial x_k} + \left\langle\frac{\partial M_j}{\partial t}\right\rangle_{\omega} = 0. \tag{A.3}$$

I approximate the motion at frequency ω by assuming

$$\langle p\rangle_{\omega} = \varrho g \langle \eta\rangle_{\omega}, \tag{A.4}$$

$$\langle u_j\rangle_{\omega} \text{ is independent of } z. \tag{A.5}$$

Equations (A.4) & (A.5) are correct to leading order if frequency ω waves satisfy the Boussinesq assumptions, and are exact in the shallow water limit.

In reality, $\langle p \rangle_\omega$ depends in part on fluxes of vertical momentum. The effects of these momentum fluxes are are usually incorporated into the radiation stress, but have been neglected in eq. (A.4). Longuet-Higgins and Stewart (1964) divided the normal radiation stress $S_{x,x}$ into three components, $S^{(1)}_{x,x}$, $S^{(2)}_{x,x}$, and $S^{(3)}_{x,x}$ (their eq.(9)). I have included $S^{(1)}_{x,x}$ and $S^{(3)}_{x,x}$ in $T_{x,x}$ but, through eq. (A.4), have neglected the pressure-deficit term $S^{(2)}_{x,x}$. From linear theory, the ratio between the neglected and retained radiation stress terms for long wave groups is

$$\mu \equiv \left| \frac{S^{(2)}_{x,x}}{S^{(1)}_{x,x} + S^{(3)}_{x,x}} \right| = \frac{1 - 2|\boldsymbol{k}|h/\sinh(2|\boldsymbol{k}|h)}{2 + 2|\boldsymbol{k}|h/\sinh(2|\boldsymbol{k}|h)}, \tag{A.6}$$

where $\boldsymbol{k}$ is the wavenumber vector of the waves generating the radiation stress. Figure A.1 shows how μ varies with wave period and water depth. During Sandyduck, peak periods were usually 7-13 s, and depths at the instrumented frames ranged from 1 m to 5 m. From fig. A.1, assumption (A.4) leads to errors of about 2–5% in radiation stress estimates. Usually $h|\langle p \rangle_\omega| > |\langle S_{x,x} \rangle_\omega|$, so the relative error in $|\langle p \rangle_\omega|$ estimates due to the neglected pressure deficit term was probably less than 5%.

Equation (A.5) neglects variations of $\langle u_j \rangle_\omega$ in the bottom boundary layer. I assume that the thickness of these boundary layers is much less than the water depth, so that the proportion of the depth-integrated momentum stored in the boundary layers is negligible.

From eq.'s (2.16), (A.3), (A.4) & (A.5)

$$h \left\langle \frac{\partial \tilde{u}_j}{\partial t} \right\rangle_\omega + gh \frac{\partial \langle \eta \rangle_\omega}{\partial x_j} + \frac{\partial \langle T_{j,k} \rangle_\omega}{\partial x_j} = 0. \tag{A.7}$$

Similarly, the exact depth-integrated mass conservation equation

$$\frac{\partial \eta}{\partial t} + \frac{\partial}{\partial x_k} \int_{-h}^{\eta} u_k \, dz = 0, \tag{A.8}$$

together with eq. (A.5), leads to

$$\left\langle \frac{\partial \eta}{\partial t} \right\rangle_\omega + \frac{\partial h \langle \tilde{u}_k \rangle_\omega}{\partial x_k} = 0. \tag{A.9}$$

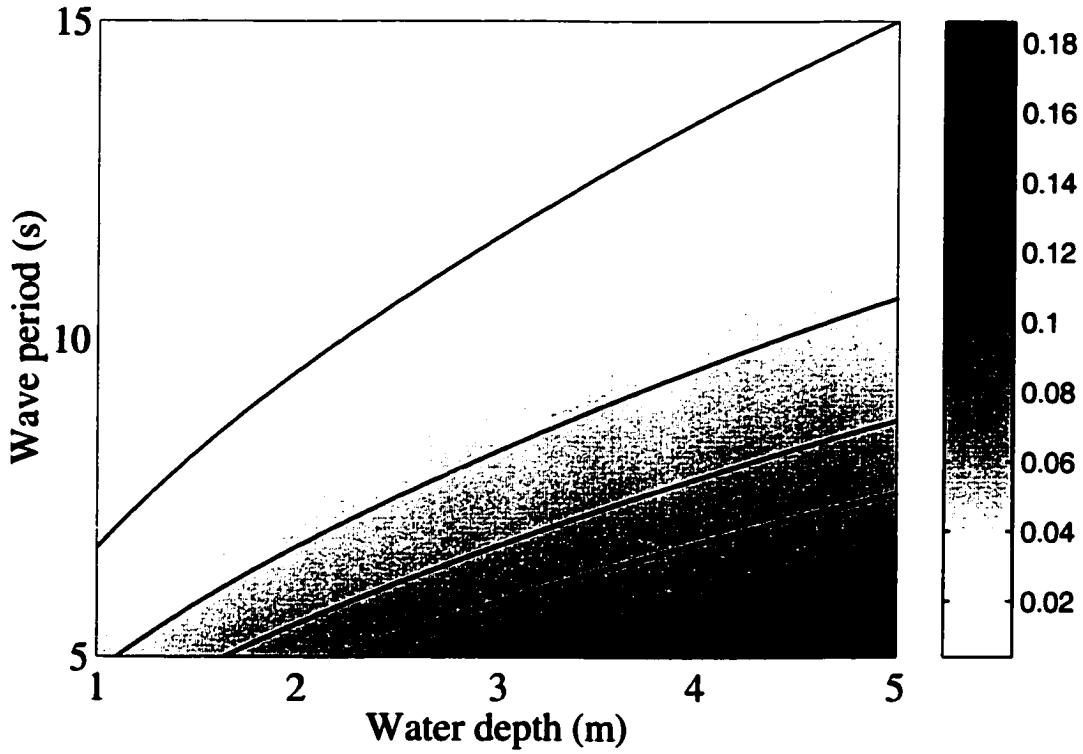

Figure A.1: Effect of water depth and wave period on the ratio μ between neglected and retained radiation stress components. Interval between contours is 0.02. Lowest contour is μ =0.02.

A.2 Fourier identity

This Section presents an identity that will be used in Section A.3. From eq. (2.8)

$$\frac{\partial X}{\partial t} = \frac{\partial}{\partial t} \sum_{j=-\infty}^{\infty} \mathrm{e}^{\mathrm{i}(j\,\Delta\omega)t} \langle X \rangle_{j\,\Delta\omega}\,, \tag{A.10}$$

so

$$\frac{\partial X}{\partial t} = \sum_{j=-\infty}^{\infty} \mathrm{e}^{\mathrm{i}(j\,\Delta\omega)t} \left[\mathrm{i}(j\,\Delta\omega) \langle X \rangle_{j\,\Delta\omega} + \frac{\partial \langle X \rangle_{j\,\Delta\omega}}{\partial t} \right]. \tag{A.11}$$

But, by definition

$$\frac{\partial X}{\partial t} = \sum_{j=-\infty}^{\infty} \mathrm{e}^{\mathrm{i}(j\,\Delta\omega)t} \left\langle \frac{\partial X}{\partial t} \right\rangle_{j\,\Delta\omega}, \tag{A.12}$$

so, from eq.'s (A.11) & (A.12)

$$\left\langle \frac{\partial X}{\partial t} \right\rangle_{\omega} = \mathrm{i}\omega \langle X \rangle_{\omega} + \frac{\partial \langle X \rangle_{\omega}}{\partial t}. \tag{A.13}$$

Now

$$\frac{\partial \langle X \rangle_{\omega} \langle X \rangle_{-\omega}}{\partial t} = \langle X \rangle_{\omega} \frac{\partial \langle X \rangle_{-\omega}}{\partial t} + \langle X \rangle_{-\omega} \frac{\partial \langle X \rangle_{\omega}}{\partial t}. \tag{A.14}$$

Combining eq.'s (A.13) & (A.14), and noting that $\langle X \rangle_{-\omega}$ is the complex conjugate of $\langle X \rangle_{\omega}$ for any real X, gives

$$\frac{\partial |\langle X \rangle_{\omega}|^2}{\partial t} = 2\Re \left[\langle X \rangle_{\omega} \left\langle \frac{\partial X}{\partial t} \right\rangle_{-\omega} \right]. \tag{A.15}$$

A.3 Energy equation

Adding $\langle \tilde{u}_j \rangle_{-\omega}$ ×eq. (A.7) to the complex conjugate of $\langle \tilde{u}_j \rangle_{-\omega}$ ×eq. (A.7) and applying eq. (A.15) gives

$$\frac{\partial h |\langle \tilde{\boldsymbol{u}} \rangle_{\omega}|^2}{\partial t} + 2\Re \left[gh \langle \tilde{u}_j \rangle_{-\omega} \frac{\partial \langle \eta \rangle_{\omega}}{\partial x_j} + \langle \tilde{u}_j \rangle_{-\omega} \frac{\partial \langle T_{j,k} \rangle_{\omega}}{\partial x_k} \right] = 0. \tag{A.16}$$

But

$$gh\,\langle\tilde{u}_j\rangle_{-\omega}\,\frac{\partial\langle\eta\rangle_\omega}{\partial x_j} = \frac{\partial gh\,\langle\tilde{u}_j\rangle_{-\omega}\,\langle\eta\rangle_\omega}{\partial x_j} - g\,\langle\eta\rangle_\omega\,\frac{\partial h\,\langle\tilde{u}_j\rangle_{-\omega}}{\partial x_j}, \tag{A.17}$$

so from eq.'s (A.9), (A.17) & (A.15)

$$2\Re\left[gh\,\langle\tilde{u}_j\rangle_{-\omega}\,\frac{\partial\langle\eta\rangle_\omega}{\partial x_j}\right] = 2\Re\left[\frac{\partial hg\,\langle\eta\rangle_\omega\,\langle\tilde{u}_j\rangle_{-\omega}}{\partial x_j}\right] + \frac{\partial g|\,\langle\eta\rangle_\omega\,|^2}{\partial t}. \tag{A.18}$$

Substituting eq. (A.18) into eq. (A.16) gives

$$\frac{\partial\mathcal{E}_{nl}}{\partial t} + \frac{\partial w_j}{\partial x_j} + \mathcal{F} = 0, \tag{A.19}$$

where $\mathcal{E}_{nl}$, w_j, and $\mathcal{F}$ are defined by eq.'s (2.12)–(2.14).

Finally, adding to eq. (A.19) a term $\mathcal{D}$ to represent the effects of dissipation gives eq. (2.11).

Appendix B

Nonlinear coupling and higher order spectra

Let X_1, X_2, X_3, and X_4 be continuous stationary time series (most results of this section also hold for regularly sampled discrete time series). Let the time series length Δt in eq.'s (2.8) & (2.10) tend to infinity, so $\Delta\omega$ is replaced by the infinitesimal $d\omega$, and the series of eq. (2.8) is replaced by the Fourier-Stieltjes integral

$$X_n = \int_{\omega=-\infty}^{\infty} e^{i\omega t} \langle X_n \rangle_\omega . \tag{B.1}$$

For non-zero frequencies, the cross-spectral density $\Phi_{\omega_1}(X_1, X_2)$, the bispectral density $\Phi_{\omega_1,\omega_2}(X_1, X_2, X_3)$, and the trispectral density $\Phi_{\omega_1,\omega_2,\omega_3}(X_1, X_2, X_3, X_4)$ are defined by (Priestley, 1988)

$$E[\langle X_1 \rangle_{\omega_1} \langle X_2 \rangle_{\omega_2}]/d\omega = \begin{cases} \Phi_{\omega_1}(X_1, X_2) & \omega_1 + \omega_2 = 0 \\ 0 & \text{otherwise} \end{cases} , \tag{B.2}$$

$$E[\langle X_1 \rangle_{\omega_1} \langle X_2 \rangle_{\omega_2} \langle X_3 \rangle_{\omega_3}]/(d\omega)^2 = \begin{cases} \Phi_{\omega_1,\omega_2}(X_1, X_2, X_3) & \omega_1 + \omega_2 + \omega_3 = 0 \\ 0 & \text{otherwise} \end{cases} , \tag{B.3}$$

and

$$E[\langle X_1\rangle_{\omega_1}\langle X_2\rangle_{\omega_2}\langle X_2\rangle_{\omega_3}\langle X_4\rangle_{\omega_4}]/(d\omega)^3 =$$

$$\begin{cases} \Phi_{\omega_1,\omega_2,\omega_3}(X_1,X_2,X_3,X_4) & \\ +\Phi_{\omega_1}(X_1,X_2)\Phi_{\omega_3}(X_3,X_4)\delta(\omega_1+\omega_2) & \omega_1+\omega_2+\omega_3+\omega_4=0 \\ +\Phi_{\omega_1}(X_1,X_3)\Phi_{\omega_2}(X_2,X_4)\delta(\omega_1+\omega_3) & \\ +\Phi_{\omega_1}(X_1,X_4)\Phi_{\omega_2}(X_2,X_3)\delta(\omega_1+\omega_4) & \\ 0 & \text{otherwise} \end{cases} . \quad \text{(B.4)}$$

The Stokes Drift $\boldsymbol{M}$ and the radiation stress S both involve products of pairs of unknowns. Consequently, we are interested in the frequency-domain representation of such products. Let X_nX_m be the time series obtained by multiplying X_n by X_m. The Fourier coefficients of X_nX_m are

$$\langle X_nX_m\rangle_\omega = \int_{\omega_1}\langle X_n\rangle_{\omega_1}\langle X_m\rangle_{\omega-\omega_1}. \quad \text{(B.5)}$$

The energy equation (2.11) involves products such as $\langle u_j\rangle_\omega\,\partial\langle S_{j,k}\rangle_{-\omega}/\partial x_k$ and $\nabla\cdot(g\langle\eta\rangle_\omega\boldsymbol{M}_{-\omega})$, so the mean values of such products represent mean energy exchanges and are given by cross-spectra of the form

$$\Phi_\omega(X_1,X_2X_3) = E[\langle X_1\rangle_\omega\langle X_2X_3\rangle_{-\omega}]/d\omega. \quad \text{(B.6)}$$

From eq.'s(B.5)&(B.6)

$$\Phi_\omega(X_1,X_2X_3) = \int_{\omega_1} E\left[\frac{\langle X_1\rangle_\omega\langle X_2\rangle_{\omega_1}\langle X_3\rangle_{-\omega-\omega_1}}{d\omega\,d\omega_1}\right]d\omega_1, \quad \text{(B.7)}$$

$$\Rightarrow \Phi_\omega(X_1,X_2X_3) = \int_{\omega_1}\Phi_{\omega,\omega_1}(X_1,X_2,X_3)\,d\omega_1, \quad \text{(B.8)}$$

(see also Yeh and Van Atta (1973) and Tugnait (1994)). Consequently, mean energy exchanges can be represented either as cross-spectra involving nonlinear products, such as $\Phi_\omega(u_j,\partial S_{j,k}/\partial x_k)$, or as integrals of the bispectrum. Cross-spectra are easier to understand

and estimate, whereas bispectra can be used to determine exactly which triads are responsible for the energy exchange. Herbers and Burton (1997) and Herbers *et al.* (2000) used integrals of the bispectrum to represent energy exchanges between shoaling and breaking Boussinesq waves.

From eq. (B.6) and the preceding discussion, we see that there can be a mean nonlinear energy exchange to a wave of frequency ω only if the wave is coherent with nonlinear forcing. The coherence between a response X_1 and a nonlinear forcing term X_1^2 is

$$\kappa_\omega(X_1, X_1^2) = \frac{\Phi_\omega(X_1, X_1^2)}{[\Phi_\omega(X_1, X_1)\Phi_\omega(X_1^2, X_1^2)]^{1/2}}. \tag{B.9}$$

Coherence with nonlinear forcing is usually estimated only within a single time series, so I have chosen the forcing to be X_1^2 (rather than X_2X_3, which would be more general) to simplify the algebra which follows. Huntley and Kim (1984) used $|\kappa|^2$ to estimate the proportion of surf beat energy that was 'forced' (as opposed to 'free'). More recently, Herbers and Guza (1992), Herbers *et al.* (1994), and Ruessink (1998a) have estimated the proportion of energy that is forced as using the parameter

$$\kappa'_\omega(X_1, X_1^2) = \frac{\int_{\omega_1} \Phi_{\omega,\omega_1}(X_1, X_1, X_1)\, d\omega_1}{\left[2\Phi_\omega(X_1, X_1)\int_{\omega_1} \Phi_{\omega_1}(X_1, X_1)\Phi_{\omega-\omega_1}(X_1, X_1)\, d\omega_1\right]^{1/2}}. \tag{B.10}$$

If the trispectrum is large, then $|\kappa'|^2$ has no simple interpretation. I will conclude this appendix by showing that $\kappa' \approx \kappa$ if the trispectrum is sufficiently small. From eq.'s (B.8) & (B.10)

$$\kappa'_\omega(X_1, X_1^2) = \frac{\Phi_\omega(X_1, X_1^2)}{\left[2\Phi_\omega(X_1, X_1)\int_{\omega_1} \Phi_{\omega_1}(X_1, X_1)\Phi_{\omega-\omega_1}(X_1, X_1)\, d\omega_1\right]^{1/2}}. \tag{B.11}$$

It remains to show that the denominator of eq. (B.11) equals the denominator of eq. (B.9). For non-zero ω, the cross spectrum between X_1X_2 and X_3X_4 is

$$\Phi_\omega(X_1X_2, X_3X_4) = E[\langle X_1X_2\rangle_\omega \langle X_3X_4\rangle_{-\omega}]/d\omega. \tag{B.12}$$

From eq.'s(B.5)&(B.12),

$$\Phi_\omega(X_1X_2, X_3X_4) = \int_{\omega_1}\int_{\omega_2} E\left[\frac{\langle X_1\rangle_{\omega-\omega_1}\langle X_2\rangle_{\omega_1}\langle X_3\rangle_{\omega_2}\langle X_4\rangle_{-\omega-\omega_2}}{d\omega\, d\omega_1\, d\omega_2}\right] d\omega_1\, d\omega_2, \tag{B.13}$$

so, from eq.'s (B.4) & (B.13)

$$\Phi_\omega(X_1X_2, X_3X_4) =$$
$$\int_{\omega_1} [\Phi_{\omega_1}(X_1, X_3)\Phi_{\omega-\omega_1}(X_2, X_4) + \Phi_{\omega_1}(X_1, X_4)\Phi_{\omega-\omega_1}(X_2, X_3)]\, d\omega_1$$
$$+ \int_{\omega_1}\int_{\omega_2} \Phi_{\omega-\omega_1,\omega_1,\omega_2}(X_1, X_2, X_3, X_4)\, d\omega_1\, d\omega_2, \quad \text{(B.14)}$$

Therefore, if $\omega \neq 0$ and the trispectral density is zero, then (from eq. (B.14))

$$\Phi_\omega(X_1^2, X_1^2) = 2\int_{\omega_1} \Phi_{\omega_1}(X_1, X_1)\Phi_{\omega-\omega_1}(X_1, X_1)\, d\omega_1 \quad \text{(B.15)}$$

Substituting eq. (B.15) into eq. (B.11) leads to eq. (B.9).

Appendix C

Cross-shore profiles of surf beat energy density and energy flux

Section 3.4 presented typical cross-shore profiles of surf beat energy density and energy flux measured during the Duck94 experiment. Here the remainder of the profiles that satisfied the conditions outlined in Section 3.4 are presented in order of increasing incident wave height.

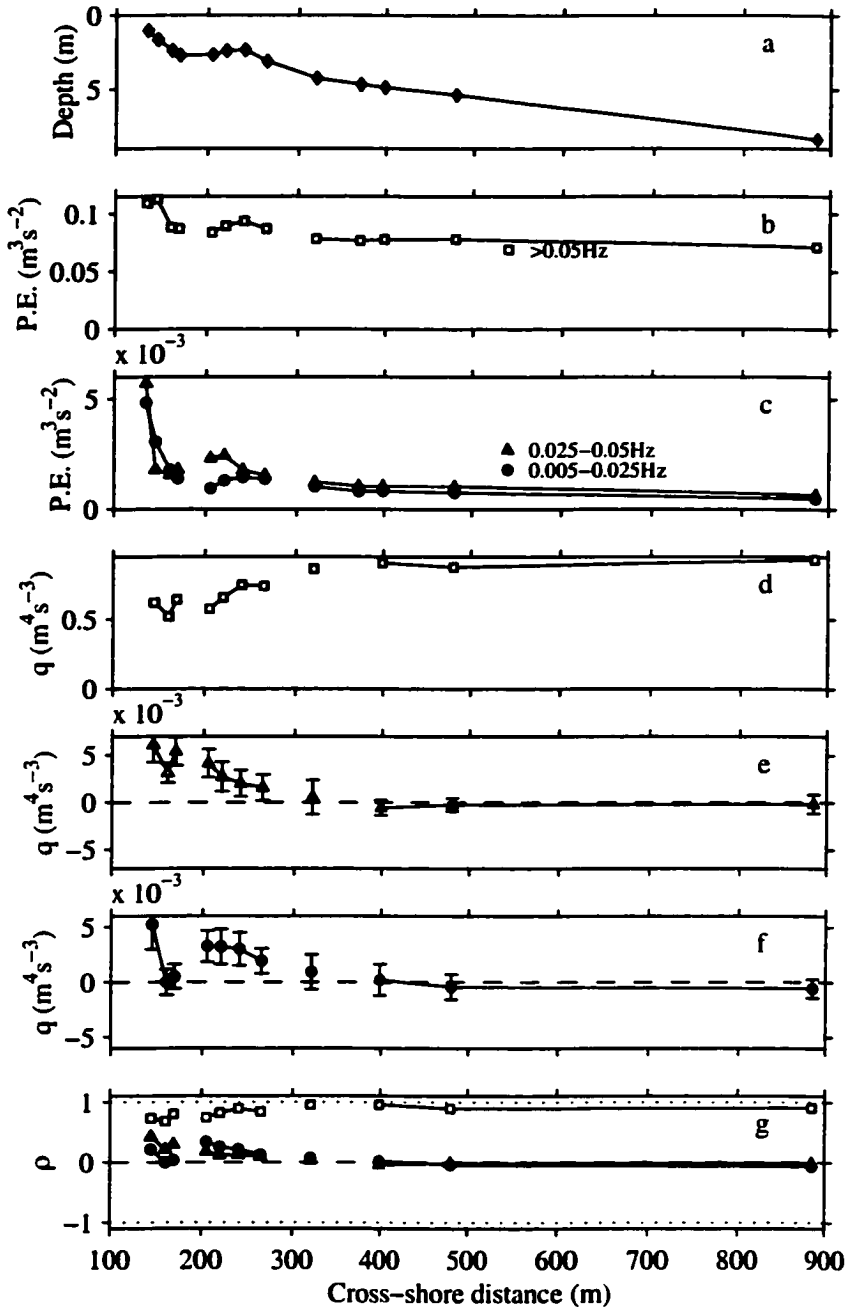

Figure C.1: Water depth (a), potential energy density $P.E.$ (b: swell. c: surf beat), shoreward energy flux q (d: swell. e: high frequency surf beat. f: low frequency surf beat), and progressiveness parameter ρ (g) *versus* cross-shore distance. Values estimated from 3 hr time series on September 28th, $Hs = 0.48$ m. Squares: Swell (> 0.05 Hz). Triangles: High frequency surf beat (0.025–0.05 Hz). Circles: Low frequency surf beat (0.005–0.025 Hz).

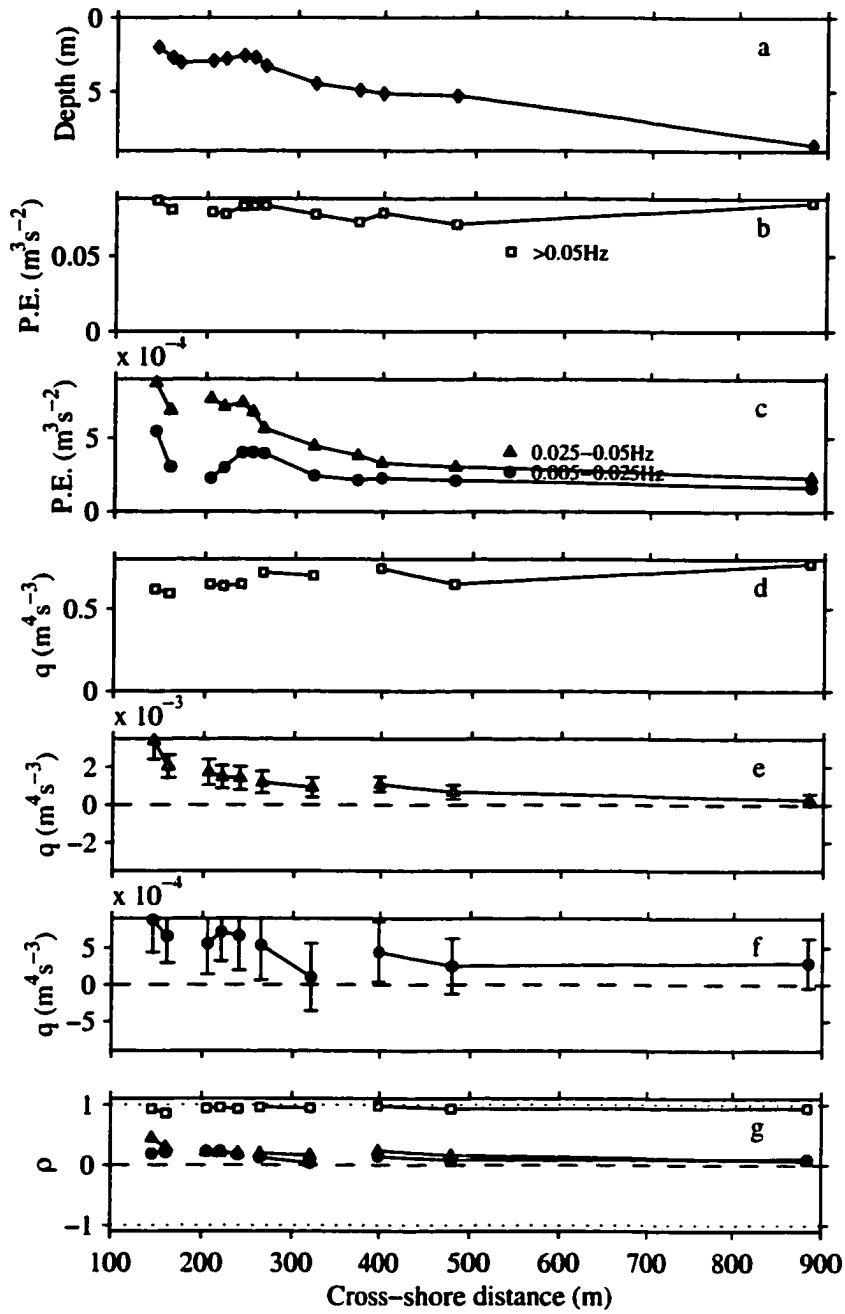

Figure C.2: Water depth (a), potential energy density $P.E.$ (b: swell. c: surf beat), shoreward energy flux q (d: swell. e: high frequency surf beat. f: low frequency surf beat), and progressiveness parameter ρ (g) *versus* cross-shore distance. Values estimated from 3 hr time series on October 8th, Hs = 0.55 m. Squares: Swell (> 0.05 Hz). Triangles: High frequency surf beat (0.025–0.05 Hz). Circles: Low frequency surf beat (0.005–0.025 Hz).

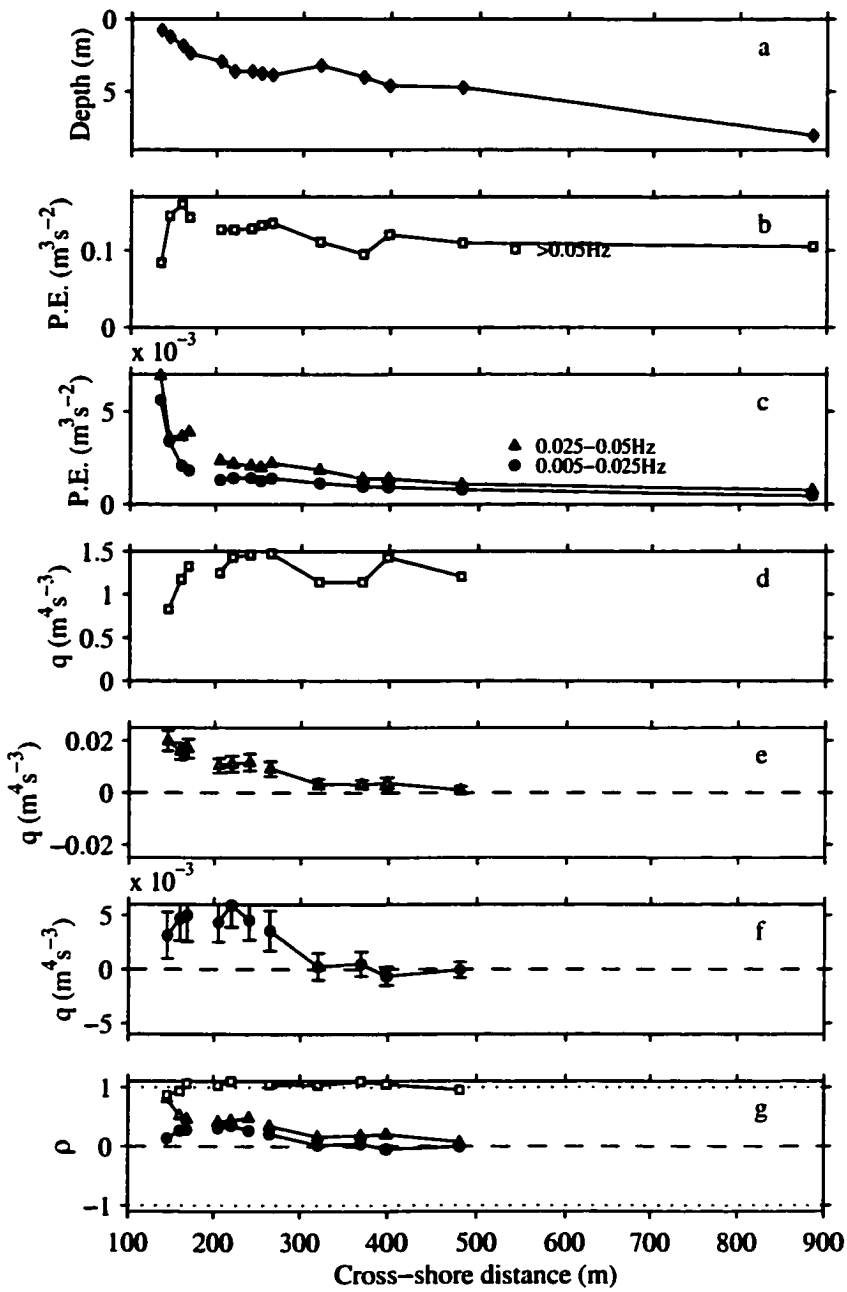

Figure C.3: Water depth (a), potential energy density $P.E.$ (b: swell. c: surf beat), shoreward energy flux q (d: swell. e: high frequency surf beat. f: low frequency surf beat), and progressiveness parameter ρ (g) *versus* cross-shore distance. Values estimated from 3 hr time series on October 29th, $Hs = 0.59$ m. Squares: Swell (> 0.05 Hz). Triangles: High frequency surf beat (0.025–0.05 Hz). Circles: Low frequency surf beat (0.005–0.025 Hz).

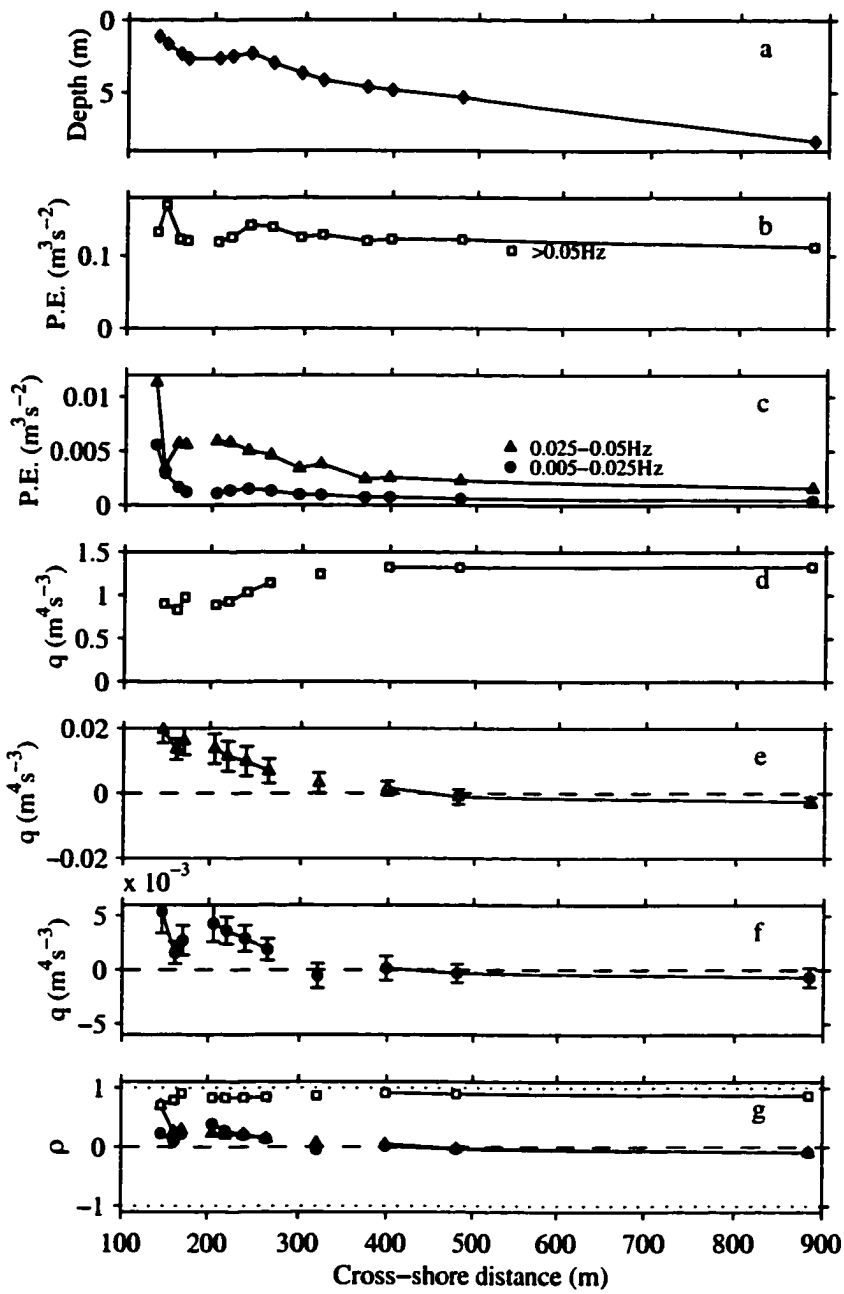

Figure C.4: Water depth (a), potential energy density $P.E.$ (b: swell. c: surf beat), shoreward energy flux q (d: swell. e: high frequency surf beat. f: low frequency surf beat), and progressiveness parameter ρ (g) *versus* cross-shore distance. Values estimated from 3 hr time series on September 24th, $Hs = 0.61$ m. Squares: Swell (> 0.05 Hz). Triangles: High frequency surf beat (0.025–0.05 Hz). Circles: Low frequency surf beat (0.005–0.025 Hz).

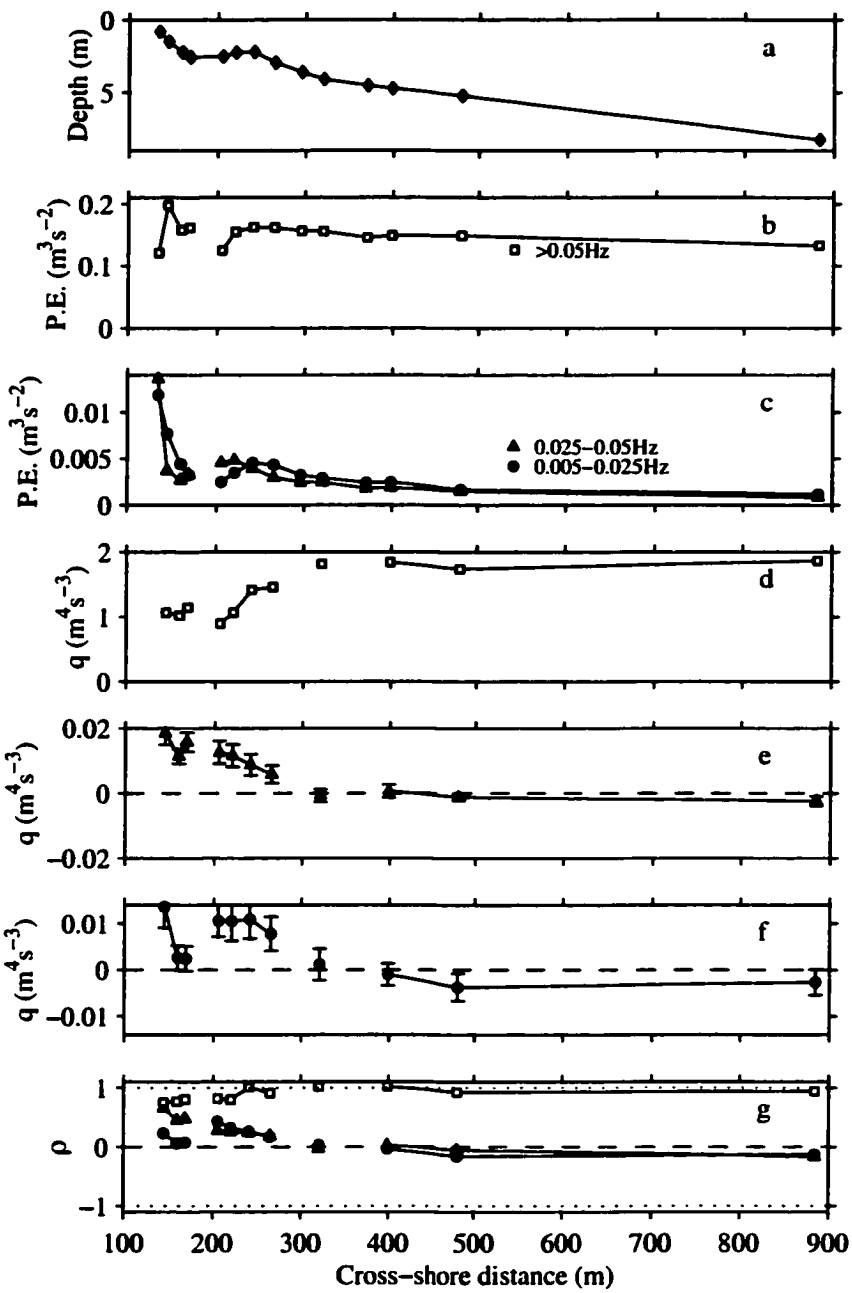

Figure C.5: Water depth (a), potential energy density $P.E.$ (b: swell. c: surf beat), shoreward energy flux q (d: swell. e: high frequency surf beat. f: low frequency surf beat), and progressiveness parameter ρ (g) *versus* cross-shore distance. Values estimated from 3 hr time series on September 27th (10 pm), $Hs = 0.66$ m. Squares: Swell (> 0.05 Hz). Triangles: High frequency surf beat (0.025–0.05 Hz). Circles: Low frequency surf beat (0.005–0.025 Hz).

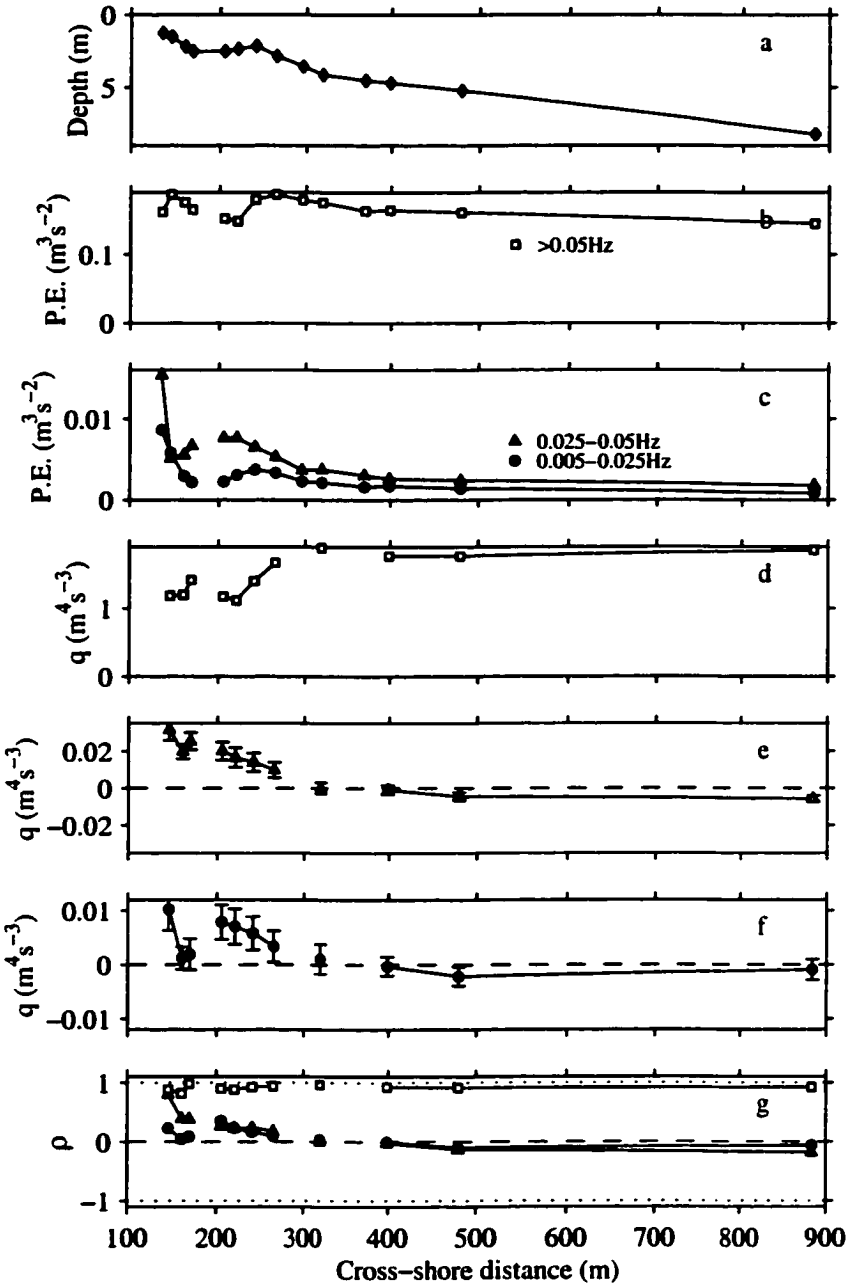

Figure C.6: Water depth (a), potential energy density $P.E.$ (b: swell. c: surf beat), shoreward energy flux q (d: swell. e: high frequency surf beat. f: low frequency surf beat), and progressiveness parameter ρ (g) *versus* cross-shore distance. Values estimated from 3 hr time series on September 24th, $Hs = 0.69$ m. Squares: Swell (> 0.05 Hz). Triangles: High frequency surf beat (0.025–0.05 Hz). Circles: Low frequency surf beat (0.005–0.025 Hz).

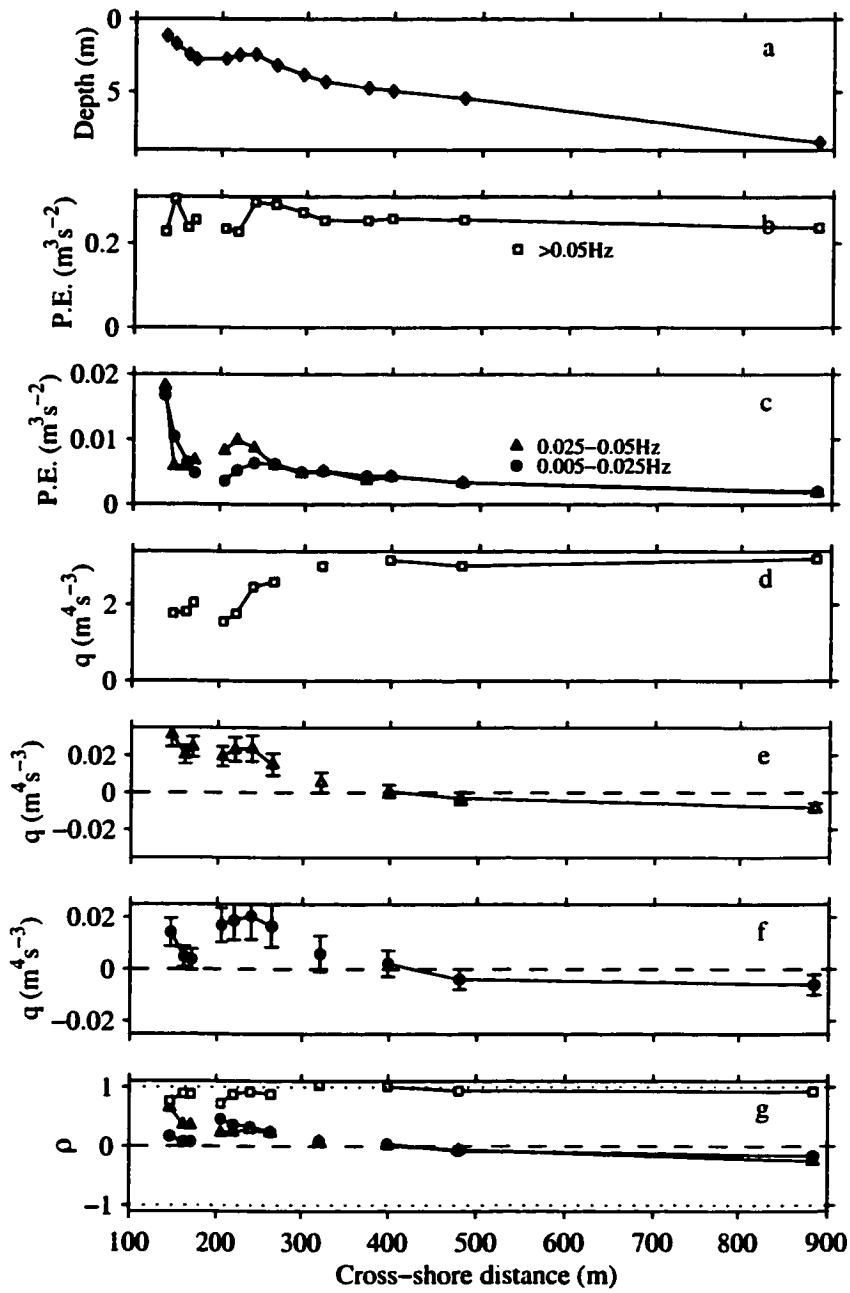

Figure C.7: Water depth (a), potential energy density $P.E.$ (b: swell. c: surf beat), shoreward energy flux q (d: swell. e: high frequency surf beat. f: low frequency surf beat), and progressiveness parameter ρ (g) *versus* cross-shore distance. Values estimated from 3 hr time series on September 27th (10 am), Hs = 0.88 m. Squares: Swell (> 0.05 Hz). Triangles: High frequency surf beat (0.025–0.05 Hz). Circles: Low frequency surf beat (0.005–0.025 Hz).

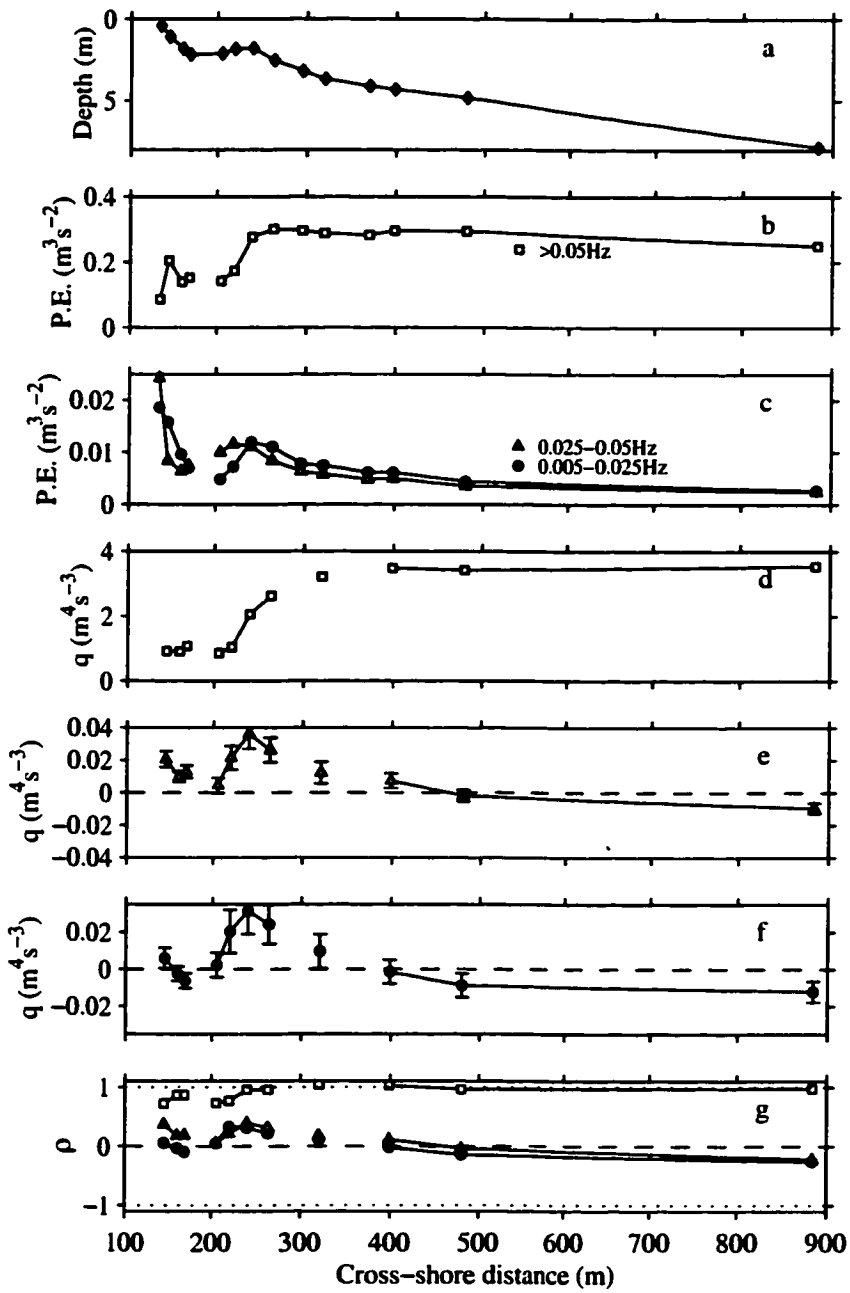

Figure C.8: Water depth (a), potential energy density $P.E.$ (b: swell. c: surf beat), shoreward energy flux q (d: swell. e: high frequency surf beat. f: low frequency surf beat), and progressiveness parameter ρ (g) *versus* cross-shore distance. Values estimated from 3 hr time series on September 27th (4 am), Hs = 0.9 m. Squares: Swell (> 0.05 Hz). Triangles: High frequency surf beat (0.025–0.05 Hz). Circles: Low frequency surf beat (0.005–0.025 Hz).

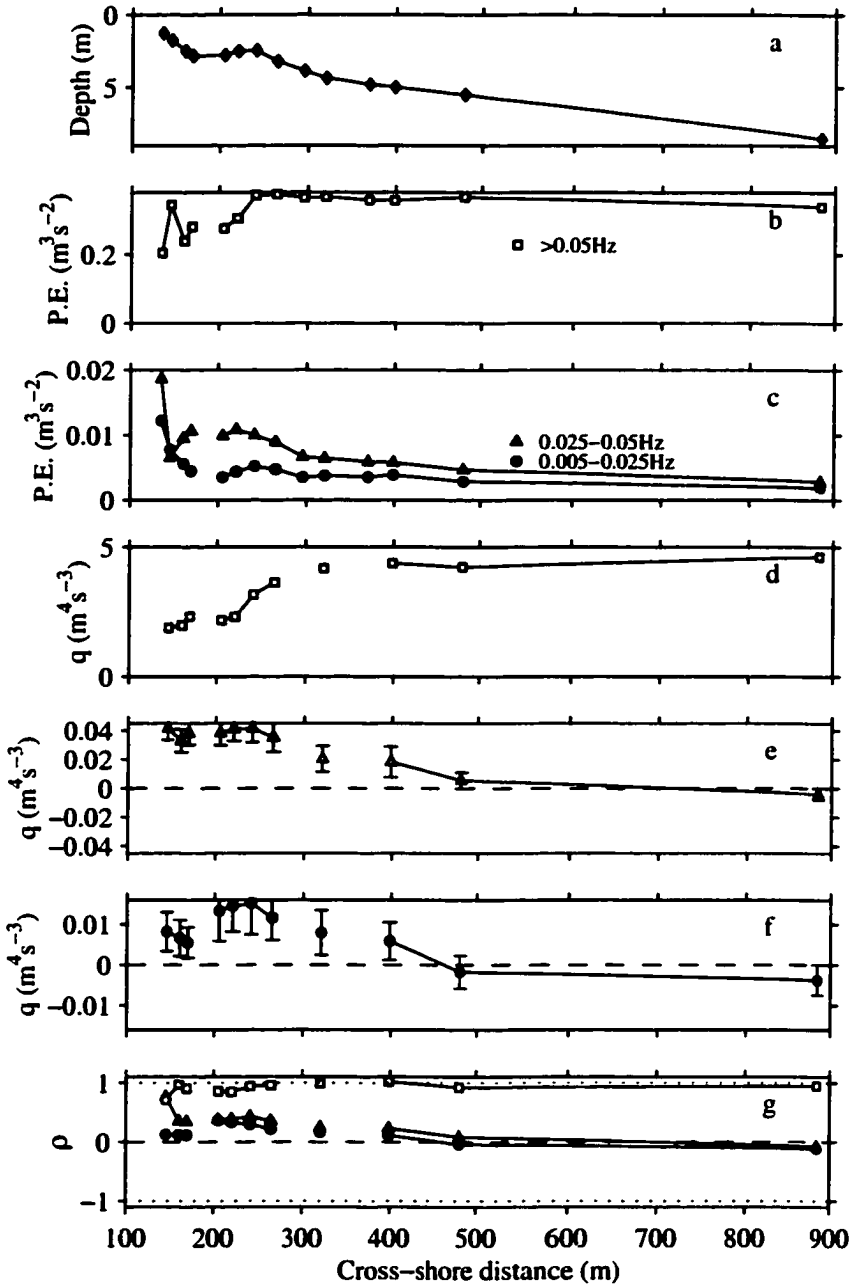

Figure C.9: Water depth (a), potential energy density $P.E.$ (b: swell. c: surf beat), shoreward energy flux q (d: swell. e: high frequency surf beat. f: low frequency surf beat), and progressiveness parameter ρ (g) *versus* cross-shore distance. Values estimated from 3 hr time series on September 26th (10 am), $Hs = 1.1$ m. Squares: Swell (> 0.05 Hz). Triangles: High frequency surf beat (0.025–0.05 Hz). Circles: Low frequency surf beat (0.005–0.025 Hz).

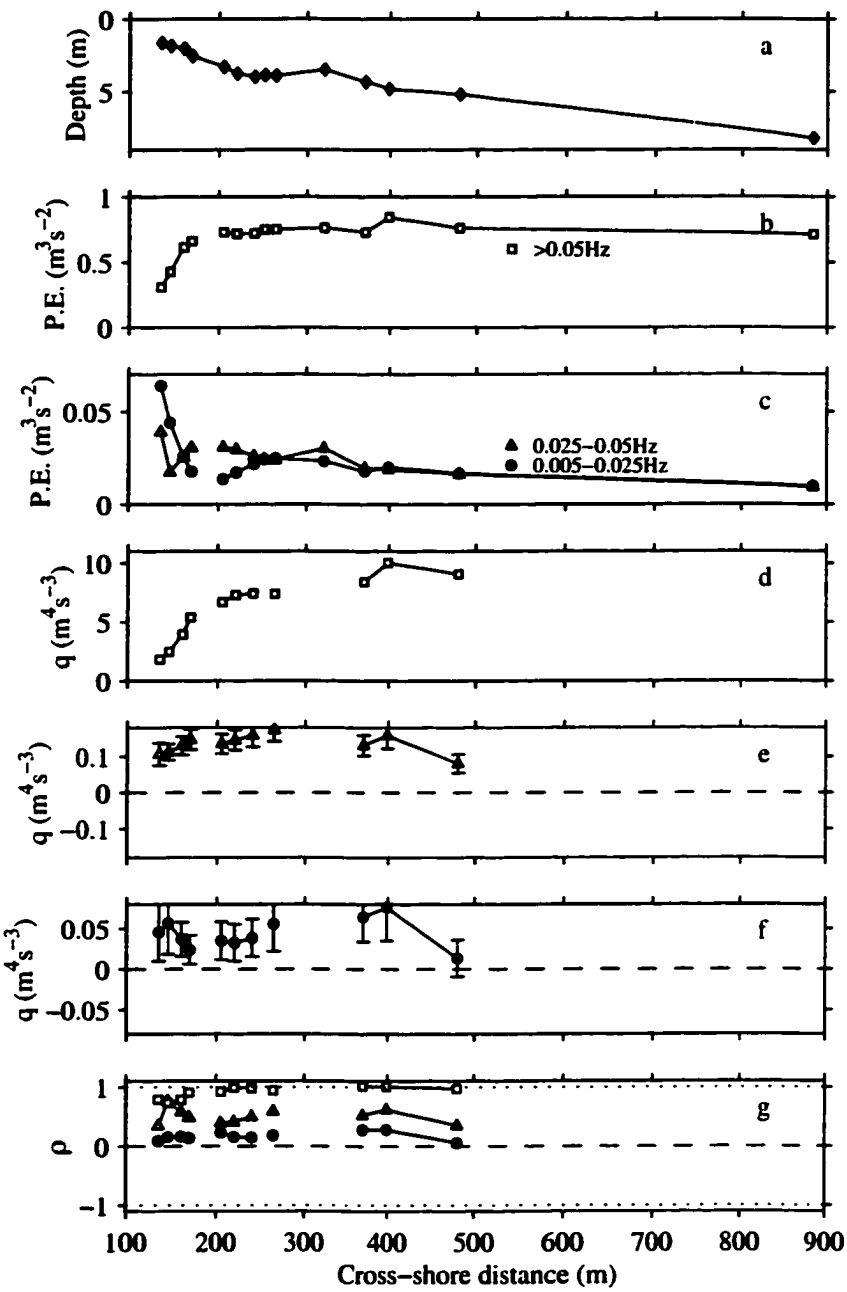

Figure C.10: Water depth (a), potential energy density $P.E.$ (b: swell. c: surf beat), shoreward energy flux q (d: swell. e: high frequency surf beat. f: low frequency surf beat), and progressiveness parameter ρ (g) *versus* cross-shore distance. Values estimated from 3 hr time series on October 18th, Hs = 1.5 m. Squares: Swell (> 0.05 Hz). Triangles: High frequency surf beat (0.025–0.05 Hz). Circles: Low frequency surf beat (0.005–0.025 Hz).

Appendix D

Homogeneous solutions of the dissipative shallow water wave problem

This section presents two linearly-independent homogeneous solutions of eq. (4.5) for a constant beach slope β and damping coefficient λ. Without loss of generality I assume $k > 0$. I also assume nonzero dissipation ($\lambda > 0$).

By introducing $\chi = 2kx$ and $\tilde{\eta} = e^{\chi/2}\hat{\eta}$, the homogeneous form of eq. (4.5) can be transformed into Laguerre's equation

$$\chi \frac{\partial^2 \tilde{\eta}}{\partial \chi^2} + (1 - \chi)\frac{\partial \tilde{\eta}}{\partial \chi} + n'\tilde{\eta} = 0, \tag{D.1}$$

where

$$n' = \frac{1}{2}\left[\frac{\omega^2(1 + i\lambda/\omega)}{kg\beta} - 1\right]. \tag{D.2}$$

Two linearly-independent homogeneous solutions of eq. (D.1) are (Magnus *et al.*, 1966, Section 6.3.1, case 1)

$$\tilde{\eta}_1(\chi) = {}_1F_1(-n', 1, \chi), \tag{D.3}$$

and

$$\tilde{\eta}_2(\chi) = \tilde{\eta}_1(\chi)\log(\chi) + \sum_{k=1}^{\infty} a_k \chi^k, \tag{D.4}$$

where

$$a_k = \frac{(-n')_k}{(k!)^2} \sum_{j=1}^{k} \left(\frac{1}{j - n' - 1} - \frac{2}{j} \right), \tag{D.5}$$

and $(.)_k$ is the Pochammer symbol (Seaborn, 1991, p.18). ${}_1F_1(-n', 1, \chi)$ is a special case of Kummer's function, and can be expressed as a Taylor series

$${}_1F_1(-n', 1, \chi) = \sum_{k=1}^{\infty} b_k \chi^k, \tag{D.6}$$

where $b_0 = 1$, and the remaining b_k satisfy the recurrence relation of the Laguerre polynomials:

$$b_{k+1} = (k+1)^{-2}(k - n')b_k. \tag{D.7}$$

The functions

$$f_B(kx) = \mathrm{e}^{-kx}\tilde{\eta}_1(2kx), \tag{D.8}$$

and

$$f_C(kx) = \mathrm{e}^{-kx}\tilde{\eta}_2(2kx) \tag{D.9}$$

are linearly-independent homogeneous solutions of eq. (4.5). f_B satisfies the shoreward boundary condition (eq. (4.7)), but the series (D.6) for $\tilde{\eta}_1$ does not truncate (since n' is complex, not an integer), so f_B does not satisfy the seaward boundary condition (eq. (4.8)) (Magnus *et al.*, 1966, Section 6.8.2). f_C satisfies neither shoreward nor seaward boundary conditions.

For large x,

$$\hat{\eta} \approx x^{-\xi/2}\mathrm{e}^{\pm kx}, \tag{D.10}$$

where $\xi = 1 \pm \omega^2(1 + \mathrm{i}\lambda/\omega)/(kg\beta)$. Equation (D.10) was derived by introducing a function $\psi(x)$ defined by $\hat{\eta}(x) = \mathrm{e}^{\psi(x)}$, substituting into eq. (4.5), assuming $\partial^2\psi/\partial x^2 \ll (\partial\psi/\partial x)^2$, retaining only the first two terms in x^{-1}, and solving for ψ (Bender and Orszag, 1978,

Section 3.5). Equation (D.10) implies the existence of a solution f_A that decays as $x \to \infty$. Both f_B and f_C diverge as $x \to \infty$ but, since f_B and f_C are linearly-independent, we can express f_A as a linear combination of f_B and f_C, i.e.

$$f_A(kx) = \mathrm{e}^{-kx}[\tilde{\eta}_1(2kx) - C\tilde{\eta}_2(2kx)], \tag{D.11}$$

where C is a constant. C was calculated as the limit to which the ratio $\tilde{\eta}_1/\tilde{\eta}_2$ tends as x becomes large.

Appendix E

Solution for forced, dissipative waves on beach with varying slope and friction coefficient

In this Section I derive matching conditions so that two planar beach solutions can be patched together at $x = x_0$. The general case where an arbitrary number of planar beach sections are patched together is a straightforward, but tedious, extension of the case presented here.

Assume a continuous, piecewise-linear seabed, and a constant damping coefficient in each subregion, so

$$h = \begin{cases} \beta_0 x & x \leq x_0 \\ \beta_1 x' & x \geq x_0 \end{cases}, \tag{E.1}$$

and

$$\lambda = \begin{cases} \lambda^- & x \leq x_0 \\ \lambda^+ & x > x_0 \end{cases}, \tag{E.2}$$

where $x' = x - x_0 + (\beta_0 x_0)/\beta_1$, and $\beta_0, \beta_1 > 0$. From eq.'s (4.1) & (4.3), η and $\tilde{u}$ are continuous at x_0, so

$$\hat{\eta}^+ = \hat{\eta}^-, \tag{E.3}$$

and

$$\frac{\hat{F}_x^+ - g\,\partial\hat{\eta}^+/\partial x - \lambda^+\hat{M}_x^+/h}{\omega + \mathrm{i}\lambda^+} = \frac{\hat{F}_x^- - g\,\partial\hat{\eta}^-/\partial x - \lambda^-\hat{M}_x^-/h}{\omega + \mathrm{i}\lambda^-}, \tag{E.4}$$

$$\Rightarrow \frac{\partial\hat{\eta}^+/\partial x}{\omega + \mathrm{i}\lambda^+} - \frac{\partial\hat{\eta}^-/\partial x}{\omega + \mathrm{i}\lambda^-} = \frac{1}{g}\left[\frac{\hat{F}_x^+ - \lambda^+\hat{M}_x^+/h}{\omega + \mathrm{i}\lambda^+} - \frac{\hat{F}_x^- - \lambda^-\hat{M}_x^-/h}{\omega + \mathrm{i}\lambda^-}\right], \tag{E.5}$$

where

$$\eta^+ = \lim_{x \to x_0+} \eta(x), \tag{E.6}$$

and

$$\eta^- = \lim_{x \to x_0-} \eta(x), \tag{E.7}$$

and similarly for $\partial\hat{\eta}/\partial x$, $\hat{F}$ and $\hat{M}_x$.

The inhomogeneous matching condition (eq. (E.5)) complicates matters. The most straightforward expression for the solution is

$$\hat{\eta}(x) = \int_{\substack{x_F \\ x_F \neq x_0}} G(x, x_F)\hat{F}(x_F)\,dx_F + \tilde{G}(x, x_0), \tag{E.8}$$

where

$$\int_{\substack{x_F \\ x_F \neq x_0}} \tag{E.9}$$

is the integral over all values of x_F except x_0. $G(x, x_F)$ satisfies eq.'s (4.17), (4.18), and the *homogeneous* matching conditions

$$\hat{\eta}^+ = \hat{\eta}^-, \tag{E.10}$$

and

$$\frac{\partial\hat{\eta}^+/\partial x}{\omega + i\lambda^+} = \frac{\partial\hat{\eta}^-/\partial x}{\omega + i\lambda^-}. \tag{E.11}$$

The function $\tilde{G}$ is added to satisfy the inhomogeneous matching conditions, and is defined by

$$\tilde{G}(x, x_0) = \begin{cases} Bf_B(n_1', x) & x < x_0 \\ Af_A(n_2', x) & x \geq x_0 \end{cases}, \tag{E.12}$$

where A and B are chosen to satisfy eq.'s (E.3) & (E.5). n_1' and n_2' are the values of n' for each subregion, determined from eq. (D.2). Here the dependence of f_A and f_B on n' is made explicit to emphasise the dependence of n' on cross-shore location.

The point-forced solutions presented in Section 4.3.3 were obtained by assuming that $\hat{F}_x - \lambda \hat{M}_x/h = 0$, so $\tilde{G} = 0$. The solutions presented in Section 4.3.4 allowed for non-zero values of $\tilde{G}$.

Appendix F

Normal modes

F.1 Introduction

Forced, dissipative shallow water waves on a planar beach can be viewed as a superposition of normal modes (Section F.2). Normal modes are eigensolutions to the unforced, or 'free wave' problem. When Q is high, and a significant proportion of the forcing projects onto resonant modes, the cross-shore structure of forced waves is similar to the the structure of free waves, and normal modes provide a very efficient description of the wave field (Section F.3). However, when Q is low, or forcing is nearly orthogonal to the resonant modes, forced waves differ greatly from free waves, and normal modes do not simplify the physical description of the problem. In fact, as I show in Sections F.4–F.6, the use of normal modes greatly complicates the discussion of cross-shore propagation, evanescence, and dissipative decoupling.

F.2 Method

The homogeneous form of eq. (4.5) is

$$\mathcal{L}[\hat{\eta}] + \Lambda\hat{\eta} = 0, \tag{F.1}$$

where

$$\mathcal{L}[\hat{\eta}] = \frac{\partial}{\partial x}\left(x\frac{\partial \hat{\eta}}{\partial x}\right) - k^2 x\hat{\eta}, \tag{F.2}$$

and

$$\Lambda = \frac{\omega^2}{g\beta}\left(1 + \mathrm{i}\frac{\lambda}{\omega}\right). \tag{F.3}$$

Dissipation has been incorporated into eq. (F.3). The operator $\mathcal{L}$ is unchanged by the introduction of dissipation[1], so the eigenvalues Λ_n and eigenfunctions φ_n are the same as in the non-dissipative case, namely

$$\Lambda_n = k(2n+1), \tag{F.4}$$

where $n \in \mathbb{Z}^+$,

$$\varphi_n(x) = \mathrm{e}^{-kx}\,{}_1F_1(-n, 1, 2kx), \tag{F.5}$$

and ${}_1F_1(-n, 1, 2kx)$ is defined by eq.'s (D.6) & (D.7). The eigenfunctions are orthogonal, so

$$\int_{x=0}^{\infty} \varphi_n(x)\varphi_m(x) 2k\, dx = \delta_{n,m}. \tag{F.6}$$

From eq.'s (F.3) & (F.4), ω is complex if k is real. Therefore, all longshore-homogeneous free waves decay due to the presence of dissipation. Next, I show that the eigenfunctions φ_n can be used to determine the steady-state response to forcing.

The forced edge wave problem is

$$\mathcal{L}[\hat{\eta}] + \Lambda\hat{\eta} = \hat{F}. \tag{F.7}$$

Assume that forcing is steady and longshore-homogeneous. Now ω and k are real, so Λ must be complex (note that the set $\{\Lambda_n\}$ is the set of eigenvalues, but Λ is no longer an eigenvalue). We express $\hat{\eta}$ and $\hat{F}$ as sums of normal modes, i.e.

$$\hat{\eta} = \sum_{n=0}^{\infty} a_n \varphi_n, \tag{F.8}$$

[1] However, if λ varied with x, then we would have to incorporate dissipation into $\mathcal{L}$. The problem could then be solved using dissipative normal modes (Garrett and Greenberg, 1977).

and

$$\hat{F} = \sum_{n=0}^{\infty} f_n \varphi_n, \tag{F.9}$$

where

$$f_n = \int_{x=0}^{\infty} \hat{F}(x)\varphi_n(x) 2k \, dx. \tag{F.10}$$

Equation (F.7) now becomes

$$\sum_{n=0}^{\infty} a_n \mathcal{L}[\varphi_n] + \Lambda \sum_{n=0}^{\infty} a_n \varphi_n = \sum_{n=0}^{\infty} f_n \varphi_n, \tag{F.11}$$

$$\Rightarrow \sum_{n=0}^{\infty} a_n (\Lambda - \Lambda_n) \varphi_n = \sum_{n=0}^{\infty} f_n \varphi_n. \tag{F.12}$$

Introducing $\omega_n = (g\beta\Lambda_n)^{1/2}$, multiplying by $2k\varphi_m$, and integrating over x from zero to infinity gives

$$\sum_{n=0}^{\infty} \frac{\omega^2(1 + \mathrm{i}\lambda/\omega) - \omega_n^2}{g\beta} a_n \int_{x=0}^{\infty} \varphi_n \varphi_m 2k \, dx = \sum_{n=0}^{\infty} f_n \int_{x=0}^{\infty} \varphi_n \varphi_m 2k \, dx. \tag{F.13}$$

From eq.'s (F.6) & (F.13)

$$a_m = \frac{g\beta f_m}{\omega^2(1 + 2\mathrm{i}Q^{-1}) - \omega_m^2}, \tag{F.14}$$

where

$$Q = 2\omega/\lambda. \tag{F.15}$$

The particular solution of the dissipative edge wave problem is given by eq.'s (F.5), (F.8), (F.14), & (F.15).

F.3 Resonance

The parameter Q defined by equation (F.15) is equivalent to the Q defined by eq. (1.1), and determines the strength of edge wave resonance. When Q is large, the gain function

$|a_m/f_m|^2$ has a resonant peak centered on the frequency $\omega_m(1 - Q^{-2})$, whose height is $O(Q^2)$, and whose half-power width is ω_m/Q (eq. (F.14)).

Equation (F.14) is identical to the equation for the response of a dissipative simple harmonic oscillator to sinusoidal forcing. The use of normal modes has lead to an elegant solution, one which emphasises the role of Q in determining the strength of edge wave resonance. The normal modes approach was previously used by Gallagher (1971), Bowen (1977), Bowen and Guza (1978), & Lippmann *et al.* (1997) (these authors assumed weak dissipation).

F.4 Propagation

In Section F.2 I showed that forced, dissipative edge waves can be expressed as a sum of normal modes. Each mode has the same cross-shore structure as a non-dissipative, free edge wave, and is cross-shore standing. Yet the sum of the normal modes represents a dissipative edge wave, which propagates across-shore (Section 4.3.1). Figures F.1 & F.2 show how the forced, dissipative edge wave presented in fig. 4.3e,f is approximated by the first four normal modes. The $n = 2$ mode resonates and has a large amplitude (fig. F.1c). Other normal modes do not resonate, and have smaller amplitudes. Non-resonant modes are almost 90 degrees out of phase with the resonant mode, so the sum of the first four modes forms a cross-shore progressive pattern (fig.F.2). This pattern is similar, but not identical, to the full Green's function solution shown in fig.4.3e,f. As more modes are added, the normal mode solution converges to the Green's function (when plotted, the sum of the first 30 normal modes is almost indistinguishable from the Green's function).

From the discussion above, we see that propagating waves can be represented as a sum of cross-shore standing normal modes. These normal modes are coherent (their amplitudes co-vary), so their sum represents a cross-shore shape different from the shape of any one normal mode. The situation would be simpler if propagation was described by individual normal modes, rather than by a set of coherent modes. Individual dissipative normal modes, which are obtained by including dissipation in the operator $\mathcal{L}$ rather than in the eigenvalue

of eq. (F.1), can propagate (Webster, 1985). Such propagation redistributes the energy of each mode to regions where dissipation is particularly strong. However, the direction of forced wave propagation (as opposed to normal mode propagation) is not determined solely by the intensity of dissipation. Since waves propagate from regions of net forcing to regions of net dissipation (Section 4.2.3), the distribution of forcing plays a vital role in determining the direction of net cross-shore propagation. Dissipative waves propagate seawards offshore of regions of forcing, and shorewards onshore of regions of forcing. Normal modes, whether dissipative or non-dissipative, are solutions to the homogeneous problem — they are calculated without any reference to the spatial distribution of forcing. Consequently, individual normal modes can not represent propagation away from regions of forcing. When a forced wave field is represented using normal modes, a set of coherent modes is required to represent propagation away from regions of forcing.

F.5 Evanescent waves

Consider the case where resonant forcing of frequency ω and wavenumber k is applied far outside the turning point. Most of the variance of the resonant mode is confined inside the turning point. Consequently, the forcing is almost orthogonal to the resonant normal mode, and the projection of forcing onto the resonant mode (f_n) is very small (eq. (F.10)). If Q is not very large, then the small forcing f_n can not excite a large response. However, if Q is sufficiently large, then the denominator of eq. (F.14) becomes very small, and a large resonant edge wave is generated. Since the resonant normal mode decays as approximately e^{-Kx} outside the turning point, the amplitude of the resonant response scales with Qe^{-KL}, in agreement with eq. (4.29) (L is the distance from the turning point to the point of forcing).

Figure F.3 shows several approximations to the point-forced evanescent wave of fig. 4.8e,f obtained using finite sums of normal modes. Many coherent normal modes are required to represent evanescent waves, because the cross-shore structure of evanescent waves differs greatly from the cross-shore structure of each individual normal mode. The

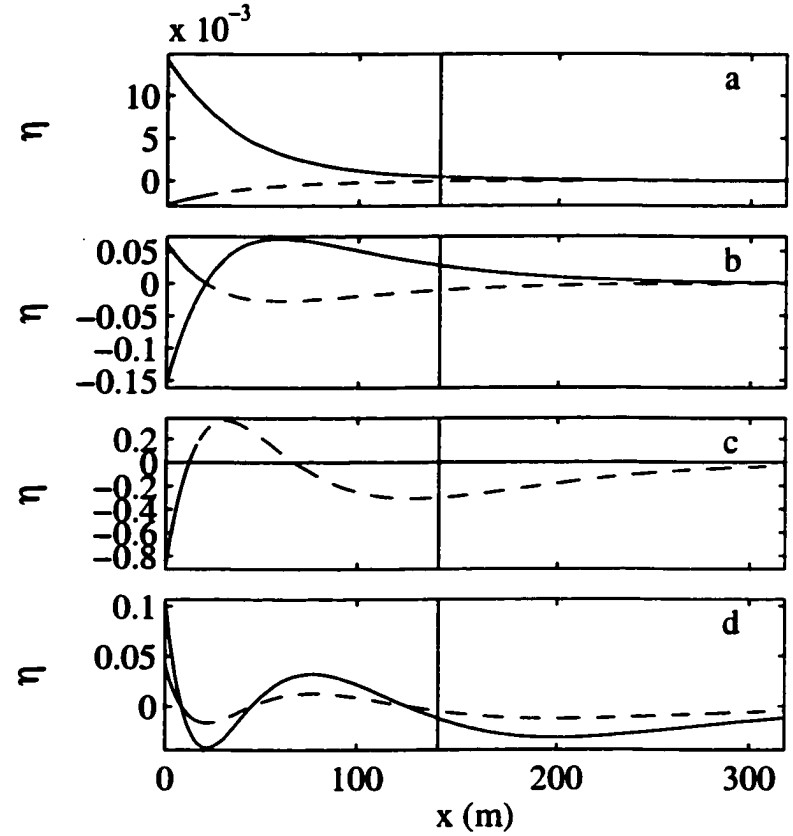

Figure F.1: Contribution from each of first four normal modes to the point-forced dissipative edge wave of fig. 4.3e,f. Solid lines: Real part of sea level amplitude. Dashed lines: Imaginary part of sea level amplitude. a: mode 0. b: mode 1. c: mode 2. d: mode 3.

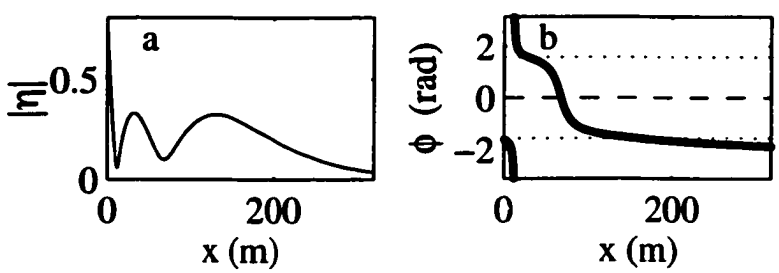

Figure F.2: Approximation to the point-forced dissipative edge wave of fig. 4.3e,f obtained from sum of first four normal modes. a: magnitude $|\eta|$. b: phase ϕ.

number of Taylor series terms, and therefore the computational time, required to evaluate a normal mode increases with the mode number. When the Taylor series expressions for high modes contained terms involving x raised to powers much greater than 40, computational errors became very large. Consequently, I was unable to accurately express the evanescent wave shown in fig. 4.8e,f as a sum of normal modes.

F.6 Dissipative decoupling

Consider two normal modes with resonant frequencies ω_n and ω_m, forced with frequency ω_n. From eq. (F.14), the ratio between the amplitudes of the two modes is

$$\frac{a_n}{a_m} = (1 + \mathrm{i}Q\sigma)\frac{f_n}{f_m}, \tag{F.16}$$

where $2\sigma = (\omega_m/\omega_n)^2 - 1$. If $\sigma \ll 1$, then $\sigma \approx \omega_m/\omega_n - 1$ is the relative change in frequency between ω_n and ω_m.

The term 'mode coupling' is standard, but confusing. Mode coupling does not refer to coupling between normal modes. Instead, mode coupling is analogous to coupling between two oscillators — in the case discussed in Section 4.3.3, mode coupling refers to coupling between bar- and shore-trapped waves.

A time scale for energy exchange between bar- and shore-trapped waves is $(\sigma\omega_n)^{-1}$ (Garrett, 1969). If $\sigma Q \ll 1$, as will be the case if Q is not extremely large and coupling between bar- and shore-trapped waves is weak,

$$a_n/a_m \approx f_n/f_m. \tag{F.17}$$

Conversely, if $\sigma Q \gg 1$ (for weakly coupled bar- and shore-trapped waves, this requires that Q be extremely large)

$$a_n/a_m \approx \mathrm{i}Q\sigma f_n/f_m. \tag{F.18}$$

The very weakly-dissipative case described by eq. (F.18) is straightforward — if $|f_n| = O(f_m)$, then $a_n \gg a_m$, so the resonant normal mode dominates over the non-resonant

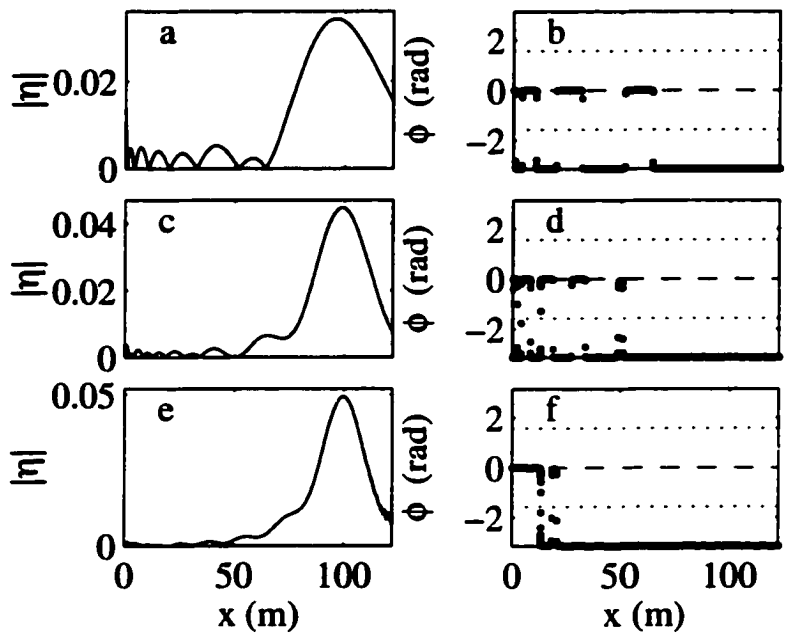

Figure F.3: Approximations to the point-forced evanescent wave of fig. 4.8e,f obtained from finite sums of normal modes. Approximation obtained by adding: a,b: First 10 modes. c,d: First 24 modes. e,f: First 44 modes. a,c,e: magnitude $|\eta|$. b,d,f: phase ϕ.

normal mode. Examples of resonant normal modes are shown in fig 4.17c,d,i,j. Note that a single resonant normal mode was made up of coupled bar- and shore-trapped waves.

To understand the more dissipative case described by eq. (F.17), consider the normal modes shown in fig. 4.17c,d,i,j. If we call these modes φ_n and φ_m, then from fig. 4.17

$$\varphi_n \approx \begin{cases} \varphi_m & \text{over bar} \\ -\varphi_m & \text{over shoreface} \end{cases} . \tag{F.19}$$

If forcing is confined to the bar, then $f_n \approx f_m$ (eq.'s (F.10) & (F.19)), so $a_n \approx a_m$ (eq. (F.17)) and

$$\eta \approx \begin{cases} 2a_n\varphi_n & \text{over bar} \\ 0 & \text{over shoreface} \end{cases} . \tag{F.20}$$

The two normal modes reinforce one another over the bar and cancel over the shoreface. By adding two normal modes, each with energy over both the bar and the shoreface, we get *only* a bar-trapped wave. If forcing is applied over the shoreface, then $f_n \approx -f_m$, so $a_n \approx -a_m$, the normal modes reinforce over the shoreface and cancel over the bar, and we get only shore-trapped waves. In this manner, dissipative decoupling is represented as a sum of two coherent normal modes.

F.7 Summary

This thesis investigates the modification of surf beat by dissipation and forcing. Dissipation and forcing modify surf beat by introducing waves that propagate from regions of forcing to regions of dissipation, by decoupling bar- and shore-trapped waves, and by allowing evanescent waves to be seen at leading order. These processes ensure that the cross-shore structure of dissipative infragravity waves depends on the cross-shore structure of the applied forcing. In contrast, the cross-shore structure of normal modes is independent of the applied forcing. Therefore, when normal modes are used, we must represent a wave whose structure depends on the forcing, using modes whose structure is independent of the forcing. We can not solve this problem using any one normal mode. We can achieve the desired

result using an infinite sum of normal modes, but such an approach leads to a complicated discussion of straightforward physics.

Bibliography

Arfken, G. B. and Weber, H. J., 2001: , *Mathematical methods for physicists*. Academic Press, San Diego, 5 edition.

Bauer, B. O. and Greenwood, B., 1990: Modification of a linear bar-trough system by a standing edge wave. *Marine Geology*, **92**, 177–204.

Bender, C. M. and Orszag, S. A., 1978: , *Advanced mathematical methods for scientists and engineers*. McGraw-Hill, New York.

Bowen, A., 1969a: Rip currents 1. Theoretical discussion. *Journal of Geophysical Research*, **74**, 5467–5490.

Bowen, A., 1969b: Rip currents 2. laboratory and field observations. *Journal of Geophysical Research*, **74**, 5479–5490.

Bowen, A., 1977: Wave-wave interactions near the shore. *Lecture notes in Physics*, **64**, 102–113.

Bowen, A., 1981: Simple models of nearshore sedimentation; beach profiles and longshore bars. *The Coastline of Canada*, **80-10**, 1–11.

Bowen, A. and Guza, R., 1978: Edge waves and surf beat. *Journal of Geophysical Research*, **83**, 1913–1920.

Bowen, A. J. and Inman, D. L., 1971: Edge waves and crescentic bars. *Journal of Geophysical Research*, **76**, 8662–8671.

Bryan, K. and Bowen, A., 1996: Edge wave trapping and amplification on barred beaches. *Journal of Geophysical Research*, **101**, 6543–6552.

Bryan, K., Howd, P., and Bowen, A., 1998: Field observations of bar-trapped edge waves. *Journal of Geophysical Research*, **103**, 1285–1305.

Chen, Y. and Guza, R., 1997: Modeling spectra of breaking surface waves in shallow water. *Journal of Geophysical Research*, **102**, 25035–25046.

Chen, Y. and Guza, R., 1999: Resonant scattering of edge waves on longshore periodic topography: Finite beach slope. *Journal of Fluid Mechanics*, **387**, 255–269.

Eckart, C., 1951: . Surface waves in water of variable depth. Wave Rep. 100, Scripps Institution of Oceanography, La Jolla, California.

Eckart, C., 1961: Internal waves in the ocean. *Physics of Fluids*, **4**, 791–799.

Eldeberky, Y. and Battjes, J., 1996: Spectral modeling of wave breaking: Applications of Boussinesq equations. *Journal of Geophysical Research*, **101**, 1253–1264.

Elgar, S. and Guza, R., 1985a: Observations of bispectra of shoaling surface gravity waves. *Journal of Fluid Mechanics*, **161**, 425–448.

Elgar, S. and Guza, R., 1985b: Shoaling gravity waves: comparisons between field observations, linear theory, and a nonlinear model. *Journal of Fluid Mechanics*, **158**, 47–70.

Elgar, S., Herbers, T., Okihiro, M., Oltman-Shay, J., and Guza, R., 1992: Observations of infragravity waves. *Journal of Geophysical Research*, **97**, 15573–15577.

Elgar, S., Herbers, T., and Guza, R., 1994: Reflection of ocean surface gravity waves from a natural beach. *Journal of Physical Oceanography*, **24**, 1503–1511.

Elgar, S., Guza, R., Raubenheimer, B., Herbers, T., and Gallagher, E. L., 1997: Spectral evolution of shoaling and breaking waves on a barred beach. *Journal of Geophysical Research*, **102**, 15797–15805.

Feddersen, F., Guza, R., Elgar, S., and Herbers, T., 1998: Alongshore momentum balances in the nearshore. *Journal of Geophysical Research*, **103**, 15667–15676.

Flynn, W. G. and Littlejohn, R. G., 1994: Normal forms for linear mode conversion and Landau-Zerner transitions in one dimension. *Annals of Physics*, **234**, 334–403.

Freilich, M. and Guza, R., 1984: Nonlinear effects on shoaling surface gravity waves. *Philosophical transactions of the Royal Society of London*, **311**, 1–41.

Gallagher, B., 1971: Generation of surf beat by non-linear wave interactions. *Journal of Fluid Mechanics*, **49**, 1–20.

Gallagher, E. L., Elgar, S., and Guza, R., 1998: Observations of sand bar evolution on a natural beach. *Journal of Geophysical Research*, **103**, 3203–3215.

Gallagher, E., Boyd, W., Elgar, S., Guza, R., and Woodward, B., 1996: Performance of a sonar altimeter in the nearshore. *Marine Geology*, **133**, 241–248.

Garrett, C., 1969: Atmospheric edge waves. *Quarterly Journal of the Royal Meteorological Society*, **95**, 731–753.

Garrett, C. and Greenberg, D., 1977: Predicting changes in tidal regime: The open boundary problem. *Journal of Physical Oceanography*, **7**, 171–181.

Green, E. I., 1955: The story of Q. *American Scientist*, **43**, 584–594.

Grimshaw, R. and Allen, J., 1982: The effect of dissipation on linearly coupled, slowly varying oscillators. *Studies in Applied Mathematics*, **67**, 169–198.

Guza, R. and Bowen, A., 1976a: Finite amplitude edge waves. *Journal of Marine Research*, **34**, 269–293.

Guza, R. and Bowen, A., 1976b: . Resonant interactions for waves breaking on a beach. In *Proceedings of the 15th International Conference on Coastal Engineering*, pages 560–579. ASCE.

Guza, R. and Davis, R., 1974: Excitation of edge waves by waves incident on a beach. *Journal of Geophysical Research*, **79**, 1285–1291.

Guza, R. and Inman, D. L., 1975: Edge waves and beach cusps. *Journal of Geophysical Research*, **80**, 2997–3012.

Guza, R. and Thornton, E., 1985: Observations of surf beat. *Journal of Geophysical Research*, **90**, 3161–3172.

Guza, R., Thornton, E., and Holman, R., 1984: . Swash on steep and shallow beaches. In *Proceedings of the 19th International Conference on Coastal Engineering*, pages 708–723. ASCE.

Hasselmann, K., Munk, W., and MacDonald, G., 1963: . Bispectra of ocean waves. In M.Rosenblatt, editor, *Proceedings of the symposium on time series analysis*, SIAM series in applied maths, pages 125–139. Wiley.

Henderson, S. M. and Bowen, A., 2001: . The dynamics of dissipative edge waves. In *Coastal Dynamics 2001*, pages 263–271. ASCE.

Henderson, S. M. and Bowen, A., 2002: Observations of surf beat forcing and dissipation. *Journal of Geophysical Research*, page in press.

Henderson, S. M., Elgar, S., and Bowen, A., 2001: . Observations of surf beat propagation and energetics. In *Proceedings of the 27th International Conference on Coastal Engineering*, pages 1412–1421. ASCE.

Herbers, T. and Burton, M., 1997: Nonlinear shoaling of directionally spread waves on a beach. *Journal of Geophysical Research*, **102**, 21101–21114.

Herbers, T. and Guza, R., 1992: Wind-wave nonlinearity observed at the sea floor. part 2: Wavenumbers and third order statistics. *Journal of Physical Oceanography*, **22**, 489–504.

Herbers, T., Elgar, S., and Guza, R., 1994: Infragravity-frequency (0.005–0.05Hz) motions on the shelf. Part 1: Forced waves. *Journal of Physical Oceanography*, **24**, 917–927.

Herbers, T., Elgar, S., and Guza, R., 1995a: Generation and propagation of infragravity waves. *Journal of Geophysical Research*, **100**, 24863–24872.

Herbers, T., Elgar, S., Guza, R., and O'Reilly, W., 1995b: Infragravity-frequency (0.005–0.05Hz) motions on the shelf. Part 2: Free waves. *Journal of Physical Oceanography*, **25**, 1063–1079.

Herbers, T., Elgar, S., and Guza, R., 1999: Directional spreading of waves in the nearshore. *Journal of Geophysical Research*, **104**, 7683–7693.

Herbers, T., Russnogle, N., and Elgar, S., 2000: Spectral energy balance of breaking waves within the surf zone. *Journal of Physical Oceanography*, **30**, 2723–2737.

Holland, K., Raubenheimer, B., Guza, R., and Holman, R., 1995: Runup kinematics on a natural beach. *Journal of Geophysical Research*, **100**, 4985–4993.

Holman, R., 1981: Infragravity energy in the surf zone. *Journal of Geophysical Research*, **86**, 6442–6450.

Holman, R. and Bowen, A., 1979: Edge waves on complex beach profiles. *Journal of Geophysical Research*, **84**, 6339–6346.

Holman, R. and Bowen, A., 1982: Bars, bumps and holes: Models for the generation of complex beach topography. *Journal of Geophysical Research*, **87**, 457–468.

Holman, R. and Bowen, A., 1984: Longshore structure of infragravity wave motions. *Journal of Geophysical Research*, **89**, 6446–6452.

Howd, P. A., Bowen, A., and Holman, R. A., 1992: Edge waves in the presence of strong longshore currents. *Journal of Geophysical Research*, **97**, 11357–11371.

Huntley, D., Guza, R., and Thornton, E., 1981: Field observations of surf beat. 1. Progressive edge waves. *Journal of Geophysical Research*, **86**, 6451–6466.

Huntley, D. A. and Kim, C. S., 1984: . Is surf beat forced or free? In *Proceedings of the 19th International Conference on Coastal Engineering*, pages 871–885. ASCE.

Johnson, R. A. and Wichern, D. W., 1982: , *Applied multivariate statistical analysis.* Prentice-Hall, Englewood Cliffs, NJ 07632, 3rd edition.

Kenyon, K., 1970: A note on conservative edge wave interactions. *Deep-Sea Research*, **17**, 197–201.

Lee, G. and Birkemeier, W., 1993: . Beach and nearshore survey data: 1985–1991, CERC field research facility. In *Technical Report CERC-93-3*. U.S. Army Corps of Engineers, Waterways Exp. Stn, Vicksburg, Miss.

Lippmann, T., Holman, R., and Bowen, A., 1997: Generation of edge waves in shallow water. *Journal of Geophysical Research*, **102**, 8663–8679.

Lippmann, T., Herbers, T., and Thornton, E., 1999: Gravity and shear wave contributions to nearshore infragravity wave motions. *Journal of Physical Oceanography*, **29**, 231–239.

Lippmann, T., Herbers, T., and Thornton, E., 1998: . Cross-shore variability of infragravity wave pressure and velocities on a barred beach. In *Coastal Dynamics '97*, pages 1023–1032. ASCE.

Lippmann, T., Herbers, T., and Thornton, E., 2001: . Observations of infragravity waves in the nearshore. In H. Hanson and M. Larson, editors, *Coastal Dynamics '01*, pages 55–61. ASCE.

List, J. H., 1991: Wave groupiness variations in the nearshore. *Coastal Engineering*, **15**, 475–496.

Longuet-Higgins, M., 1967: On trapping of wave energy round islands. *Journal of Fluid Mechanics*, **29**, 781–821.

Longuet-Higgins, M. and Stewart, R., 1962: Radiation stress and mass transport in gravity waves, with application to 'surf beats'. *Journal of Fluid Mechanics*, **13**, 481–504.

Longuet-Higgins, M. and Stewart, R., 1964: Radiation stresses in water waves: a physical discussion, with applications. *Deep-Sea Research*, **11**, 529–562.

Louisell, W. H., 1960: , *Coupled mode and parametric electronics*. Wiley, New York.

Magnus, W., Oberhettinger, F., and Soni, R. P., 1966: , *Formulas and theorems for the special functions of mathematical physics*. Springer-Verlag, New York, 3 edition.

Masselink, G., 1995: Group bound long waves as a source of infragravity energy in the surf zone. *Continental Shelf Research*, **15**, 1525–1547.

Mathew, J. and Akylas, T., 1990: On the radiation damping of finite amplitude edge waves. *Proceedings of the Royal Society of London, Series A*, **431**, 419–431.

Mei, C. C., 1983: , *The applied dynamics of ocean surface waves*. Wiley, New York.

Middleton, J. H., Cahill, M. L., and Hsieh, W. W., 1987: Edge waves on the Sydney coast. *Journal of Geophysical Research*, **92**, 9487–9493.

Miles, J., 1990: Wave reflection from a gently sloping beach. *Journal of Fluid Mechanics*, **214**, 59–66.

Munk, W., Snodgrass, F., and Gilbert, F., 1964: Long waves on the continental shelf: an experiment to separate leaky and trapped waves. *Journal of Fluid Mechanics*, **20**, 529–554.

Nelson, R. and Gonsalves, J., 1992: Surf zone transformation of wave height to water depth ratios. *Coastal Engineering*, **17**, 49–70.

Nielsen, P., 1992: , *Coastal bottom boundary layers and sediment transport*. World Scientific, River Edge, N.J., U.S.A.

Ohanian, H. C., 1990: , *Principles of quantum mechanics*. Prentice Hall, New Jersey.

O'Hare, T. and Huntley, D., 1994: Bar formation due to wave groups and associated long waves. *Marine Geology*, **116**, 313–325.

Okihiro, M., Guza, R., and Seymour, R., 1992: Bound infragravity waves. *Journal of Geophysical Research*, **97**, 11453–11469.

Oltman-Shay, J. and Guza, R., 1987: Infragravity edge wave observations on two California beaches. *Journal of Physical Oceanography*, **17**, 644–663.

Parrish, D. F. and Niiler, P. P., 1971: Topographic generation of long internal waves in a channel. *Geophysical Fluid Dynamics*, **2**, 1–15.

Phillips, O., 1977: , *The dynamics of the upper ocean.* Cambridge University Press, Cambridge, England, 2 edition.

Priestley, M., 1988: , *Non-linear and non-stationary time series analysis.* Academic Press, 24/28 Oval Road, London NW1 7DX, England.

Raubenheimer, B., Guza, R., Elgar, S., and Kobayashi, N., 1995: Swash on a gently sloping beach. *Journal of Geophysical Research*, **100**, 8751–8760.

Raubenheimer, B., Guza, R., and Elgar, S., 1996: Wave transformation across the inner surf zone. *Journal of Geophysical Research*, **101**, 25589–25597.

Ruessink, B., 1998a: Bound and free infragravity waves in the nearshore zone under breaking and nonbreaking conditions. *Journal of Geophysical Research*, **103**, 12795–12805.

Ruessink, B., 1998b: The temporal and spatial variability of infragravity energy in a barred nearshore zone. *Continental Shelf Research*, **18**, 585–605.

Sallenger, A. H. and Holman, R. A., 1985: Wave energy saturation on a natural beach of variable slope. *Journal of Geophysical Research*, **90**, 11939–11944.

Saulter, A. N., O'Hare, T. J., and Russell, P. E., 1997: . Analysis of infragravity wave-driven sediment transport on macrotidal beaches. In *Coastal Dynamics*, pages 1033–1042. ASCE.

Schäffer, H., 1993: Infragravity waves induced by short-wave groups. *Journal of Fluid Mechanics*, **247**, 551–588.

Schäffer, H., 1994: Edge waves forced by short-wave groups. *Journal of Fluid Mechanics*, **259**, 125–148.

Schönfeldt, H.-J., 1995: On the modification of edge waves by longshore currents. *Continental Shelf Research*, **15**, 1213–1220.

Seaborn, J. B., 1991: , *Hypergeometric functions and their applications*. Number 8 in Texts in Applied Mathematics. Springer-Verlag, New York.

Sheremet, A., Guza, R., Elgar, S., and Herbers, T., 2001: . Estimating infragravity wave properties from pressure-current meter array observations. In *Proceedings of the 27th International Conference on Coastal Engineering*, pages 1476–1489. ASCE.

Short, A. D., 1975: Multiple offshore bars and standing waves. *Journal of Geophysical Research*, **80**, 3838–3840.

Sleath, J., 1984: , *Sea bed mechanics*. Wiley, New York.

Svendsen, I. A. and Putrevu, U., 1994: Nearshore mixing and dispersion. *Proceedings of the Royal Society of London, Series A*, **445**, 561–576.

Symonds, G., Huntley, D., and Bowen, A., 1982: Two-dimensional surf beat: Long wave generation by a time-varying breakpoint. *Journal of Geophysical Research*, **87**, 492–498.

Symonds, G. and Rangasinghe, R., 2001: . On the formation of rip currents on a plane beach. In *Proceedings of the 27th International Conference on Coastal Engineering*, pages 468–481. ASCE.

Tucker, M., 1950: Surf beats: Sea waves of 1 to 5 min. period. *Proceedings of the Royal Society of London, Series A*, **202**, 565–573.

Tugnait, J. K., 1994: Detection on non-gaussian signals using integrated polyspectrum. *IEEE transactions on signal processing*, **42**, 3137–3149.

Ursell, F., 1952: Edge waves on a sloping beach. *Proceedings of the Royal Society, Series A*, **214**, 79–97.

Van Dongeren, A., Svendsen, I., and Sancho, F., 1996: . Generation of infragravity waves. In *Proceedings of the 25th International Conference on Coastal Engineering*, pages 1335–1348. ASCE.

Van Dongeren, A., Svendsen, I., and Putrevu, U., 1998: . Quasi 3-d effects in infragravity waves. In *Proceedings of the 26th International Conference on Coastal Engineering*, pages 1323–1336. ASCE.

Vittori, G., De Swart, H., and Blondeaux, P., 1999: Crescentic bedforms in the nearshore region. *Journal of Fluid Mechanics*, **381**, 271–303.

Webster, I., 1985: Frictional continental shelf waves and the circulation response of a continental shelf to wind forcing. *Journal of Physical Oceanography*, **15**, 855–864.

Whitham, G., 1962: Mass, momentum and energy flux in water waves. *Journal of Fluid Mechanics*, **12**, 135–147.

Yeh, T. and Van Atta, C., 1973: Spectral transfer of scalar and velocity fields in heated grid turbulence. *Journal of Fluid Mechanics*, **58**, 233–261.